Journal of

Computation and Artificial Intelligence in Mechanics and Biomechanics

Editor in Chief:
Jorge Belinha

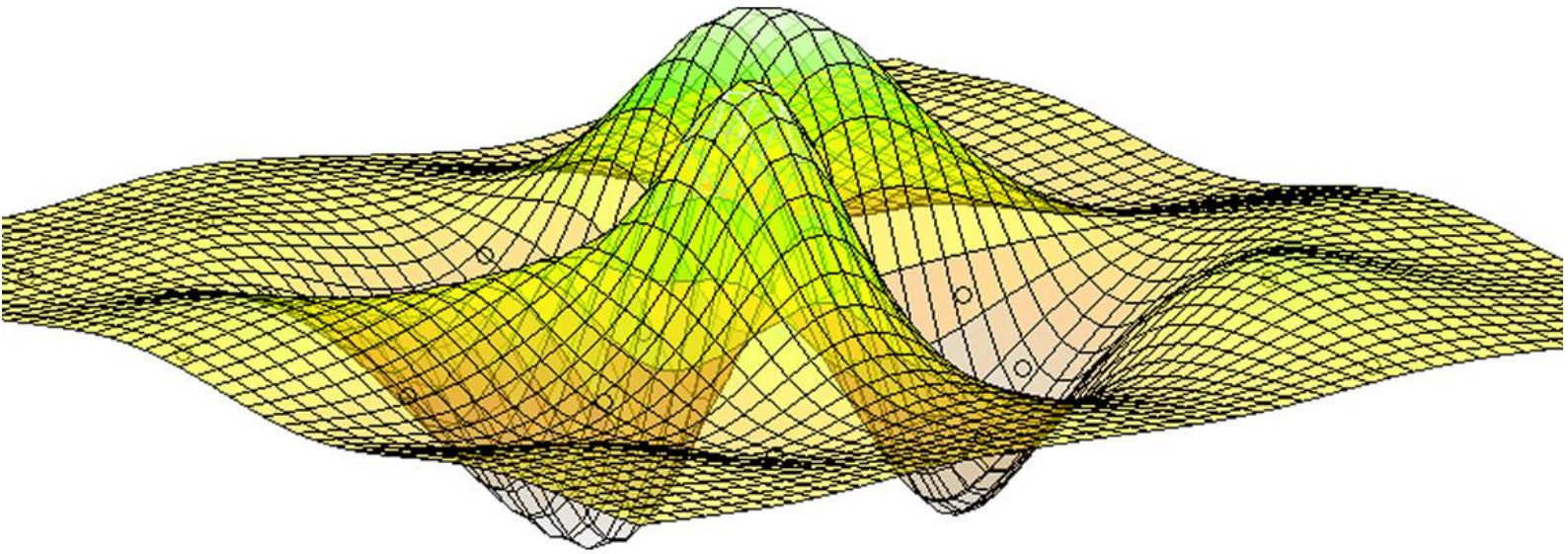

ISSN 2184-8971
Volume 2, Issue 1

PUBLICAÇÕES ISEP
European Commission | Horizon 2020 European Union funding for Research & Innovation
OpenAIRE
zenodo

Journal of Computation and Artificial Intelligence in Mechanics and Biomechanics

Editorial overview by
Editor in chief: Jorge Belinha [1]

[1]*School of Engineering, Polytechnic of Porto (ISEP), Department of Mechanical Engineering, Portugal, job@isep.ipp.pt*

Journal of Computation and Artificial Intelligence in Mechanics and Biomechanics (JCAIMB) is a scholarly online peer review free open access journal fully sponsored by "Publicações ISEP". All manuscripts are available in the ZENODO repository database, from OpenAIRE project, allowing an automatically abstracting and indexation and free open access.

Thus, JCAIMB is committed to ensure free Open Science to both authors and readers and to publish only quality works, which are reviewed by experts in related field. Moreover, JCAIMB aims to publish quality original research works, following the scientific method of scholarly value in computational mechanics and biomechanics combined with several degrees of artificial intelligence, whose formulations and applications are properly demonstrated and validated. Nevertheless, innovative applications using commercial software packages are encouraged, as well as original and up-to-date revision manuscripts. In this issue, four manuscripts are published in JCAIMB:

- Finite element simulations of the electro-chemomechanical behavior of articular cartilage. Part I: theoretical formulation, by Mariana Bento, Fernando M.F. Simões and Benjamin Loret;
- Finite element simulations of the electro-chemomechanical behavior of articular cartilage. Part II: results and discussion, by Mariana Bento, Fernando M.F. Simões and Benjamin Loret;
- Structural analysis of the new Bioactive Kinetic Screw in titanium alloy vs. commercially pure titanium, by Carlos Aurelio Andreucci, Elza M. M. Fonseca and Renato N. Jorge;
- Structural analysis of healthy and degenerated intervertebral discs using meshless methods, by Rita Almeida and Jorge Belinha.

Enjoy.

The editorial team.

Technical information:

Publisher:	Publicações ISEP - https://publicacoes.isep.ipp.pt/
Repository:	ZENODO repository database - https://zenodo.org/
Licence:	under the terms of the Creative Commons Attribution 4.0 International (CC BY 4.0) license.
Director:	Jorge Belinha
Email:	job@isep.ipp.pt
Format:	Online: https://publicacoes.isep.ipp.pt/jcaimb
Periodicity:	Semestrial

Journal of Computation and Artificial Intelligence in Mechanics and Biomechanics ISSN 2184-8971
Volume 2, Issue 1, Page 1-16, 2022

Finite element simulations of the electro-chemo-mechanical behavior of articular cartilage. Part I: theoretical formulation

Mariana Bento[1], Fernando M.F. Simões[2], Benjamin Loret[3]

[1] *Instituto Superior Técnico, University of Lisbon, mariana.bento@tecnico.ulisboa.pt; Av. Rovisco Pais,1;Lisboa;Portugal*
[2] *CERIS and Instituto Superior Técnico, University of Lisbon, fernando.simoes@tecnico.ulisboa.pt; Av. Rovisco Pais,1;Lisboa;Portugal*
[3] *Laboratoire 3SR, Université Grenoble Alpes, Benjamin.Loret100@gmail.com; Domaine universitaire BP53, 38041 Grenoble Cedex 9; France*

Abstract
Articular cartilage is a porous medium, reinforced by collagen fibers and saturated by an aqueous electrolyte. The presence of electrically charged macromolecules, the proteoglycans, leads to electro-chemo-mechanical interactions in the tissue which enhance its adaptation to physiological requests. In the present work, a new finite element formulation is presented and a finite element program is developed, with the purpose of numerically simulate the response of an articular cartilage sample to a combination of chemical and mechanical actions. The model considers the distinct physiological and mechanical roles of the fluid in the intrafibrillar and extrafibrillar compartments. As a new feature, the presence of the intrafibrillar fluid is taken into account in a straightforward manner based on experimental observations. Parametric identification and simulations of actual loading processes are described in part II of this paper.

***DOI**: 10.5281/zenodo.7405999*

Article Info

Keywords
Articular cartilage
Osteoarthritis
Electro-chemo-mechanical couplings
Finite element method

Article History
Received: *19/05/2022*
Revised: *06/07/2022*
Accepted: *01/11/2022*

1. Introduction

Synovial joints are a specific group of joints in the human body that present a fibrous capsule filled by a fluid rich in nutrients (the synovial fluid) which nourishes a thin layer of articular cartilage that covers the extremities of the bones and provides frictionless movements in the joint [1],[2]. Articular cartilage is a highly specialized connective tissue, lacking nerves and blood vessels, characterized as a porous medium structured by collagen fibers (mostly of type II) and saturated by an electrolyte (representing 60% to 85% of the total volume of the tissue) with water as solvent and metallic ions as solutes [2-5]. Charged macromolecules, the proteoglycans (PG), intermingled with collagen fibers, give rise to electro-chemo-mechanical couplings that allow moderate deformation to take place and ensure an optimal adaptation of the tissue to physiological loads. Collagen and PGs are, thus, the main components of the extracellular matrix (ECM), responsible for the support of the stresses resulting from the forces in the joints and, together with water and dissolved inorganic salts, determine the complex behavior of the tissue that we wish to model in a macroscopic continuum framework. The cells present in the tissue (the chondrocytes) which are responsible for both the production and degradation of the ECM, being in this way in charge for its maintenance and repair, represent just 2% to 10% of the adult cartilage volume [3],[4].

Collagen is a fundamental protein with the tropocollagen molecule as its basic unit. Each tropocollagen unit is composed by three polypeptide chains that coil around each other forming a triple helix. The subsequent polymerization of the tropocollagen molecules originates collagen fibrils that, when grouped together, create a collagen fiber. The triple helix configuration, in addition to the covalent cross links that can be formed between the fibrils, provide collagen and the tissue with its tensile (stiffness and strength) properties [4].

Proteoglycans are composed by a protein core attached to several glycosaminoglycan (GAG) chains, which may further aggregate through a non-covalent protein linkage to a hyaluronan (HA) molecule. According to its GAG composition, different types of proteoglycans may be found among the tissue; aggrecan, the most abundant one, is gifted with the greatest capability to interact with HA molecules through the link protein [3],[4]. The link protein provides stabilization to the PGs aggregation, contributing to the immobilization of PGs within the collagen network, which has a major importance in the normal function of articular cartilage [3]. Under physiologic conditions, the GAG chains are negatively charged due to the presence of sulfate and carboxyl groups and the high number of fixed negative charges

Corresponding Author
Fernando M.F. Simões
fernando.simoes@tecnico.ulisboa.pt

(the fixed charge density - FCD) causes electrostatic repulsive forces between these molecules. The existence of these forces plays an important role in the tissue compressive stiffness since, when a compressive force is applied, the repulsion between the PG molecules opposes the movement and, therefore, if the number of PGs in the cartilage tissue increases, the FCD and the compressive stiffness increase as well [3].

The system comprising the tissue and the synovial fluid tends to evolve in order to achieve chemical balance. For instance, if the salt concentration (*e.g.* NaCl, $CaCl_2$) in the synovial fluid increases (hypertonic solution), a higher amount of ionic species is attracted inside the tissue according to Donnan's osmotic effect. Inside the tissue, these counter-ions shield the electrostatic repulsive forces between PGs and, consequently, allow for a higher contractive deformation or, equivalently, a lower compressive stiffness of the tissue [3]. By the contrary, in the presence of a hypotonic surrounding medium, less cations will also be present inside the tissue, leading to higher repulsive forces between PGs, lower contractive deformations and higher compressive stiffness [6]. The chemical composition of the synovial fluid has, additionally, an impact on the level of swelling and hydration of the tissue. According to the osmotic effect, water tends to flow from a medium with lower concentration of ions to a medium with higher concentration. In this way, due to the fact that the PG molecule is negatively charged and counter-ions are always present inside the tissue, in the presence of a hypotonic surrounding medium, an osmotic flow is generated leading to the migration of water from the hypotonic region (outside the tissue) towards the hypertonic region (inside), contributing to the swelling of the tissue [7]. However, when the surrounding medium is hypertonic (with higher concentration of salt), the tissue loses water and shrinks [6].

The fluid part of cartilage is therefore a vital component of the tissue, since it is responsible not only for the exchange of nutrients and waste products between the chondrocytes and the synovial fluid in the joint, but it also plays an important role in defining the mechanical response of the cartilage due to the presence of dissolved inorganic free cations such as Na^+ and Ca^{2+}, which balance the proteoglycan negative charges. Within the cartilage tissue, water may be found, besides inside the cells, in two different locations: (a) in the intrafibrillar (IF) space, inside the collagen fibers (between the collagen fibrils) or (b) in the extrafibrillar (EF) space, outside the collagen fibers and covering the proteoglycan molecules. In both spaces, part of the water is free to move when some load (*e.g.* compressive force) is applied or due to the presence of an osmotic pressure [3,4,8].

As any other tissue of the body, during the natural aging process of life, the cartilage tissue may suffer modifications in the ECM, due to alterations in the normal function of the chondrocytes, that lose their full capacity to synthesize the ECM components [9], [10]. Osteoarthritis is a disease characterized by the loss of articular cartilage in the joints (decrease of its thickness) due to an unbalance between synthesis and degradation of the cartilage components (promotion of the cells' catabolic process over the anabolic), culminating in altered biomechanics. Therefore, the understanding and knowledge of the tissue behavior and its evolution through age is crucial in the improvement of prevention and treatment of the degenerative pathologies that may affect the cartilage tissue as well as in the development of novel engineered materials to be used in regenerative medicine.

Over the past years, several chemo-mechanical models have been proposed to capture various aspects of articular cartilage response. In a work conducted by Mow *et al.* [11], the cartilage tissue was considered as a combination of a fluid and a solid phase. In such model, the collagen matrix, along with the proteoglycans, compose the solid phase of a matrix considered to be a porous, permeable medium. The fluid phase accounted for the interstitial fluid, being both phases incompressible. The triphasic model, proposed by Lai *et al.* [12], is an extension of the latter biphasic model, where the cartilage tissue is now decomposed into three phases: an incompressible interstitial fluid phase, accounting for the presence of water, an ionic phase composed by the ionic species Na^+ and Cl^- (addition relatively to the biphasic model), and an incompressible solid phase, comprising the collagen and proteoglycan molecules of the porous-permeable ECM. The model was later generalized to include multi-electrolytes [13].

According to the experimental observations by Maroudas *et al.* [8], the presence of water in two distinct compartments of the tissue is significant for the mechanical aspects of its response. Along this perspective, Huyghe [14] and Loret and Simões [15-17] proposed a three phase electro-chemo-mechanical model with one solid and two fluid phases. In the latter model, the EF fluid phase included the EF water, the charged proteoglycans and dissolved ions, while the IF fluid phase was constituted by the IF water along with dissolved salts. The collagen fibers are the components of the solid phase. Water and ions of the IF phase have first to transfer through the collagen wall to reach the EF phase, being the latter the one that communicates with the external environment. In order to model the exchanges of mass between the two fluid phases and between the EF compartment and the surrounding medium, equations of mass transfer, together with the generalized diffusion equations developed in [18], were implemented in the simulation of the mechanical response of the tissue using the finite element method [19]. The consideration in these models of two fluid phases may be particularly important when studying osteoarthritis since collagen fibers, which become damaged in a osteoarthritic

cartilage, act in the model like membranes between these two compartments. Although quite complete, the model by Loix *et al.* [19] requires the definition of several material parameters that cannot be obtained from the existing experimental data, including the characteristic transfer times between the IF and EF phases (the mass transfer between phases is not instantaneous) and the parameters related to the difference of the pressure of water in these phases. Moreover, with this model, the authors were not able to replicate the experimental results by Eisenberg and Grodzinsky [6]. Nonetheless, the model used in [19] introduces, for the first time, the notion of *fictitious bath* or *equilibrium bath* that is used to define the articular cartilage mechanical parameters.

The finite element formulation proposed in this paper follows the framework of the model by Loix *et al.* [19], that is, a three phase model is also considered, with one solid phase and two fluid phases, accounting for the presence of two water compartments (EF and IF phases). However, as new features of the present formulation: 1) the electro-chemo-mechanical constitutive law used in this work is defined in [20], which is different from the one used by Loix *et al.* [19] and 2) the contribution of the IF phase to the simulations is considered in a different and simplified way, not requiring the definition of IF material parameters and functions. In fact, according to Basser *et al.* [21], during a compression test in a specimen extracted from the hip, the percentage of IF water varied from 23.32% to 27.80% of the total amount of water, in all the stages of the test. Thus, a fixed value of 25% is considered in this work for the percentage of IF water with respect to the total amount of water, and consequently, the percentage attributed to the EF part is the remaining 75%. Exchange of mass (ions and water) between the EF phase and the environment surrounding the tissue (bath/synovial fluid) through boundary membranes, always guaranteeing the equilibrium at the interface between the exterior and interior of the tissue, is taken into account as well as diffusion of the ionic species within the EF phase. Only the presence of Na^+ and Cl^- is considered in this model since NaCl is the most abundant salt in the tissue [3]. As a simplification over [15-17] and [19], exchange of ions between the two fluid phases, although existing, is not modelled and, therefore, there is no access to the values of the masses of the IF ionic species. Proteoglycans, being macromolecules, do not pass through the membranes, thus they only exist in the EF phase.

Following this formulation, a finite element program is developed in MATLAB environment with the purpose of numerically simulate the response of an articular cartilage sample to a combination of chemical and mechanical actions. Parametric identification and simulations of actual loading processes are described in part II of this paper.

2. Field and constitutive equations

2.1. Mass and volume measures

The cartilage sample is a multi-phase tissue, being as well a multi-species mixture, composed by water (w), sodium (Na^+), chloride (Cl^-), among others. In this work, two distinct phases will be directly modelled: the EF fluid phase, $E=\{w,PG,Cl^-,Na^+\}$, and the solid phase, composed by the cartilage fibers, $S=\{c\}$. The EF phase may be further divided in two distinct subsets: one composed by the mobile species, $E^{mo} = \{w, Cl^-, Na^+\}$, and one composed only by the ionic species, $E^{ions} = \{Cl^-, Na^+\}$.

In this way, two types of constitutive equations are required to describe the tissue behavior: electro-chemo-mechanical equations, which account for deformation, and generalized diffusion equations, describing the flow of the ionic species and water through the extrafibrillar phase.

During the development of the field and constitutive equations, that will be conducted further ahead, several mass and volume quantities in the EF phase will be used, which need therefore to be defined *a priori*. The current volume, the current mass and the current number of moles of the species k in the EF phase will be denoted as V_{kE}, M_{kE} and N_{kE}, respectively. Considering V_0 the initial volume of the porous medium, and V and V_E the current total and EF volumes, several other entities related to the species k in this phase may be defined:

- some are intrinsic, like the intrinsic density $\rho_k = M_{kE}/V_{kE}$, the molar volume $\hat{v}_k = V_{kE}/N_{kE}$ and the molar mass $\hat{m}_k = M_{kE}/N_{kE}$ related by $\rho_k = \hat{m}_k / \hat{v}_k$;
- some refer to the current volume, like the volume fraction $n^{kE} = V_{kE}/V$ and the apparent density $\rho^{kE} = n^{kE} \rho_k = M_{kE}/V$;
- some refer to the initial volume, like the mass content $m^{kE} = M_{kE}/V_0$, the volume content $v^{kE} = V_{kE}/V_0 = m^{kE}/\rho_k$ and the molar content $\mathcal{N}_{kE} = N_{kE}/V_0$;
- and some are defined in the EF phase, like the molar concentration $c_{kE} = N_{kE}/V_E$ and the molar fraction $x_{kE} = N_k/\Sigma_k N_{kE}$.

All the entities described above can also be obtained for the EF phase as a whole by summing the contributions of all the species: volume content $v^E = \Sigma_k\, v^{kE}$, volume fraction $n^E = \Sigma_k\, n^{kE}$, total number of moles $N_E = \Sigma_k\, N_{kE}$ and molar content $\mathcal{N}_E = \Sigma_k\, \mathcal{N}_{kE} = N_E/V_0$.

2.2. Mass and momentum balances

The mass balance equation of mobile EF species (water and ionic species) can be written as [22]

$$\frac{\mathrm{d}m^{kE}}{\mathrm{d}t} + \mathrm{div}\boldsymbol{M}_{kE} = 0, \quad k \in E^{mo}, \tag{1}$$

where $\boldsymbol{M}_{kE}$ is the mass flux of the species through the solid skeleton defined as

$$\rho_k^{-1}\boldsymbol{M}_{kE} = n_{kE}(\boldsymbol{v}_{kE} - \boldsymbol{v}_S), \tag{2}$$

where $\boldsymbol{v}_{kE}$ is the velocity of species k and $\boldsymbol{v}_S$ is the solid skeleton velocity. Eq.(1) reflects the fact that the change of mass of the fluid phase species k is due to the mass exchange with the surroundings.

Dividing Eq.(1) by ρ_k, we obtain

$$\frac{\mathrm{d}v^{kE}}{\mathrm{d}t} + \mathrm{div}\boldsymbol{J}_{kE} = 0, \tag{3}$$

where $\boldsymbol{J}_{kE}$ is the species volume flux through the solid skeleton

$$\boldsymbol{J}_{kE} = \rho_k^{-1}\boldsymbol{M}_{kE} = n_{kE}(\boldsymbol{v}_{kE} - \boldsymbol{v}_S). \tag{4}$$

Assuming that the solid skeleton and all the EF species are incompressible, the change of volume of the tissue is symmetric to the change of the volume of the fluid phase due to diffusion, that is

$$\mathrm{div}\,\boldsymbol{v}_S + \mathrm{div}\,\boldsymbol{J}_E = \boldsymbol{0}, \tag{5}$$

where $\boldsymbol{J}_E = \Sigma_{k\in E}\,\boldsymbol{J}_{kE}$, which is obtained summing up Eq.(4) for all the EF species and assuming that the velocity of the proteoglycans is equal to the solid phase velocity.

Neglecting body forces and dynamic effects, the balance of momentum equation is

$$\mathrm{div}\,\boldsymbol{\sigma} = \boldsymbol{0}, \tag{6}$$

where $\boldsymbol{\sigma}$ is the total Cauchy stress tensor.

2.3. The global structure of the constitutive equations

The global structure of the constitutive equations was previously developed, in a thermodynamic framework, in [23]. In such framework, the Clausius-Duhem inequality, neglecting thermal effects and considering the contribution of just one fluid phase (in this work the IF phase is indirectly taken into account), results in an expression that contains two terms of distinct natures and which, consequently, are required to be positive individually:

$$\begin{cases} \dot{D}_1 = -\dot{W} + \boldsymbol{S}:\dot{\boldsymbol{E}} + \displaystyle\sum_{k\in E} g_{kE}^{ec}\,\dot{\mathcal{N}}_{kE} \geq 0 \\ \dot{D}_2 = -\displaystyle\sum_{k\in E} \frac{\boldsymbol{\nabla} g_{kE}^{ec}}{\hat{v}_k}.\boldsymbol{J}_{kE} \geq 0\,. \end{cases} \tag{7}$$

2.3.1. Electro-chemo-mechanical constitutive equation

Considering articular cartilage as a hyperelastic material, the first term $\dot{D}_1$ in Eq.(7) is considered to exactly vanish, that is

$$\dot{W} = \boldsymbol{S}:\dot{\boldsymbol{E}} + \sum_{k\epsilon E} g_{kE}^{ec}\dot{\mathcal{N}}_{kE}, \tag{8}$$

where ($\dot{}$) denotes a time derivative, $W=W(\boldsymbol{E}, \mathcal{N}_{kE})$ is the internal energy per unit of initial (reference) volume V_0, $\boldsymbol{S}$ is the 2nd Piola-Kirchhoff stress tensor, $\boldsymbol{E}$ is the Green-Lagrange strain tensor ($\boldsymbol{E} = ½ (\boldsymbol{F}^{\mathrm{T}}\boldsymbol{F}- \boldsymbol{I})$, where $\boldsymbol{F}$ is the gradient of deformation tensor) and g_{kE}^{ec} is the electro-chemical potential per unit of mole of species k.

Additionally, for the formulation of the equations that govern the tissue deformation, two constraints need to be included: the electroneutrality and incompressibility conditions. The electroneutrality condition introduces a constraint in the constitutive equation, that incrementally can be written as:

$$\dot{I}_{el} = F\sum_{k\epsilon E} \xi_k \dot{\mathcal{N}}_{kE} = 0, \tag{9}$$

where F is Faraday's constant (F = 96485 Coulomb mol^{-1}) and ξ_k is the valence of species k. The incompressibility of all the tissue constituents introduces a second constraint in the constitutive equations, that incrementally can be written as:

$$\dot{I}_{inc} = \dot{J} - \sum_{k\epsilon E} \hat{v}_k \dot{\mathcal{N}}_{kE} = \det\boldsymbol{F}\,\boldsymbol{F}^{-\mathrm{T}}:\dot{\boldsymbol{F}} - \sum_{k\epsilon E} \hat{v}_k \dot{\mathcal{N}}_{kE}, \tag{10}$$

where $J = V/V_0 = \det \boldsymbol{F}$.

In order to satisfy the two aforementioned constraints, an augmented internal energy $\mathcal{W}$ is defined, that results from the introduction of the Lagrange multipliers ϕ_E and p_E interpreted, respectively, as the electrical potential and the pressure in the fluid EF phase

$$\mathcal{W} = W(\boldsymbol{E}, \mathcal{N}_{kE}) - \phi_E I_{el} + p_E I_{inc}\,, \tag{11}$$

from which results

$$\begin{aligned}\dot{\mathcal{W}} &= \boldsymbol{S}:\dot{\boldsymbol{E}} + \textstyle\sum_{k\epsilon E} g_{kE}^{ec}\dot{\mathcal{N}}_{kE} - \phi_E F \sum_{k\epsilon E}\xi_k\dot{\mathcal{N}}_{kE} + p_E\,(\det\boldsymbol{F}\,\boldsymbol{F}^{-\mathrm{T}}:\dot{\boldsymbol{F}} - \textstyle\sum_{k\epsilon E}\hat{v}_k\dot{\mathcal{N}}_{kE}) \\ &= \bar{\boldsymbol{S}}:\dot{\boldsymbol{E}} + \textstyle\sum_{k\epsilon E}\bar{g}_{kE}^{ec}\dot{\mathcal{N}}_{kE}\end{aligned} \tag{12}$$

where $\bar{\boldsymbol{S}} = \boldsymbol{S} + p_E \det\boldsymbol{F}\,\boldsymbol{F}^{-1}{:}\boldsymbol{F}^{-\mathrm{T}}$ and $\bar{g}_{kE}^{ec} = g_{kE}^{ec} - \hat{v}_k\,p_E - F\,\xi_k\,\phi_E$ are the effective 2nd Piola-Kirchhoff stress tensor and the effective electro-chemical potential per unit of mole of species k, respectively.

Since $\dot{\mathcal{W}}$ is also given by

$$\dot{\mathcal{W}} = \frac{\partial\mathcal{W}}{\partial\boldsymbol{E}}:\dot{\boldsymbol{E}} + \sum_{k\epsilon E}\frac{\partial\mathcal{W}}{\partial\mathcal{N}_{kE}}\dot{\mathcal{N}}_{kE}\,, \tag{13}$$

the coupled electro-chemo-hyperelastic constitutive equations are obtained from $\bar{\boldsymbol{S}} = \partial\mathcal{W}/\partial\boldsymbol{E}$ and $\bar{g}_{kE}^{ec} = \partial\mathcal{W}/\partial\mathcal{N}_{kE}$, subjected to the constraints $I_{inc} = \partial\mathcal{W}/\partial p_E = 0$ and $I_{el} = \partial\mathcal{W}/\partial\phi_E = 0$.

As in [20], the constitutive form of the energy $\mathcal{W}$ here proposed is decomposed into a coupled chemo-mechanical contribution and a purely chemical contribution, $\mathcal{W} = \mathcal{W}_{ch\text{-mech}} + \mathcal{W}_{ch}$. The coupled chemo-mechanical contribution is, in turn, decomposed into a coupled chemo-mechanical term $\mathcal{W}_{\text{ch-mech},1}(\boldsymbol{E}, \mathcal{N}_{kE}) = -\,p_{ch}(\mathcal{N}_{kE})\,(\det\boldsymbol{F} - 1)$ and by a product of a purely chemical term $\mathcal{W}_{ch,2}(\mathcal{N}_{kE})$ by a purely mechanical term $\mathcal{W}_{mech}(\boldsymbol{E})$, corresponding to the strain energy of the tissue matrix (PGs, collagen and other proteins), as

$$\mathcal{W}_{ch\text{-}mech}(\boldsymbol{E}, \mathcal{N}_{kE}) = \mathcal{W}_{ch\text{-}mech,1}(\boldsymbol{E}, \mathcal{N}_{kE}) + \mathcal{W}_{ch,2}(\mathcal{N}_{kE})\mathcal{W}_{mech}(\boldsymbol{E}). \tag{14}$$

The purely chemical term is given by:

$$\mathcal{W}_{ch}(\mathcal{N}_{kE}) = RT\left(\sum_{k\epsilon E} \mathcal{N}_{kE} \ln N_{kE} - \mathcal{N}_E \ln N_E\right), \tag{15}$$

where T is the temperature and R is the gas constant (R = 8.314 J mol^{-1} K^{-1}).

The mole based electro-chemical potentials of the species are then obtained as follows:

$$g^{ec}_{kE} = \frac{\partial \mathcal{W}}{\partial \mathcal{N}_{kE}} + \hat{v}_k\, p_E + F\,\xi_k \phi_E = \frac{\partial \mathcal{W}_{ch\text{-}mech}}{\partial \mathcal{N}_{kE}} + RT \ln x_{kE} + \hat{v}_k\, p_E + F\,\xi_k \phi_E, \tag{16}$$

which, in the absence of chemo-mechanical couplings ($\partial \mathcal{W}_{ch\text{-}mech}/\partial \mathcal{N}_{kE}$ = 0), present their classical form, composed by a mechanical ($\hat{v}_k\, p_E$), a chemical ($RT \ln x_{kE}$) and an electrical ($F\xi_k\, \phi_E$) term.

As usual, in the definition of the electro-chemical potentials of the ionic species, only the chemical and electrical terms are retained, thus:

$$g^{ec}_{kE} = RT \ln x_{kE} + F\,\xi_k \phi_E, \quad k\epsilon E^{ions}. \tag{17}$$

In the case of the electrically neutral water molecule, its electro-chemical potential, neglecting again the chemo-mechanical couplings, is defined as:

$$g^{ec}_{wE} = \hat{v}_w\, p_E + RT \ln x_{wE}. \tag{18}$$

The Cauchy stress tensor is also obtained as [20]:

$$\boldsymbol{\sigma} = \frac{1}{\det \boldsymbol{F}}\, \boldsymbol{F}\boldsymbol{S}\boldsymbol{F}^{\mathrm{T}} = \frac{1}{\det \boldsymbol{F}} \boldsymbol{F} \frac{\partial \mathcal{W}_{ch\text{-}mech}}{\partial \boldsymbol{E}} \boldsymbol{F}^{\mathrm{T}} - p_E \boldsymbol{I} = -p_{ch}\boldsymbol{I} + \mathcal{W}_{ch,2}\, \mathbb{E}\!:\!\boldsymbol{E} - p_E \boldsymbol{I}, \tag{19}$$

where $\boldsymbol{F}\, \partial \mathcal{W}_{mech}/\partial \boldsymbol{E}\, \boldsymbol{F}^{\mathrm{T}}/\det \boldsymbol{F} = \mathbb{E}\!:\!\boldsymbol{E}$. Rewriting Eq.(19), we get:

$$\boldsymbol{\sigma} + p_E \boldsymbol{I} = -p_{ch}\boldsymbol{I} + \mathcal{W}_{ch,2}\, \mathbb{E}\!:\!\boldsymbol{E}, \tag{20}$$

where $\mathbb{E}$ is the 4th rank mechanical constitutive tensor of the tissue immersed in a saturated bath and $\boldsymbol{I}$ is the 2nd order identity tensor. In the absence of chemo-mechanical couplings (p_{ch} = 0 and $\mathcal{W}_{ch,2}$ = 1), the classical constitutive equation of an inert porous medium is obtained, $\boldsymbol{\sigma} + p_E\, \boldsymbol{I} = \mathbb{E}\!:\!\boldsymbol{E}$. Therefore, the first chemo-mechanical term $\mathcal{W}_{ch\text{-}mech,1}$ gives rise to an isotropic chemical stress $p_{ch}\, \boldsymbol{I}$, while the term $\mathcal{W}_{ch,2}$ is intended to amplify the stiffness of the tissue for small ionic concentrations, thus reflecting the shielding effect [6].

In order to obtain the final form of the constitutive equation, the concept of *fictitious bath* or *equilibrium bath* needs to be introduced, that is a bath whose composition and pressure $\tilde{p}_B$ may vary in time and space so that, at any time, it is in electro-chemical equilibrium with any point of the tissue. Thus, the pressure p_E can be defined as $p_E = \tilde{p}_B + \tilde{\pi}_{osm}$, where $\tilde{\pi}_{osm}$ is the osmotic (or Donnan) pressure between the tissue's point and the corresponding fictitious bath. Therefore, the constitutive equation Eq. (20) can be written as:

$$\boldsymbol{\sigma} + \tilde{p}_B \boldsymbol{I} + \tilde{\pi}_{osm}\boldsymbol{I} + p_{ch}\boldsymbol{I} = \mathcal{W}_{ch,2}\, \mathbb{E}\!:\!\boldsymbol{E}. \tag{21}$$

Since the properties of the fictitious bath are obtained from those of the tissue, the osmotic pressure $\tilde{\pi}_{osm}$ can be seen as a function of the primary variables and, therefore, it is eligible to enter in the constitutive equation. Due to the fact that the osmotic pressure $\tilde{\pi}_{osm}$ varies with the ionic concentration, it will be used to define both p_{ch} and $\mathcal{W}_{ch,2}$. In this sense, the following expressions are suggested in [20]:

$$p_{ch} = \alpha_p \, \tilde{\pi}_{osm}, \tag{22}$$

$$\mathcal{W}_{ch,2} = 1 + \alpha_w \, \tilde{\pi}_{osm}, \tag{23}$$

where α_p and α_w are chemo-mechanical parameters, with α_p being non-dimensional.

It is important to notice that when the composition of the tissue is uniform and the tissue is in equilibrium with an external bath of known pressure and chemical composition, $\tilde{p}_B$ and $\tilde{\pi}_{osm}$ become the real bath (p_B) and osmotic (π_{osm}) pressures (the fictitious bath then becomes the real one), and the fluid pressure at any point of the tissue is:

$$p_E = p_B + \pi_{osm} \tag{24}$$

However, when there is no equilibrium, the pressure p_E and the chemical composition are obtained, at every time, from the primary variables and never from the properties of the surrounding bath, since those properties are not constitutive, and, thus, should not be involved in the definition of the constitutive equation. The notion of *fictitious bath* is then particularly useful during transient states (*e.g.* when changes of the chemical composition of the bath occur) or when the external bath is inhomogeneous.

2.3.2. Generalized diffusion equation

In [18], two equivalent forms of the generalized diffusion equations, that satisfy the dissipation inequality $D_2 \geq 0$ in Eq.(7), were proposed. The first one relates the vector $\boldsymbol{j}$, containing the volume fluxes of the species in the fluid phase relative to the solid phase, with the vector $\boldsymbol{f}$ of their electro-chemical gradients by an isotropic, semi-definite positive, generalized diffusion matrix $\boldsymbol{\kappa}$:

$$\boldsymbol{j} = -\boldsymbol{\kappa}\boldsymbol{f}, \tag{25}$$

where

$$\boldsymbol{j} = \begin{Bmatrix} \boldsymbol{J}_{wE} \\ \boldsymbol{J}_{NaE} \\ \boldsymbol{J}_{ClE} \end{Bmatrix}, \qquad \boldsymbol{f} = \begin{Bmatrix} \rho_w \boldsymbol{\nabla}\mu^{ec}_{wE} \\ \rho_{Na} \boldsymbol{\nabla}\mu^{ec}_{NaE} \\ \rho_{Cl} \boldsymbol{\nabla}\mu^{ec}_{ClE} \end{Bmatrix} \quad \text{and} \quad \boldsymbol{\kappa} = \begin{bmatrix} \kappa_{ww} & \kappa_{wNa} & \kappa_{wCl} \\ \kappa_{Naw} & \kappa_{NaNa} & \kappa_{NaCl} \\ \kappa_{Clw} & \kappa_{ClNa} & \kappa_{ClCl} \end{bmatrix}. \tag{26}$$

In Eq.(26), the electro-chemical potentials μ^{ec}_{kE} are related to the electro-chemical potentials per unit of mole by $\mu^{ec}_{kE} = g^{ec}_{kE}/\hat{m}_k$.

The second proposed form relates the vector $\boldsymbol{J}$, containing the volume flux of the water, the diffusive fluxes of the ionic species $\boldsymbol{J}^d_k = n^{kE}(\boldsymbol{v}_{kE} - \boldsymbol{v}_{wE})$ and the electrical current density within the tissue $\boldsymbol{I}_e$, with the vector $\boldsymbol{F}$, containing the gradients of the fluid pressure, of the molar fractions and of the electric potential, by a matrix $\boldsymbol{K}$:

$$\boldsymbol{J} = -\boldsymbol{K}\boldsymbol{F} \tag{27}$$

where

$$\boldsymbol{J} = \begin{Bmatrix} \boldsymbol{J}_w \\ \boldsymbol{J}^d_{Na} \\ \boldsymbol{J}^d_{Cl} \\ \boldsymbol{I}_e \end{Bmatrix}, \qquad \boldsymbol{F} = \begin{Bmatrix} \boldsymbol{\nabla} p_E - RT\boldsymbol{\nabla} c_{PG} \\ \dfrac{RT}{\hat{v}_{Na}} \boldsymbol{\nabla} \ln x_{NaE} \\ \dfrac{RT}{\hat{v}_{Cl}} \boldsymbol{\nabla} \ln x_{ClE} \\ \boldsymbol{\nabla}\phi_E \end{Bmatrix}. \tag{28}$$

The matrix $\boldsymbol{K}$ governs the coupled motions of water and ionic species inside the tissue that result from Darcy's law of seepage (due to a water pressure gradient), Fick's law of diffusion (due to an ionic concentration gradient) and Ohm's

law of electrical flow (due to an electrical potential gradient). Since the electrical current density $\boldsymbol{I}_e$ is a linear combination of the water volume flux $\boldsymbol{J}_w$ and of the ionic diffusion fluxes $\boldsymbol{J}_k^d$, matrix $\boldsymbol{K}$ is symmetric, isotropic and, at best, positive semi-definite. Its form is given in [18] by:

$$\boldsymbol{K} = \begin{bmatrix} k_{EE} & 0 & 0 & k_e \\ 0 & k_{NaNa}^d & 0 & k_{Nae}^d \\ 0 & 0 & k_{ClCl}^d & k_{Cle}^d \\ k_e & k_{Nae}^d & k_{Cle}^d & \sigma_e \end{bmatrix} \tag{29}$$

where

$$\begin{cases} k_{EE} = \dfrac{K_h}{\rho_w g} \quad \text{is the "short-circuit" permeability,} \\ K_h \quad \text{is the hydraulic conductivity,} \\ k_e = -k_{EE} F \tilde{e}_{PG} \quad \text{is the electro} - \text{osmotic coefficient,} \\ \sigma_e = n^E F \sum\limits_{k \epsilon E^{ions}} c_{kE} u_{kE}^* + k_{EE} F^2 \tilde{e}_{PG}^2 \quad \text{is the electrical conductivity,} \\ k_{kl}^d = \hat{v}_k \hat{v}_l n^E c_{kE} \dfrac{u_{kE}^*}{F} I_{kl} \\ k_{ke}^d = \hat{v}_k n^E c_{kE} u_{kE}^* \mathrm{sgn}(\xi_k) \\ \tilde{e}_{PG} = e_{PG} \dfrac{n^E}{n^{wE}} \approx e_{PG} = \xi_{PG} c_{PG} \quad \text{is the fixed charge density (FCD)} \end{cases} \tag{30}$$

and u_{kE}^* is the effective ionic mobility of species $k \in E^{ions}$ related to the corresponding coefficient of diffusion D_{kE} by the Nernst-Einstein relation $u_{kE} = D_{kE} |\xi_k| F/RT$, being $u_{kE}^* = \tau u_{kE}$,with τ representing the tortuosity factor.

The coefficients of the matrices $\boldsymbol{\kappa}$ and $\boldsymbol{K}$ are related by a compatibility relation, which permits to write the coefficients of $\boldsymbol{\kappa}$ as [18]:

$$\boldsymbol{\kappa} = k_{EE} \begin{bmatrix} 1 & L_{Na} & L_{Cl} \\ L_{Na} & L_{Na}^2 & L_{Na} L_{Cl} \\ L_{Cl} & L_{Na} L_{Cl} & L_{Cl}^2 \end{bmatrix} + \begin{bmatrix} 0 & 0 & 0 \\ 0 & k_{NaNa}^d & 0 \\ 0 & 0 & k_{ClCl}^d \end{bmatrix} \tag{31}$$

where $L_k = n^{kE}/n^{wE}$, $k \in E^{ions}$.

3. Finite element formulation

3.1. Element contributions

The four field equations developed in section 2.2 that need to be satisfied are the balance of momentum, Eq.(6), the global balance of mass, Eq.(5), and the balance of mass of ions Na^+ and Cl^-, Eq.(3). From these equations the four primary unknowns of the formulation are obtained: the displacement of the solid skeleton and the electro-chemical potentials of the EF species (w, Na^+, Cl^-). All other quantities of interest may be deduced from these four primary unknowns.

To formulate the problem in its weak form, the field equations are multiplied by virtual fields ($\delta\boldsymbol{u}$, $\delta\mu$), and integrated by parts over the body V, which results in:

$$\int_V \nabla(\delta \boldsymbol{u}) : \boldsymbol{\sigma}\, \mathrm{d}V = \int_{\partial V} \delta \boldsymbol{u} \cdot \boldsymbol{\sigma} \cdot \hat{\boldsymbol{n}}\, \mathrm{d}S$$
$$\int_V \delta\mu\, \mathrm{div}\, \boldsymbol{v}_S - \nabla(\delta\mu) \cdot \boldsymbol{J}_E\, \mathrm{d}V = -\int_{\partial V} \delta\mu\, \boldsymbol{J}_E \cdot \hat{\boldsymbol{n}}\, \mathrm{d}S \tag{32}$$
$$\int_V \delta\mu\, \frac{\mathrm{d}v^{kE}}{\mathrm{d}t} - \nabla(\delta\mu) \cdot \boldsymbol{J}_{kE}\, \mathrm{d}V = -\int_{\partial V} \delta\mu\, \boldsymbol{J}_{kE} \cdot \hat{\boldsymbol{n}}\, \mathrm{d}S\,, \qquad k \in E^{ions}\,,$$

where $\hat{\boldsymbol{n}}$ is the unit outward normal to the boundary ∂V of the volume V.

The replacement of the virtual fields in Eq.(32), in each finite element, by its approximation with the shape functions $\boldsymbol{\psi}_u$ and $\boldsymbol{\psi}_\mu$ results in the non-linear first order semi-discrete equation

$$F^{int} = F^{ext}, \tag{33}$$

where F^{int} and F^{ext} are obtained by assembling the element contributions F_e^{int} and F_e^{ext} below

$$F_e^{int} = \begin{Bmatrix} \int_{V^e} \boldsymbol{B}_u^{\mathrm{T}} \boldsymbol{\sigma}\, \mathrm{d}V^e \\ \int_{V^e} \boldsymbol{\psi}_\mu^{\mathrm{T}}\, \mathrm{div}\, \boldsymbol{v}_S - \nabla \boldsymbol{\psi}_\mu^{\mathrm{T}}\, \boldsymbol{J}_E\, \mathrm{d}V^e \\ \int_{V^e} \boldsymbol{\psi}_\mu^{\mathrm{T}}\, \frac{\mathrm{d}v^{NaE}}{\mathrm{d}t} - \nabla \boldsymbol{\psi}_\mu^{\mathrm{T}}\, \boldsymbol{J}_{NaE}\, \mathrm{d}V^e \\ \int_{V^e} \boldsymbol{\psi}_\mu^{\mathrm{T}}\, \frac{\mathrm{d}v^{ClE}}{\mathrm{d}t} - \nabla \boldsymbol{\psi}_\mu^{\mathrm{T}}\, \boldsymbol{J}_{ClE}\, \mathrm{d}V^e \end{Bmatrix} \text{ and } F_e^{ext} = \begin{Bmatrix} \int_{\partial V^e} \boldsymbol{\psi}_u^{\mathrm{T}}\, \boldsymbol{\sigma} \cdot \hat{\boldsymbol{n}}\, \mathrm{d}S^e \\ -\int_{\partial V^e} \boldsymbol{\psi}_\mu^{\mathrm{T}}\, \boldsymbol{J}_E \cdot \hat{\boldsymbol{n}}\, \mathrm{d}S^e \\ -\int_{\partial V^e} \boldsymbol{\psi}_\mu^{\mathrm{T}}\, \boldsymbol{J}_{NaE} \cdot \hat{\boldsymbol{n}}\, \mathrm{d}S^e \\ -\int_{\partial V^e} \boldsymbol{\psi}_\mu^{\mathrm{T}}\, \boldsymbol{J}_{ClE} \cdot \hat{\boldsymbol{n}}\, \mathrm{d}S^e \end{Bmatrix}. \tag{34}$$

From the element vector of the internal forces F_e^{int}, the element stiffness and diffusion matrices may be retrieved through their definition, $K^{\mathrm{e}} = \partial F_e^{int} / \partial X^{\mathrm{e}}$ and $C^{\mathrm{e}} = \partial F_e^{int} / \partial V^{\mathrm{e}}$, with X^{e} and V^{e} representing, respectively, the vectors of the element degrees of freedom and their time derivatives:

$$X^e = \begin{Bmatrix} \boldsymbol{u} \\ \mu_{wE}^{ec} \\ \mu_{NaE}^{ec} \\ \mu_{ClE}^{ec} \end{Bmatrix}, \quad V^e = \dot{X}^e, \tag{35}$$

$$K^e = \begin{bmatrix} \boldsymbol{K}_{uu}^e & \boldsymbol{K}_{u\mu_w}^e & \boldsymbol{K}_{u\mu_{Na}}^e & \boldsymbol{K}_{u\mu_{Cl}}^e \\ \boldsymbol{0} & \boldsymbol{K}_{\mu_w\mu_w}^e & \boldsymbol{K}_{\mu_w\mu_{Na}}^e & \boldsymbol{K}_{\mu_w\mu_{Cl}}^e \\ \boldsymbol{0} & \boldsymbol{K}_{\mu_{Na}\mu_w}^e & \boldsymbol{K}_{\mu_{Na}\mu_{Na}}^e & \boldsymbol{K}_{\mu_{Na}\mu_{Cl}}^e \\ \boldsymbol{0} & \boldsymbol{K}_{\mu_{Cl}\mu_w}^e & \boldsymbol{K}_{\mu_{Cl}\mu_{Na}}^e & \boldsymbol{K}_{\mu_{Cl}\mu_{Cl}}^e \end{bmatrix}, \tag{36}$$

$$C^e = \begin{bmatrix} \boldsymbol{0} & \boldsymbol{0} & \boldsymbol{0} & \boldsymbol{0} \\ \boldsymbol{C}_{\mu_w u}^e & \boldsymbol{0} & \boldsymbol{0} & \boldsymbol{0} \\ \boldsymbol{C}_{\mu_{Na} u}^e & \boldsymbol{0} & \boldsymbol{C}_{\mu_{Na}\mu_{Na}}^e & \boldsymbol{C}_{\mu_{Na}\mu_{Cl}}^e \\ \boldsymbol{C}_{\mu_{Cl} u}^e & \boldsymbol{0} & \boldsymbol{C}_{\mu_{Cl}\mu_{Na}}^e & \boldsymbol{C}_{\mu_{Cl}\mu_{Cl}}^e \end{bmatrix}. \tag{37}$$

The non-zero components of the matrices K^{e} and C^{e} are then:

$$
\begin{aligned}
\boldsymbol{C}^{e}_{\mu_w u} &= \int_{V^e} \boldsymbol{\psi}^{\mathrm{T}}_{\mu}\, \mathrm{tr}\, \boldsymbol{B}_u \, \mathrm{d}V^e \\
\boldsymbol{C}^{e}_{\mu_k u} &= \int_{V^e} \boldsymbol{\psi}^{\mathrm{T}}_{\mu}\, \frac{3}{4}\frac{v^{kE}}{n^E} z_{kE}\, \mathrm{tr}\, \boldsymbol{B}_u \, \mathrm{d}V^e, \quad k \in E^{ions} \\
\boldsymbol{C}^{e}_{\mu_k \mu_l} &= \int_{V^e} \boldsymbol{\psi}^{\mathrm{T}}_{\mu}\, \frac{\widehat{m}_l}{RT} v^{kE}\, z_{klE} \boldsymbol{\psi}_{\mu} \, \mathrm{d}V^e, \quad k, l \in E^{ions},
\end{aligned}
\tag{38}
$$

$$
\begin{aligned}
\boldsymbol{K}^{e}_{uu} &= \int_{V^e} \boldsymbol{B}^{\mathrm{T}}_{u} \left[(1+\alpha_w \tilde{\pi}_{osm})\mathbf{I} + \left[\left(R_u - \alpha_p Q_u\right)\boldsymbol{I} + \alpha_w Q_u \mathbf{I}\!:\!\boldsymbol{E}\right] \otimes \boldsymbol{I}\right] \boldsymbol{B}_u \, \mathrm{d}V^e \\
\boldsymbol{K}^{e}_{u\mu_l} &= \int_{V^e} \boldsymbol{B}^{\mathrm{T}}_{u} \left[\left[\left(R_l - \alpha_p Q_l\right)\boldsymbol{I} + \alpha_w Q_l \mathbf{I}\!:\!\boldsymbol{E}\right]\widehat{m}_l\right] \boldsymbol{\psi}_{\mu} \, \mathrm{d}V^e \quad , \quad l \in E^{mo} \\
\boldsymbol{K}^{e}_{\mu_w \mu_l} &= \int_{V^e} \boldsymbol{\nabla}\boldsymbol{\psi}^{\mathrm{T}}_{\mu}\, \rho_l \sum\nolimits_{k \in E} \kappa_{kl}\, \boldsymbol{\nabla}\boldsymbol{\psi}_{\mu} \, \mathrm{d}V^e \quad , \quad l \in E^{mo} \\
\boldsymbol{K}^{e}_{\mu_k \mu_l} &= \int_{V^e} \boldsymbol{\nabla}\boldsymbol{\psi}^{\mathrm{T}}_{\mu}\, \rho_l \kappa_{kl} \boldsymbol{\nabla}\boldsymbol{\psi}_{\mu} \, \mathrm{d}V^e \quad , \quad k \in E^{ions}, l \in E^{mo},
\end{aligned}
\tag{39}
$$

where $\boldsymbol{B}_u$ is defined as the strain-displacement matrix, Q_u and Q_l are given by Eq.(A.6) and R_u and R_l are given by Eq.(B.15). To obtain each of the components of the element matrices, it is necessary to resort to the constitutive equations developed in section 2.3, taken additionally into account the manipulations described in detail in Appendix A and Appendix B.

In the finite element simulations presented in this work, a one dimensional bar element, with three nodes (quadratic interpolation) for the displacement unknown and two nodes (linear interpolation) for the electro-chemical potentials, is used. The use of two nodes and linear interpolation for the electro-chemical potentials is motivated by the fact that in classical porous media, in which the nodal degrees of freedom also comprise the water pressure, a linear interpolation is usually used to approximate this variable along the element. In this way, each variable may be approximated, within a generic element *e*, by the predefined shape functions multiplied by the nodal values of the respective variables: $u = [\psi_u]\{u^e\}$ and $\mu_k^{ec} = [\psi_\mu]\{\mu_k^{ec^e}\}$ with

$$
u^e = \begin{Bmatrix} u^1 \\ u^2 \\ u^3 \end{Bmatrix} \text{ and } \mu_k^{ec^e} = \begin{Bmatrix} \mu_k^{ec^1} \\ \mu_k^{ec^2} \end{Bmatrix}.
\tag{40}
$$

In order to obtain the non-zero components of the stiffness and diffusion matrices, the Gaussian quadrature rule is applied, where two integration points are used for both displacement and electro-chemical potentials.

In a 1D (uniaxial strain) analysis, the 4th rank mechanical constitutive tensor $\mathbf{E}$ defined in Eq.(20) and used in Eq.(39), involves just one constitutive parameter (E_{sat}) to be obtained from experimental results.

3.2. Time integration

For the integration of the semi-discrete equations previously developed, both an incremental and an iterative process are performed, where the steps in the incremental process are denoted by *n* and the iterations by *i*. Moreover, a midpoint scheme is used for the time integration, meaning that, for each step *n*+1, the equations are evaluated at time $t_{n+\alpha} = t_n + \alpha\,\Delta t$, with $\alpha = 0.5$, where $\Delta t = t_{n+1} - t_n$.

Within each step *n*+1, several iterations are performed until convergence is reached, which corresponds to a vanishing residual R:

$$
R_{n+\alpha} = F^{ext}(S_{n+\alpha}) - F^{int}(X_{n+\alpha}, V_{n+\alpha}) = 0,
\tag{41}
$$

where $\mathcal{S}$ represents the nodal "loads" and $\mathcal{X}$ and $\mathcal{V}$ represent the vectors of the nodal primary variables (displacement and electro-chemical potentials) and of the nodal velocities of the primary variables, respectively. The quantities $\mathcal{Z} = \mathcal{S}, \mathcal{X}, \mathcal{V}$, evaluated at the time $t_{n+\alpha}$, are defined as $\mathcal{Z}_{n+\alpha} = (1-\alpha)\,\mathcal{Z}_n + \alpha\,\mathcal{Z}_{n+1}$, with $\mathcal{Z}_n$ and $\mathcal{Z}_{n+1}$ the values of $\mathcal{Z}$ evaluated at time t_n and t_{n+1}, respectively.

In the present problem, the internal forces are non-linear functions of the nodal primary unknowns. In this way, a linearization of Eq.(33) around the current solution ($\mathcal{X}^{\,i}$ and $\mathcal{V}^{\,i}$, for $i \geq 1$), through the development of the internal forces into a Taylor series neglecting the higher order terms, results in:

$$\mathcal{F}^{ext}(\mathcal{S}^{i}_{n+\alpha}) - \mathcal{F}^{int}\left(\mathcal{X}^{i+1}_{n+\alpha},\, \mathcal{V}^{i+1}_{n+\alpha}\right) \approx \mathcal{R}^{i+1}_{n+\alpha} - \mathcal{C}^{*}(\alpha\Delta\mathcal{V}) = \mathbb{0}, \tag{42}$$

with $\mathcal{R}^{i+1}_{n+\alpha}$ the residual at step n+1, evaluated at time $t_{n+\alpha}$, and at iteration i+1 which, recalling Eq.(41), has the form

$$\mathcal{R}^{i+1}_{n+\alpha} = \mathcal{F}^{ext}(\mathcal{S}^{i}_{n+\alpha}) - \mathcal{F}^{int}\left(\mathcal{X}^{i}_{n+\alpha},\, \mathcal{V}^{i}_{n+\alpha}\right), \tag{43}$$

where $\mathcal{Z}^{i}_{n+\alpha} = (1-\alpha)\,\mathcal{Z}_n + \alpha\,\mathcal{Z}^{i}_{n+1}$, with $\mathcal{Z} = \mathcal{S}, \mathcal{X}, \mathcal{V}$.

With all the above relations formulated, the iterative process is then conducted as follows:

$$\begin{cases} \text{for } i = 0 & \mathcal{V}^{0}_{n+1} = \mathcal{V}_n\ , \qquad \mathcal{X}^{0}_{n+1} = \mathcal{X}_n + (1-\alpha)\Delta t\,\mathcal{V}_n \\ \text{for } i \geq 1 & \mathcal{V}^{i}_{n+1} = \mathcal{V}^{i-1}_{n+1} + \Delta\mathcal{V}\ , \quad \mathcal{X}^{i}_{n+1} = \mathcal{X}_n + \Delta t\,\mathcal{V}^{i}_{n+\alpha} = \mathcal{X}^{0}_{n+1} + \alpha\Delta t\,\mathcal{V}^{i}_{n+1} \end{cases} \tag{44}$$

where the velocity update $\Delta\mathcal{V}$, in each iteration, is obtained from the linearized equation Eq.(42) where the effective diffusion matrix $\mathcal{C}^{*}$ is defined as:

$$\mathcal{C}^{*} = \mathcal{C} + \alpha\Delta t\mathcal{K} \ \text{ with } \ \mathcal{C} = \frac{\partial \mathcal{F}^{int}}{\partial \mathcal{V}}\left(\mathcal{X}^{i}_{n+\alpha},\, \mathcal{V}^{i}_{n+\alpha}\right),\ \mathcal{K} = \frac{\partial \mathcal{F}^{int}}{\partial \mathcal{X}}\left(\mathcal{X}^{i}_{n+\alpha},\, \mathcal{V}^{i}_{n+\alpha}\right). \tag{45}$$

As the iterative process progresses, it is expected that the system converges until $\Delta\mathcal{V}$ becomes sufficiently small. Thus, the convergence criterion used is the following:

$$||\Delta\widetilde{\mathcal{V}}||^{i}_{n} / ||\Delta\widetilde{\mathcal{V}}||^{0}_{n} \leq TOL, \tag{45}$$

where $||\Delta\widetilde{\mathcal{V}}||^{i}_{n}$ represents the norm of the normalized $\Delta\mathcal{V}$ vector, at step n and iteration i, and TOL represents the threshold which is a very small number.

The normalization of the $\Delta\mathcal{V}$ vector is desirable since either $\mathcal{X}$ and $\mathcal{V}$ are composed of variables (displacements, electro-chemical potentials and their time derivatives) that have different physical dimensions and orders of magnitude. In this way, the components of $\Delta\mathcal{V}$ related to displacements are normalized by the maximum value obtained at iteration 0, and a similar normalization procedure is performed on the components of $\Delta\mathcal{V}$ related to the electro-chemical potentials:

$$\left(\overline{\Delta\mathcal{V}}^{i}_{n}\right)_{u} = \frac{\left(\Delta\mathcal{V}^{i}_{n}\right)_{u}}{\left(\Delta\mathcal{V}^{0}_{n}\right)_{max,u}} \quad \text{and} \quad \left(\overline{\Delta\mathcal{V}}^{i}_{n}\right)_{\mu} = \frac{\left(\Delta\mathcal{V}^{i}_{n}\right)_{\mu}}{\left(\Delta\mathcal{V}^{0}_{n}\right)_{max,\mu}}\ . \tag{46}$$

Once this normalization is performed, the same threshold TOL may be used for both type of variables.

4. Conclusions

Articular cartilage is a porous medium, reinforced by collagen fibers and saturated by an aqueous electrolyte. The presence of proteoglycans (electrically charged macromolecules) is the reason why electro-chemo-mechanical interactions occur, which enhance the tissue adaptation to physiological actions.

In previous works [15,18,20], it was proposed 1) a constitutive law and 2) a generalized diffusion model for articular cartilage. In those models, the collagen fibers constitute the solid phase of the porous medium and the fluid phase is

composed by water, PGs and dissolved inorganic salts (NaCl). In the current work, two fluid compartments are also considered, in order to account for the division of water in the IF and EF spaces inside the tissue, as highlighted in [8]. However, as a new feature, the IF compartment is taken into account in a simplified way, distinct to what was previously considered in [16,17,19,20], but consistent with experimental observations [21]. This simplification avoids the definition of material parameters and functions related to the IF compartment that cannot be obtained from the existing experimental data.

A finite element program, whose formulation is based on the described model, is developed in a MATLAB environment with the purpose of numerically simulate the response of an articular cartilage sample to a combination of chemical and mechanical actions. The parametric identification and simulations of actual loading processes are described in the companion paper.

Appendix A. Osmotic equilibrium and fictitious bath

From the electro-chemical potentials of the ionic species Na^+ and Cl^-, the chemical potential of the salt NaCl may be obtained:

$$g_{NaCl} = g^{ec}_{NaE} + g^{ec}_{ClE} = RT \ln(x_{NaE} x_{ClE}), \tag{A.1}$$

with x_{kE} the molar fraction of the species k in the EF compartment.

The electroneutrality condition of the (*fictitious*) bath requires that $\tilde{x}_{ClB} = \tilde{x}_{NaB}$ (with $\tilde{x}_{ClB}$ and $\tilde{x}_{NaB}$ the molar fractions of the species in the fictitious bath), and the electroneutrality condition of the tissue imposes that $x_{ClE} = x_{NaE} + y_{PG}$ where $y_{PG} = \xi_{PG}\, x_{PG} < 0$. Imposing the chemical equilibrium between the two phases (ficticious bath and cartilage tissue), $\tilde{g}_{NaCl} = g_{NaCl}$, we obtain:

$$x_{NaE} x_{ClE} = \tilde{x}_{NaB} \tilde{x}_{ClB} \quad \text{or} \quad \tilde{x}_{NaB} \tilde{x}_{ClB} = \sqrt{x_{NaE}(x_{NaE} + y_{PG})} \tag{A.2}$$

and

$$\begin{aligned} \tilde{x}_{wB} &= 1 - \tilde{x}_{NaB} - \tilde{x}_{ClB} = 1 - 2\sqrt{x_{NaE}(x_{NaE} + y_{PG})} \\ x_{wE} &\approx 1 - x_{NaE} - x_{ClE} = 1 - 2x_{NaE} - y_{PG}. \end{aligned} \tag{A.3}$$

Note that x_{PG} is neglected in the first equality in Eq.$(A.3)_2$.

From the chemical equilibrium of water ($\tilde{g}_w = g_w$), the fictitious Donnan osmotic pressure is thus defined as:

$$\begin{aligned} \tilde{\pi}_{osm} = p_E - \tilde{p}_B &= \frac{RT}{\hat{v}_w} \ln\left(\frac{\tilde{x}_{wB}}{x_{wE}}\right) \approx \frac{RT}{\hat{v}_w} (x_{NaE} + x_{ClE} - \tilde{x}_{NaB} - \tilde{x}_{ClB}) \\ &= \frac{RT}{\hat{v}_w} (2x_{NaE} + y_{PG} - 2\sqrt{x_{NaE}(x_{NaE} + y_{PG})}) \end{aligned} \tag{A.4}$$

from which results $\tilde{p}_B = p_E - \tilde{\pi}_{osm}$.

In order to obtain the quantities necessary to formulate the finite element method the expression of $\tilde{\pi}_{osm}$ needs to be differentiated:

$$\begin{aligned} \delta\tilde{\pi}_{osm} &\approx \frac{RT}{\hat{v}_w} (\delta x_{NaE} + \delta x_{ClE} - 2\delta \tilde{x}_{NaB}) \\ = \frac{RT}{\hat{v}_w} \left(\delta x_{NaE} + \delta x_{ClE} - 2\delta\sqrt{x_{NaE} x_{ClE}}\right) &= \sum\nolimits_{k \epsilon E^{ions}} P_k \delta x_{kE} \,, \\ \text{with } P_{Na} = \frac{RT}{\hat{v}_w}\left(1 - \frac{x_{ClE}}{\sqrt{x_{NaE} x_{ClE}}}\right) &= \frac{RT}{\hat{v}_w}\left(1 - \frac{x_{ClE}}{\tilde{x}_{NaB}}\right), \\ \text{and } P_{Cl} = \frac{RT}{\hat{v}_w}\left(1 - \frac{x_{NaE}}{\sqrt{x_{NaE} x_{ClE}}}\right) &= \frac{RT}{\hat{v}_w}\left(1 - \frac{x_{NaE}}{\tilde{x}_{NaB}}\right). \end{aligned} \tag{A.5}$$

Then, using Eq.(B.11) in Appendix B, we get:

$$\delta\tilde{\pi}_{osm} = Q_u \text{div}\, \delta\boldsymbol{u} + \sum_{l\epsilon E^{mo}} Q_l \hat{m}_l \delta\mu_{lE}^{ec},$$

$$\text{with } Q_u = \sum_{k\epsilon E^{ions}} P_k \frac{3}{4}\frac{y_{PG}}{n^E}\frac{\xi_k x_{kE}}{z_E}, \quad Q_l = \sum_{k\epsilon E^{ions}} P_k \frac{x_{kE}}{RT} z_{kl}, \quad z_{kl} = I_{kl} - \xi_k\xi_l\, x_{lE}/z_E \text{ and } z_E = x_{NaE} + x_{ClE}. \tag{A.6}$$

As the system evolves towards the equilibrium, which occurs when the tissue is in balance with the (homogeneous) real bath (the fictitious bath then becomes the real bath), the electro-chemo-mechanical equilibrium conditions (Eq.(A.2), Eq.(A.3) and Eq.(A.4)) can also be used to obtain the equilibrium concentrations within the tissue and the osmotic pressure as a function of the known (real) bath composition $x_{NaB} = x_{ClB} = x^*$, as:

$$x_{NaE} = \frac{-y_{PG}}{2} + \frac{\sqrt{y_{PG}^2+4x^{*2}}}{2}, \quad x_{ClE} = \frac{y_{PG}}{2} + \frac{\sqrt{y_{PG}^2+4x^{*2}}}{2}, \quad x_{wE} = 1 - \sqrt{y_{PG}^2 + 4x^{*2}}, \quad \pi_{osm} = \frac{RT}{\hat{v}_w}\left(\sqrt{y_{PG}^2 + 4x^{*2}} - 2x^*\right). \tag{A.7}$$

By approximating the total volume of the EF phase by the volume of the EF water (water is the most abundant constituent of the EF phase of the tissue) and replacing the molar fractions by molar concentrations ($x_{kE} \approx c_{kE}\hat{v}_w$), an approximated equation for the osmotic pressure can be obtained:

$$\pi_{osm} = RT(\sqrt{e_{PG}^2 + 4c^{*2}} - 2c^*), \tag{A.8}$$

where $c^* = c_{NaB} = c_{ClB}$ is the ionic concentration of the bath.

Appendix B. Algebraic manipulations

In this Appendix some algebraic manipulations necessary to update the dependent variables and to obtain the element stiffness and diffusion matrices are provided. The constraints that must be obeyed by the molar fractions in the EF phase are:

$$\begin{cases} x_{wE} + x_{NaE} + x_{ClE} + x_{PG} = 1 \\ x_{NaE} - x_{ClE} + y_{PG} = 0, \end{cases} \tag{B.1}$$

where the PGs molar fraction x_{PG} is considered to be approximately zero. Nevertheless, the quantity $y_{PG} = \xi_{PG}\, x_{PG}$ can not be neglected, since, despite the fact that x_{PG} is a very small number, the PGs valence ξ_{PG} is a very large number and, thus, y_{PG} is a significant quantity.

The volume content of the EF phase v^E is given by $v^E = V_E/V_0$, and the variation of the volume content is $\delta v^E = \delta V_E/V_0$. The volume of the EF phase is given by $V_E = \Sigma_{k\epsilon E}\, V_{kE}$, which can be approximated by the volume of water in the EF phase V_{wE}, since water is the most abundant component in this phase. The same is true for the IF phase: $v^I = V_I/V_0 \approx V_{wI}/V_0$, and $\delta v^I = \delta V_I/V_0$. The solid phase is considered to be incompressible and thus variations of the total volume are only due to variations of the volume of the fluid phases due to exchanges of mass with the surrounding bath. In this way the following expression can be written:

$$\delta v^E + \delta v^I = \frac{\delta V_E}{V_0} + \frac{\delta V_I}{V_0} \approx \frac{\delta V_{wE}}{V_0} + \frac{\delta V_{wI}}{V_0} \tag{B.2}$$

$$= \frac{\delta V_w}{V_0} = \frac{\delta V}{V_0} = \delta\left(\frac{V}{V_0}\right) = \delta(\det \boldsymbol{F}) = \det \boldsymbol{F}\, \text{div}\, \boldsymbol{v}_S \delta t \approx \text{div}\, \delta \boldsymbol{u}$$

Moreover, as previously mentioned, it is also defined that the variation of the volume of water in the IF and EF phases are always equal to, respectively 25% and 75% of the total variation of the volume of water: $\delta V_{wI} = 0.25\ \delta V_w$ and $\delta V_{wE} = 0.75\ \delta V_w$. In this way, the variation of the EF volume content is:

$$\delta v^E = \frac{3}{4}\frac{\delta V_w}{V_0} = \frac{3}{4}\,\text{div}\,\delta \boldsymbol{u}. \tag{B.3}$$

The volume fraction of the EF phase is given by $n^E = V_E/V = (\Sigma_{k\epsilon E}\ V_{kE})/\text{V} \approx V_{wE}/V$, and the respective variation may be written as:

$$\delta n^E = \frac{\delta V_{wE}}{V} - \frac{V_{wE}}{V^2}\delta V = \frac{\delta V_{wE}}{V_0}\frac{V_0}{V} - n^E\frac{\delta V}{V_0}\frac{V_0}{V} \approx \frac{\delta V_E}{V_0} - n^E\left(\frac{\delta V_E}{V_0} + \frac{\delta V_I}{V_0}\right) = \left(\frac{3}{4} - n^E\right)\text{div}\,\delta \boldsymbol{u}. \tag{B.4}$$

The variation of the PG effective molar fraction y_{PG} can be obtained considering that $y_{PG} = \xi_{PG}\, x_{PG} \approx \xi_{PG}\, N_{PG}/n^E\ \hat{v}_w/V$,

$$\delta y_{PG} = \xi_{PG}\delta x_{PG} \approx -\xi_{PG}\frac{N_{PG}}{(n^E)^2}\frac{\hat{v}_w}{V}\delta n^E - \xi_{PG}\frac{N_{PG}}{n^E}\frac{\hat{v}_w}{V^2}\delta V \approx -y_{PG}\left(\frac{\delta n^E}{n^E} + \frac{\delta V}{V}\right) \approx -\frac{3}{4}\frac{y_{PG}}{n^E}\text{div}\,\delta \boldsymbol{u}. \tag{B.5}$$

The molar fractions of the species can be defined as a function of the volume contents v^{kE}:

$$x_{kE} \approx \frac{N_{kE}}{n^E}\frac{\hat{v}_w}{V} = \frac{V_{kE}}{\hat{v}_k n^E}\frac{\hat{v}_w}{V} = \frac{\hat{v}_w}{\hat{v}_k}\frac{v^{kE}}{n^E}\frac{V_0}{V} \tag{B.6}$$

and therefore, since $m^{kE} = \rho_k\, v^{kE}$,

$$\frac{\delta m^{kE}}{m^{kE}} = \rho_k\frac{\delta v^{kE}}{m^{kE}} = \frac{\delta v^{kE}}{v^{kE}} \approx \frac{\delta x_{kE}}{x_{kE}} + \frac{3}{4n^E}\text{div}\,\delta \boldsymbol{u}, \quad k \in E^{mo}. \tag{B.7}$$

Using the definition of the electro-chemical potentials $\mu_{kE}^{ec} = g_{kE}^{ec}/\,\hat{m}_k$ and the constraints imposed to the molar fractions Eq.(B.1), the variation of the EF electrical potential can be obtained:

$$y_{PG}F\delta\phi^E = x_{wE}\hat{v}_w\delta p_E - \sum\nolimits_{l\epsilon E^{mo}} x_{lE}\hat{m}_l\delta\mu_{lE}^{ec}. \tag{B.8}$$

The variation of the molar fractions of the ionic species may be also computed substituting Eq.(B.8) in the variation of the corresponding electro-chemical potentials as

$$\begin{aligned}\delta x_{kE} &= \frac{\hat{m}_k}{RT}x_{kE}\left(\delta\mu_{kE}^{ec} - \frac{\xi_k x_{wE}\hat{v}_w}{\hat{m}_k y_{PG}}\delta p_E + \frac{\xi_k}{\hat{m}_k y_{PG}}\sum\nolimits_{l\epsilon E^{mo}} x_{lE}\hat{m}_l\delta\mu_{lE}^{ec}\right)\\ &= -\frac{\xi_k}{RT}\frac{x_{kE}}{y_{PG}}x_{wE}\hat{v}_w\delta p_E + \frac{x_{kE}}{RT}\left(\hat{m}_k\delta\mu_{kE}^{ec} + \frac{\xi_k}{y_{PG}}\sum\nolimits_{l\epsilon E^{mo}} x_{lE}\hat{m}_l\delta\mu_{lE}^{ec}\right), \qquad k \in E^{ions}.\end{aligned} \tag{B.9}$$

Resorting once again to the electroneutrality condition $(\Sigma_{k\epsilon E^{mo}}\ \xi_k\ \delta x_{kE}) + \delta y_{PG} = 0$, and using Eq.(B.5) and Eq.(B.9), the EF pressure may be defined as a function of the primary variables:

$$z_E x_{wE} \hat{v}_w \delta p_E = -\frac{3y_{PG}^2}{4n^E} RT \operatorname{div} \delta \boldsymbol{u} + z_E \sum\nolimits_{l \epsilon E^{mo}} z_{lE} x_{lE} \hat{m}_l \delta \mu_{lE}^{ec} \,, \tag{B.10}$$

where $z_E = x_{NaE} + x_{ClE}$ and $z_{lE} = 1 + \xi_l y_{PG}/z_E$.

Further manipulations may be performed in order to obtain the variations of the molar fractions of the ionic species as a function of the primary unknowns:

$$\delta x_{kE} = \frac{3y_{PG}\xi_k x_{kE}}{4n^E z_E} \operatorname{div} \delta \boldsymbol{u} + \frac{x_{kE}}{RT} \sum\nolimits_{l \epsilon E^{ions}} z_{klE} \hat{m}_l \delta \mu_{lE}^{ec} \,, \quad k \in E^{ions}, \tag{B.11}$$

where $z_{klE} = I_{kl} - \xi_k \, \xi_l \, x_{lE} \, z_E$ and $\boldsymbol{I}$, with components I_{kl}, is the identity matrix. The incremental fictitious osmotic pressure may also be defined, replacing Eq.(B.11) in Eq.(A.5).

Using Eq.(B.7) and Eq.(B.11), the mass content variations may also be defined as a function of the variations of the primary variables:

$$\delta m^{kE} = \frac{3}{4} \frac{m^{kE}}{n^E} z_{kE} \operatorname{div} \delta \boldsymbol{u} + \frac{m^{kE}}{RT} \sum\nolimits_{l \epsilon E^{ions}} z_{klE} \hat{m}_l \delta \mu_{lE}^{ec} \,, \quad k \in E^{ions}, \tag{B.12}$$

from which the derivative of the volume contents of the ionic species in order of time, $\mathrm{d}v^{kE}/\mathrm{d}t$, used in Eq.(34), may be obtained:

$$\frac{\mathrm{d}v^{kE}}{\mathrm{d}t} = \frac{v^{kE}}{m^{kE}} \frac{\mathrm{d}m^{kE}}{\mathrm{d}t} = \frac{3}{4} \frac{v^{kE} z_{kE}}{n^E} \operatorname{div}\left(\frac{\mathrm{d}\boldsymbol{u}}{\mathrm{d}t}\right) + \frac{v^{kE}}{RT} \sum\nolimits_{l \epsilon E^{ions}} z_{klE} \hat{m}_l \left(\frac{\mathrm{d}\mu_{lE}^{ec}}{\mathrm{d}t}\right), k \in E^{ions}. \tag{B.13}$$

The stress increment can also be computed, using the mechanical constitutive equation Eq.(21), as well as Eq.(B.10) and Eq.(A.6):

$$\delta \boldsymbol{\sigma} = -\delta p_E \boldsymbol{I} - \alpha_p \, \delta \tilde{\pi}_{osm} \boldsymbol{I} + (1 + \alpha_w \, \tilde{\pi}_{osm}) \mathbf{E} \colon \delta \boldsymbol{E} + \alpha_w \, \delta \tilde{\pi}_{osm} \mathbf{E} \colon \boldsymbol{E}. \tag{B.14}$$

Defining

$$\begin{gathered} \delta p_E = -R_u \operatorname{div} \delta \boldsymbol{u} - \sum\nolimits_{l \epsilon E^{mo}} R_l \hat{m}_l \delta \mu_{lE}^{ec} \\ \text{with } R_u = \frac{3RTy_{PG}^2}{4n^E z_E x_{wE} \hat{v}_w}, \\ \text{and } R_l = -\frac{z_{lE} x_{lE}}{x_{wE} \hat{v}_w}, \end{gathered} \tag{B.15}$$

Eq.(B.14) gets the form

$$\begin{aligned} \delta \boldsymbol{\sigma} = & \left[(1 + \alpha_w \tilde{\pi}_{osm}) \mathbf{E} + \left[\left(R_u - \alpha_p Q_u\right) \boldsymbol{I} + \alpha_w Q_u \mathbf{E} \colon \boldsymbol{E}\right] \otimes \boldsymbol{I}\right] \operatorname{div} \delta \boldsymbol{u} \\ & + \sum\nolimits_{l \epsilon E^{mo}} \left[\left(R_l - \alpha_p Q_l\right) \boldsymbol{I} + \alpha_w Q_l \mathbf{E} \colon \boldsymbol{E}\right] \hat{m}_l \delta \mu_{lE}^{ec}. \end{aligned} \tag{B.16}$$

In the case of a uniaxial deformation ε, Eq.(B.16) becomes:

$$\begin{aligned} \delta \sigma = & \left[(1 + \alpha_w \tilde{\pi}_{osm}) E_{sat} + \left[\left(R_u - \alpha_p Q_u\right) + \alpha_w Q_u E_{sat} \varepsilon\right]\right] \frac{\mathrm{d}(\delta u)}{\mathrm{d}x} \\ & + \sum\nolimits_{l \epsilon E^{mo}} \left[\left(R_l - \alpha_p Q_l\right) + \alpha_w Q_l E_{sat} \varepsilon\right] \hat{m}_l \delta \mu_{lE}^{ec}. \end{aligned} \tag{B.17}$$

References

[1] Barbe M, Driban JB, Safadi FF, Barr AE, Popoff SN. Structure and Function of Joints. In Bone Pathology 2009 (pp. 51-60). Humana Press.

[2] Martin RB, Burr DB, Sharkey NA, Fyhrie DP. Synovial Joint Mechanics. In Skeletal Tissue Mechanics 2015 (pp. 227-273). Springer.

[3] Hung CT, Mow VC. Biomechanics of Articular Cartilage. In Basic Biomechanics of the Musculoskeletal System 2001 (pp. 60-101). Lippincott Williams and Wilkins.

[4] Sophia Fox AJ, Bedi A, Rodeo SA. The basic science of articular cartilage: Structure, composition, and function. Sports Health. 2009;1(6):461–468.

[5] Greene GW, Zappone B, Söderman O, Topgaard D, Rata G, Zeng H, Israelachvili JN. Anisotropic dynamic changes in the pore network structure, fluid diffusion and fluid flow in articular cartilage under compression. Biomaterials. 2010;31(12):3117–3128.

[6] Eisenberg SR, Grodzinsky AJ. Swelling of articular cartilage and other connective tissues: Electromechanochemical forces. Journal of Orthopaedic Research. 1985;3(2):148–159.

[7] Han E, Chen SS, Klisch SM, Sah RL. Contribution of proteoglycan osmotic swelling pressure to the compressive properties of articular cartilage. Biophysical Journal. 2011;101(4):916–924.

[8] Maroudas A, Wachtel E, Grushko G, Katz E, Weinberg P. The e_ect of osmotic and mechanical pressures on water partitioning in articular cartilage. Biochimica et Biophysica Acta. 1991;1073(2):285–294.

[9] Egri D, Battistella LR, Yoshinari NH. O envelhecimento da cartilagem articular. Revista Brasileira de Reumatologia. 1999;39(1):45–48.

[10] Guilak F. Biomechanical factors in osteoarthritis. Best Practice and Research Clinical Rheumatology. 2011;25(6):815–823.

[11] Mow VC, Kuei SC, Lai WM, Armstrong CG. Biphasic creep and stress relaxation of articular cartilage in compression: Theory and experiments. Journal of Biomechanical Engineering. 1980;102(1):73–84.

[12] Lai WM, Hou JS, Mow VC. A triphasic theory for the swelling and deformation behaviors of articular cartilage. Journal of Biomechanical Engineering. 1991;113(3):245–258.

[13] Gu WY, Lai WM, Mow VC. A mixture theory for charged-hydrated soft tissues containing multi-electrolytes: passive transport and swelling behaviors. Journal of Biomechanical Engineering. 1998;120:169–180.

[14] Huyghe J. Intra-extrafibrillar mixture formulation of soft charged hydrated tissues. Journal of Theoretical and Applied Mechanics. 1999;37(3):519–536.

[15] Loret B, Simões FMF. Articular cartilage with intra- and extrafibrillar waters: A chemo-mechanical model. Mechanics of Materials. 2004;36(5-6):515–541.

[16] Loret B, Simões FMF. Mechanical effects of ionic replacements in articular cartilage. Part I: The constitutive model. Biomechanics and Modeling in Mechanobiology. 2005;4(2-3):63–80.

[17] Loret B, Simões FMF. Mechanical effects of ionic replacements in articular cartilage. Part II: Simulations of successive substitutions of NaCl and CaCl2. Biomechanics and Modeling in Mechanobiology. 2005;4(2-3):81–99.

[18] Loret B, Simões FMF. Articular cartilage with intra- and extrafibrillar waters - mass transfer and generalized diffusion. European Journal of Mechanics, A/Solids. 2007;26(5):759–788.

[19] Loix F, Simões FMF, Loret B. Articular cartilage with intra and extrafibrillar waters - Simulations of mechanical and chemical loadings by the finite element method. Computer Methods in Applied Mechanics and Engineering. 2008;197(51-52):4840–4857.

[20] Loret B, Simões FMF. Effects of the pH on the mechanical behavior of articular cartilage and corneal stroma. International Journal of Solids and Structures. 2010;47(17):2201–2214.

[21] Basser PJ, Schneiderman R, Bank RA, Wachtel E, Maroudas A. Mechanical properties of the collagen network in human articular cartilage as measured by osmotic stress technique. Archives of Biochemistry and Biophysics, 351(2):207–219, 1998.

[22] Loret B, Simões FMF. Biomechanical Aspects of Soft Tissues. Boca Raton: CRC Press; 2017.

[23] Loret B, Simões FMF. A framework for deformation, generalized diffusion, mass transfer and growth in multi-species multi-phase biological tissues. European Journal of Mechanics, A/Solids. 2005;24(5):757–781.

Journal of Computation and Artificial Intelligence in Mechanics and Biomechanics ISSN 2184-8971
Volume 2, Issue 1, Page 17-34, 2022

Finite element simulations of the electro-chemo-mechanical behavior of articular cartilage. Part II: results and discussion

Mariana Bento[1], Fernando M.F. Simões[2], Benjamin Loret[3]

[1] *Instituto Superior Técnico, University of Lisbon, mariana.bento@tecnico.ulisboa.pt; Av. Rovisco Pais,1;Lisboa;Portugal*
[2] *CERIS and Instituto Superior Técnico, University of Lisbon, fernando.simoes@tecnico.ulisboa.pt; Av. Rovisco Pais,1;Lisboa;Portugal*
[3] *Laboratoire 3SR, Université Grenoble Alpes, Benjamin.Loret100@gmail.com; Domaine universitaire BP53, 38041 Grenoble Cedex 9; France*

Abstract
In the present work, the finite element formulation and program presented in part I of this paper, are used to numerically simulate the response of an articular cartilage sample to a combination of chemical and mechanical actions. In the simulations, a sample of articular cartilage, laterally confined, is immersed in a bath of variable chemical composition always assuming the existence of electro-chemical equilibrium at the tissue-bath interface. Nonetheless, inside the tissue, the equilibrium is not attained instantaneously. In fact, the time needed to establish a steady state depends on the problem geometry and on some material properties, namely the percolation and diffusion times associated with Darcy's and Fick's laws, respectively. A good agreement is obtained between the results of the present model and previous experimental data in the case of a homogeneous bath. As another new feature of the model, results are also obtained when the tissue is immersed in a bath which allows each of the sample extremities to experience distinct variations of the chemical composition, which gives a closer insight to the tissue's behavior under a more diverse environment.

***DOI**: 10.5281/zenodo.7406031*

Article Info

Keywords
Articular cartilage
Osteoarthritis
Electro-chemo-mechanical couplings
Finite element method

Article History
Received: *19/05/2022*
Revised: *06/07/2022*
Accepted: *01/11/2022*

1. Introduction

In this work, a finite element program, whose formulation is based on the model described in part I of this paper, is used to numerically simulate the response of an articular cartilage sample to a combination of chemical and mechanical actions. The finite element formulation follows the framework of the model by Loix *et al*. [1] accounting for the presence of one solid phase and two water compartments (extrafibrillar – EF and intrafibrillar – IF phases). However, as new features of the present formulation: 1) it uses the electro-chemo-mechanical constitutive law defined in [2] and 2) the contribution of the IF phase is considered in a simplified way, not requiring the definition of IF material parameters and functions.

In the simulations, a sample of articular cartilage, laterally confined, is immersed in a bath of variable chemical composition always assuming the existence of electro-chemical equilibrium at the tissue-bath interface. The corresponding chemo-mechanical parameters are obtained from the experimental tests by Eisenberg and Grodzinsky [3] and a good agreement is obtained between the simulated and experimental results. In particular, the shielding effect observed in the experimental results is very well reproduced by the model, which is something that other existing articular cartilage chemo-mechanical models (*e.g.* [4]) and existing finite element software packages based on those models (like FEBio [5]) are not able to replicate since they assume a constant stiffness for the tissue.

As another new feature of the present formulation, 3) numerical results are also obtained when the tissue is immersed in a bath which allows each of the sample extremities to experience distinct variations of the chemical composition. This simulation gives a closer insight to the tissue's behavior under a more diverse environment which is something that other existing models are also not able to provide.

2. Parameter identification

The definition of proper values for the material parameters is conducted by adjusting the mechanical model to actual experimental results obtained by Eisenberg and Grodzinsky [3]. In that work, an extraction of a cylindrical graft of bovine

Corresponding Author
Fernando M.F. Simões
fernando.simoes@tecnico.ulisboa.pt

articular cartilage and bone was performed, followed by several cuts, obtaining a final sample of cartilage from the middle zone with 6.4 mm of diameter and 600 μm of thickness. Posterior confined compression tests were conducted.

Table 1 - Chemical constants.

Species, k	Molar volume, $\hat{v}_k$ (m^3 mol^{-1})	Molar mass, $\hat{m}_k$ (kg mol^{-1})	Valence ξ_k
w	18×10^{-6}	0.018	0
Na	2.37×10^{-6}	0.023	+1
Cl	15.42×10^{-6}	0.0355	–1
PG	-	2000	–4500 [2]

The initial volume of the tissue sample described above is $V_0 = 0.0193\times10^{-6}$ m^3. Supposing that, initially, 80% of the total volume of the articular tissue is water, the initial total volume of water in the sample may be obtained: $V_w^0 = 0.8\ V_0$. However, as mentioned in section 1 of the companion paper, part of the water is contained in the IF space and the remaining in the EF space, being the percentage of water, with respect to the total amount, in the IF and EF phases, 25% and 75%, respectively. In this way, the initial EF water volume is $V_{wE}^0 = 1.1580\times10^{-8}$ m^3 and the respective number of moles, considering the water density and the water molar mass (Table 1), is $N_{wE}^0 = 6.4333\times10^{-4}$ mol. Regarding the PGs, their mass percentage from the total tissue's mass is considered to be 5%, thus resulting in a number of moles $N_{PG} = 5.3075\times10^{-10}$ mol and in a volume $V_{PG} = 5.8913\times10^{-10}$ m^3, considering the PGs' molar mass shown in Table 1 and a tissue density equal to 1.1 g/cm^3. Since PG molecules are not able to leave the EF space, PGs' mass remains constant.

The bath concentration is initially set to 1000 mol/m^3 = 1 M (practically near to saturation), with its pressure and electrical potential being set to zero (reference values). In a situation of equilibrium between the bath and the tissue, the electro-chemical potentials of the water and ions inside and outside the tissue are equal. In this way, the initial number of moles of the ionic species in the EF phase is $N_{NaE}^0 = 1.28381\times10^{-5}$ mol and $N_{ClE}^0 = 1.04497\times10^{-5}$ mol, from which the initial molar fraction of the PGs is obtained: $x_{PG}^0 = N_{PG}/(N_{wE}^0 + N_{NaE}^0 + N_{ClE}^0 + N_{PG}) = 7.9618\times10^{-7}$. Moreover, considering that the initial total volume of the EF phase is given by the contributions of the initial volume of all its constituents (water, ions and PGs), its value is $V_E^0 = 1.2361\times10^{-8}$ m^3. Taking into account the valence of the PG molecule (see Table 1), the initial value of the FCD is obtained: $e_{PG}^0 = \xi_{PG}\ c_{PG}^0 = -193$ moles of charge/(m^3 of extrafibrillar water), or, equivalently, $e_{PG}^0 = -0.1125$ mEq of charge/(g of wet tissue), which is within the values of the FCD reported by Maroudas [6].

In a state of equilibrium between the tissue and the surrounding medium, the fictitious bath coincides to the real bath, and thus $\tilde{\pi}_{osm} = \pi_{osm}$ and $\tilde{p}_B = p_B$. Taking additionally the pressure of the real bath as a reference value (formally taking $p_B = 0$), we obtain: $p_E = \pi_{osm}$, and the constitutive equation Eq.(21) in the companion paper, under a uniaxial strain state, becomes:

$$\sigma = -p_E\left(1 + \alpha_p\right) + (1 + \alpha_w p_E)E_{sat}\varepsilon \tag{1}$$

where the constitutive tensor $\mathbf{E}$ is represented, in a one-dimensional strain state, only by the material parameter E_{sat} and p_E is given by Eq.(A.8) in the companion paper:

$$p_E = RT\left(\sqrt{e_{PG}^2 + 4c^*} - 2c^*\right) \tag{2}$$

where $e_{PG} = \xi_{PG}\ c_{PG}$ is the tissue FCD and $c^* = c_{NaB} = c_{ClB}$ is the ionic concentration of the bath. In this way, three mechanical parameters have to be defined: α_p, α_w and E_{sat}, the latter being the confined compression modulus at the tissue's saturation state.

The adjustment of the model to the experimental points is performed in two different stages, considering in all cases that the system is under equilibrium:

1. The first stage is performed under a no deformation condition, in which the bath composition is changed, decreasing the concentration from the initial value (chosen to be 1000 mol/m^3) to a given final target concentration;
2. During the second stage, a negative deformation is imposed under a fixed concentration of salt in the bath.

Temperature is considered to be equal to 298 K and pH is considered to be neutral.

Assuming that the collagen fibers (solid phase) and the PG molecules are incompressible, as the contractive uniaxial deformation ($\varepsilon < 0$) is applied, the volume of the EF phase and the FCD value are gradually updated as:

$$V_E = V_E^0 + \varepsilon V_0, \tag{3}$$

and

$$e_{PG} = \xi_{PG} N_{PG} / V_E. \tag{4}$$

After updating e_{PG} using Eq.(4), the water pressure and the corresponding stress are obtained from Eq.(2) and Eq. (1), respectively.

During stage 1, the variation of the salt concentration in the bath, considering a zero deformation, allows to obtain the first mechanical parameter in the mechanical model, α_p, since, during this stage, the stress is only governed by $\sigma = -p_E(1 + \alpha_p)$. Thus, from the initial hypertonic state, the bath concentration is decreased until the target concentration is reached. During this decrease of the bath concentration, a successive increase in the absolute value of the stress, due to the increase of the water pressure, is observed. This trend results from the flow of water towards the inside of the tissue. The lower the final concentration is, the higher is the water pressure, and consequently, the higher is the compressive stress. The value of α_p that most accurately approximates the model to the experimental results is $\alpha_p = -0.95$.

During stage 2, under a constant bath concentration c^*, a negative deformation is applied. With the α_p parameter already defined, the remaining mechanical parameters, α_w and E_{sat}, that determine, for each salt concentration in the bath, the slope of the corresponding stress-strain curve, are obtained. When the salt concentration in the bath is very large, there is a tendency of ionic species to move towards the inside of the tissue, increasing the shielding effect and decreasing the repulsive forces and the compressive stiffness of the tissue. Thus, for the same strain but different bath concentration, a higher compressive stress is observed when the outer concentration is lower, since the repulsive forces are less shielded and the compressive stiffness of the tissue is higher. Moreover, as the contractive strain increases, while maintaining the same chemical conditions, the proteoglycans get closer to each other, increasing the inter repulsive forces. All these aspects are well reproduced by the model, as it may be seen in Fig.1. The curves obtained in Fig.1 are adjusted in order to fit the experimental data [3] and the values of α_w and E_{sat} that minimize the error for all the curves are 5.4×10^{-6} Pa^{-1} and 250 kPa, respectively.

In order to complete the material constants of the model, the values used for the transport parameters required for the computation of the generalized diffusion matrix components to be used in the finite element simulations, which are retrieved from [1], are presented in Table 2.

Table 2 - Transport parameters.

Hydraulic conductivity K_h	Sodium diffusion coefficient D_{NaE}	Chloride diffusion coefficient D_{ClE}	Tortuosity τ
9.8×10^{-12} m/s	13.3×10^{-10} m^2/s	20.3×10^{-10} m^2/s	0.4

3. Finite element simulations

3.1. Initial state and simulation framework

The sample of cartilage considered in section 2 is also considered in the finite element simulations performed in this section. The bath concentration is again initially set to 1000 mol/m^3 = 1 M, with its pressure and electrical potential being set to zero (reference values). The tissue sample is also considered to be initially at zero deformation (see Fig.2). Imposing electro-chemical equilibrium between the initial bath and the tissue, all the initial quantities are obtained and their values are summarized in Table 3.

Table 3 - Initial values

$V_0 = 0.0193\times10^{-6}$ m^3	$V_w^0 = 1.544\times10^{-8}$ m^3	$p_E^0 = 2.6413\times10^4$ Pa	$\phi_w^0 = -2.64283\times10^{-3}$ V
$V_{PG} = 5.8913\times10^{-10}$ m^3	$V_{wE}^0 = 1.1580\times10^{-8}$ m^3	$V_{NaE}^0 = 3.0426\times10^{-11}$ m^3	$V_{ClE}^0 = 1.6113\times10^{-10}$ m^3
$N_{PG} = 5.3075\times10^{-10}$ mol	$N_{wE}^0 = 6.4333\times10^{-4}$ mol	$N_{NaE}^0 = 1.28381\times10^{-5}$ mol	$N_{ClE}^0 = 1.04497\times10^{-5}$ mol
$x_{PG}^0 = 7.9618\times10^{-7}$	$x_{wE}^0 = 0.9651$	$x_{NaE}^0 = 0.0193$	$x_{ClE}^0 = 0.0157$

From this initial state, alterations are imposed either through changes in the bath concentration (chemical loading) or through the imposition of uniaxial (confined) deformation in the tissue (mechanical loading). During chemical loading, rates of change of the electro-chemical potentials are imposed at the nodes of the extremities of the tissue sample corresponding to constant rate of change of the number of moles of salt in the bath. During mechanical loading, constant rates of displacement are imposed at the nodes of the extremities of the tissue sample.

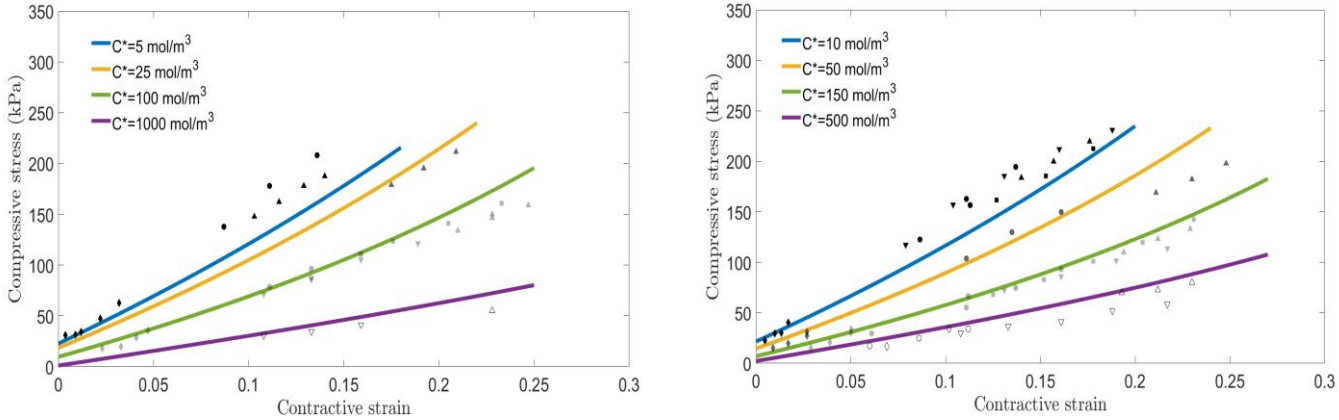

Fig.1 - Experimental points (symbols) by Eisenberg and Grodzinsky [3] and stress-strain curves obtained by the mechanical constitutive model proposed, while changing the contractive deformation, from zero to a given final strain value, under different bath concentrations c^* from 5 to 1000 mol/m^3, with $\alpha_p = -0.95$, $\alpha_w = 5.4\times10^{-6}$ Pa^{-1} and $E_{sat} = 250$ kPa in Eq.(1).

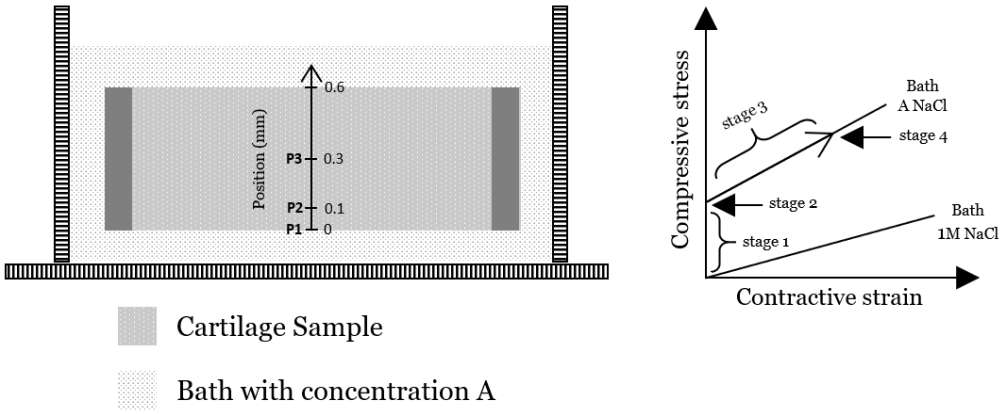

Fig.2 - A cylindrical tissue sample, with 0.6 mm thickness, is immersed in a bath which is initially homogeneous in both its mechanical properties and chemical composition (concentration A). The specimen is in contact with the bath along the upper and lower surfaces.

The main simulations performed in this work involve four distinct stages, with changes in both the chemical composition of the bath and in the deformation of the tissue (see Fig.2):

1. Stage 1: in the first stage, the bath concentration is decreased from the initial value (1 M NaCl) to a given final target concentration, under zero deformation, in a given time interval t_1;
2. Stage 2: during a time interval t_2, the system is left at rest, so that a new state of equilibrium is reached;
3. Stage 3: in the third stage, under a constant bath solution, a contractive uniaxial strain is imposed in a time interval t_3;
4. Stage 4: during a time interval t_4, the system is again left at rest in order for a new equilibrium to be reached.

The four-stage simulation described above is in part similar to the one conducted in section 2, to obtain the values of the material parameters of the mechanical model. However, in those simulations, long term equilibrium was assumed in all points while, in this simulation, the time variable is included, which allows to study the evolution in time and space of several variables defined within the sample under the combined action of chemical and mechanical "loads", with the equilibrium state being reached during the simulation in the two extra stages 2 and 4.

For the study of the influence of mesh size and time step on the convergence of the method, simulations are conducted with meshes comprising different number of finite elements and different time steps. The corresponding results are described in detail in Appendix A. From these results, it is concluded that the number of elements and the time step that allow a satisfactory convergence of the results, without increasing excessively the computational effort, are respectively equal to 50 elements and 0.1 s.

3.2. Homogeneous bath simulation

In this section, a simulation is conducted (see Fig.2) where, during the first stage, the homogeneous bath concentration is decreased at a constant rate from the initial value of 1000 mol/m^3 to a value of 150 mol/m^3 during 1000 s, under no variation of thickness, followed by a 50 minutes equilibrium stage. In the third stage, a negative 20% deformation is applied during 1000 s, followed by another 50 minutes equilibrium stage.

As the bath concentration decreases during stage 1, an outflow of ions is observed. Therefore, there is a consequent decrease of the sodium and chloride mass contents, m^{NaE} and m^{ClE}, throughout the tissue thickness, as pictured in Fig.3. Nevertheless, it may be seen that such decrease does not occur in a uniform manner over the thickness of the sample, with the impact of the decrease of the bath concentration being first felt in the extremities of the tissue (in contact with the bath), with the posterior progression towards inside the sample.

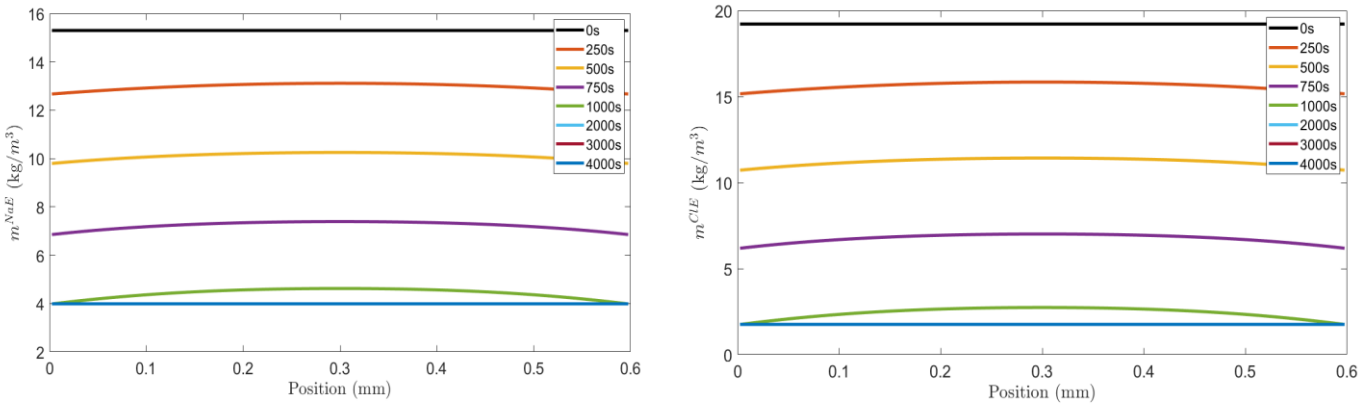

Fig.3 - Time evolution of the spatial distribution, along the tissue thickness, of the sodium (a) and chloride (b) ionic mass contents, m^{NaE} and m^{ClE}, during stages 1 and 2. The ionic content decreases due to a decrease of the ionic concentration of the bath. The last three curves are practically superimposed which means that steady state is practically reached at t = 2000 s. The same type of behavior can be observed next in Fig.4 to Fig.6.

Since the total volume during the first two stages of the simulation is the same as the initial one, and recalling that the solid phase is incompressible, the volume of the EF fluid phase must also remain constant. In this way, with the loss of ions in the EF phase, the water mass content, m^{wE}, increases at the end of the second stage, with its profile along the tissue thickness following the trend of the tissue local deformation (see Fig.4). Since in the first 4000 s of the simulation no total deformation is imposed, it may be seen in Fig.4(b) that, at any time, the overall mean strain is zero. However, the local deformation along the thickness of the tissue is not null before steady state is reached. In fact, as the salt concentration decreases in the bath, water enters the specimen from the top and bottom boundaries which consequently expand, while the constraint imposed in the total deformation implies the inverse trend in the middle of the specimen. Overall, integrating the local deformation, the total thickness of the tissue remains constant at any time (see Fig.11).

Fig.5 shows the evolution of the effective PG molar fraction y_{PG}, which is related to the FCD, e_{PG}, by $y_{PG} \approx \xi_{PG}\, c_{PG}\, \hat{v}_w = e_{PG}\, \hat{v}_w$. The values of y_{PG} vary between $-3.5/-3.6\times10^{-3}$, which corresponds to a FCD value $e_{PG} \approx -190$ moles of charge/m^3, within the range of values of FCD referred by Maroudas [6].

The EF water pressure, p_E, presents an increase at the end of stage 2 (see Fig.6(a)), being this a consequence of the increase of the water mass content in the EF phase without variation of the volume of the tissue.

The EF electrical potential, ϕ_E, is initially practically zero and by the end of the second stage, with the migration of ions towards outside the tissue, it becomes more negative (see Fig.6(b)). In fact, during the refreshment of the bath, the ionic concentrations decrease, both in the bath and in the cartilage, but the change is lower in the cartilage and this implies a decrease of the EF electrical potential.

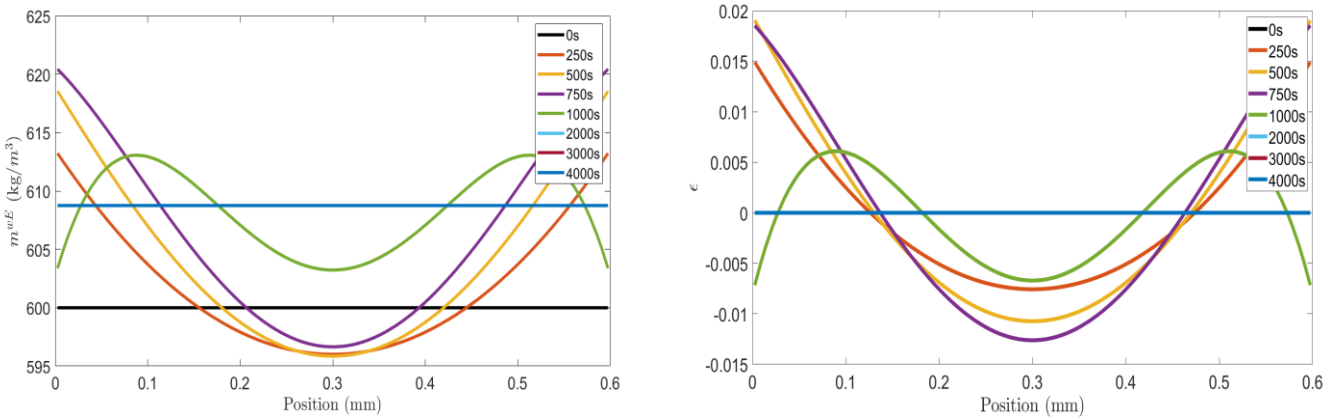

Fig.4 - Time evolution of the spatial distribution, along the tissue thickness, of the water mass content m^{wE} (a) and of the local tissue deformation ε (b), during stages 1 and 2. At time t = 0 s, the deformation is homogeneously equal to zero. The last three curves are practically superimposed which means that steady state, with zero deformation, is also practically reached at t = 2000 s. Before steady state is reached, the deformation is positive (extension) in the vicinity of the boundaries and negative (contraction) in the center of the specimen; the total thickness of the tissue remains constant at any time, though.

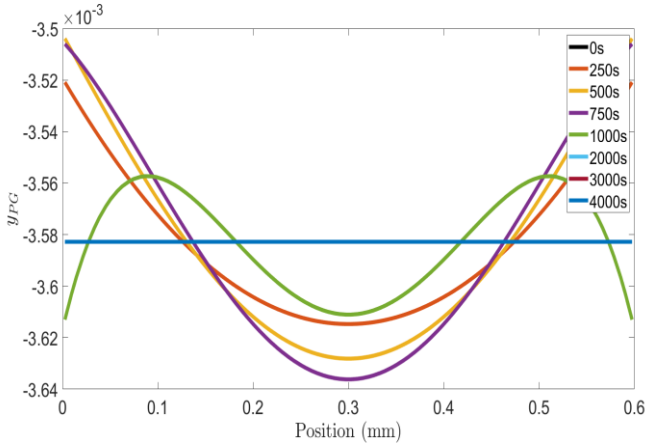

Fig.5 - Time evolution of the spatial distribution, along the tissue thickness, of the proteoglycan effective molar fraction y_{PG}, during stages 1 and 2. The first and the last three curves are practically superimposed, that is, the steady state proteoglycan effective molar fraction is practically equal to the initial value because the initial and steady state water mass contents are very close since the total deformation of the tissue is zero.

In stages 3 and 4, no alterations are imposed in the chemical composition of the bath surrounding the tissue. Thus, changes perceived in the chemical variables are a consequence of the applied deformation. In Fig.7, lower ionic mass contents are observed at the end of the simulation, although such decrease is not as significant as during the first two stages. When applying the contractive deformation, water and dissolved ions are expelled from the tissue. Thus, a decrease in the water mass content is also observed in Fig.8(a), with the consequent decrease of the tissue volume. Once again, the trend of the water mass content curves follows the trend of the deformation profiles (Fig.8(b)). At first, since the imposition of the displacement occurs at the extremities of the tissue, these are the points that experience a larger deformation. As the system evolves towards a new equilibrium, the deformation progresses to the inner points, until a homogeneous deformation is verified along the tissue thickness (see Fig.8(b)).

In contrast to what is verified during the change of the bath chemistry, after the application of the deformation an increase in the negative value of y_{PG} at the end of stage 4 is observed. Due to the decrease in the EF water volume, the PGs concentration is higher and so y_{PG} and the FCD have higher absolute values (see Fig.9).

When the negative deformation is applied, a higher EF water pressure p_E is observed. Moreover, with the exit of more ions, the EF electrical potential decreases once again, as one may verify in Fig.10.

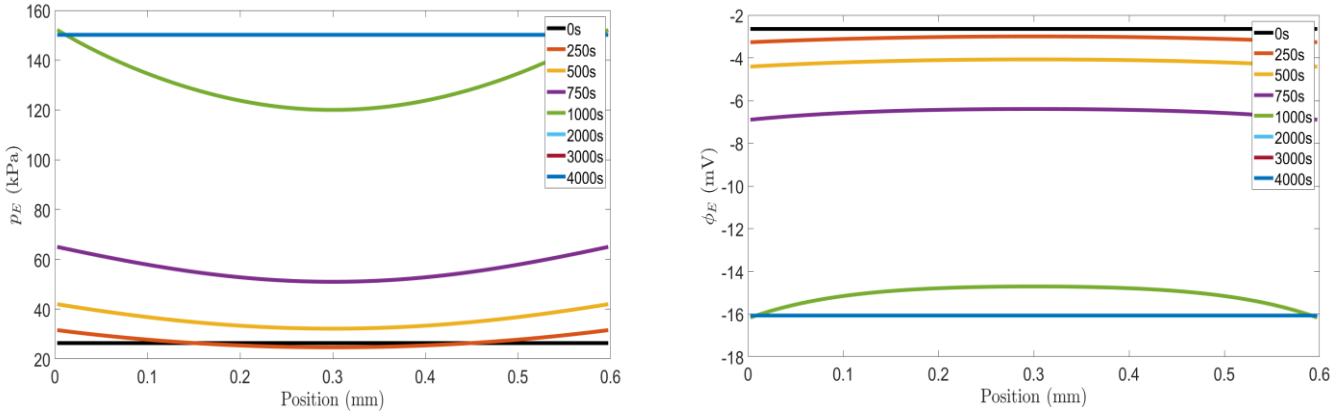

(a) (b)

Fig.6 - Time evolution of the spatial distribution, along the tissue thickness, of the EF water pressure p_E (a) and of the EF electrical potential ϕ_E (b), during stages 1 and 2. The increase of water pressure starts at the boundaries through which water infiltrates.

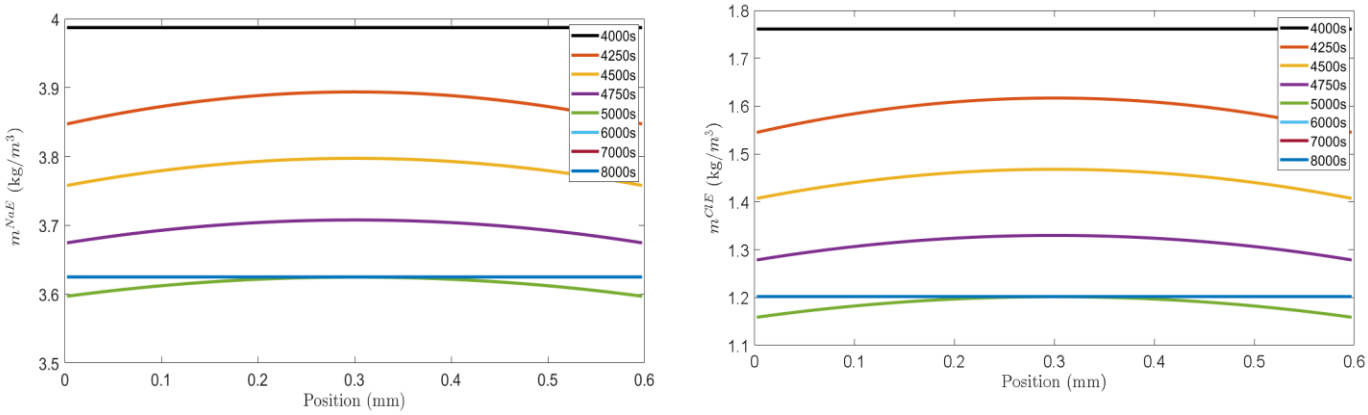

(a) (b)

Fig.7 - Time evolution of the spatial distribution, along the tissue thickness, of the sodium (a) and chloride (b) ionic mass contents, m^{NaE} and m^{ClE}, during stages 3 and 4. The ionic content decreases due to the imposed contractive deformation. The last three curves are practically superimposed which means that steady state is practically reached at t = 6000 s. The same type of behavior can be observed next in Fig.8 to Fig.10.

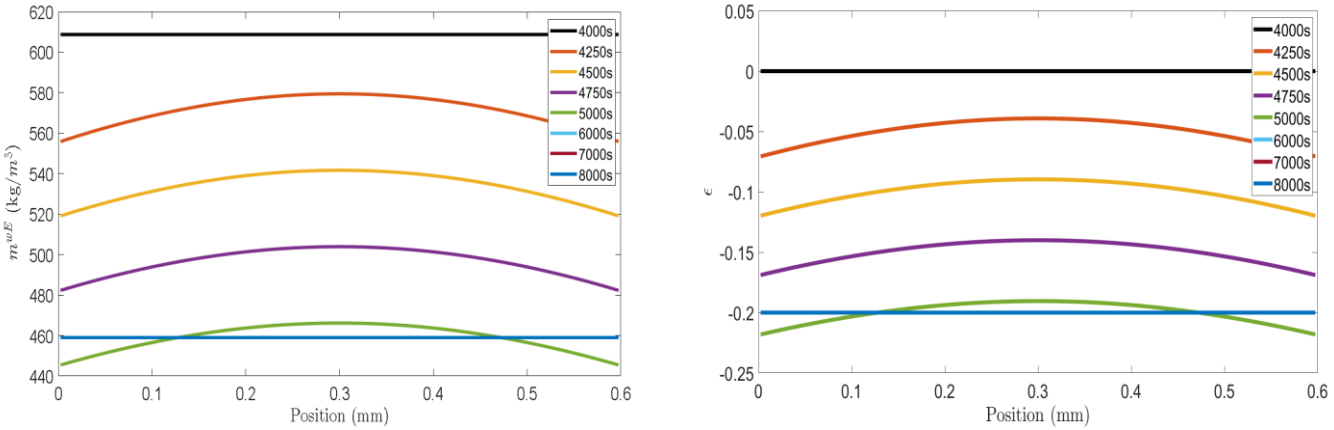

(a) (b)

Fig.8 - Time evolution of the spatial distribution, along the tissue thickness, of the water mass content m^{wE} (a) and of the local tissue deformation ε (b), during stages 3 and 4. The upward motion of the lower boundary and downward motion of the upper boundary are reflected first close to the vicinity of these boundaries, leading to an initial quicker decrease of mass content in these zones.

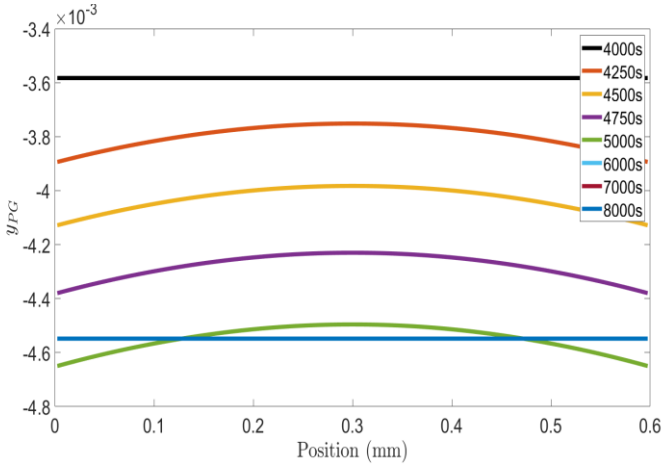

Fig.9 - Time evolution of the spatial distribution, along the tissue thickness, of the proteoglycan effective molar fraction y_{PG}, during stages 3 and 4. The significative increase in the absolute value of the proteoglycan effective molar fraction is due to the observed strong decrease of the water mass content.

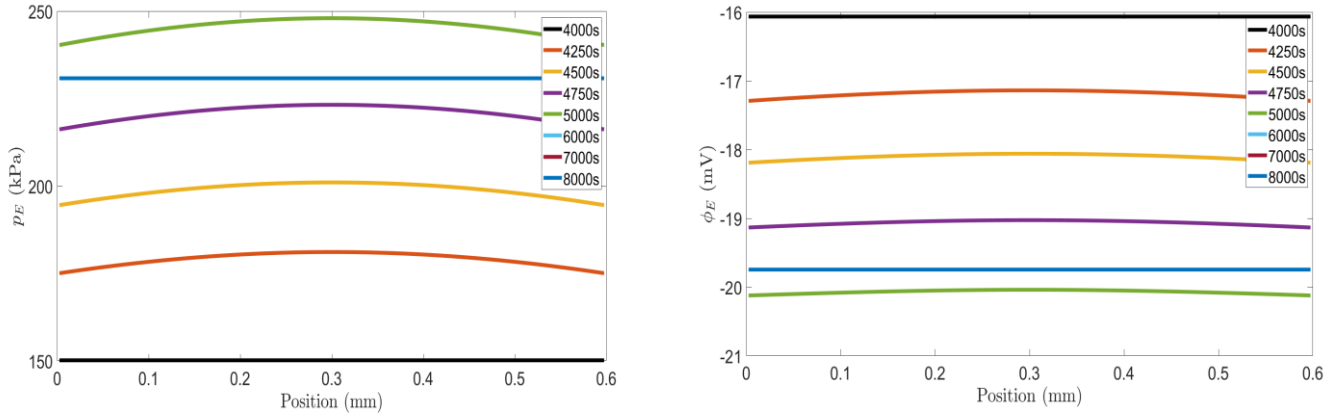

(a) (b)

Fig.10 - Time evolution of the spatial distribution, along the tissue thickness, of the EF water pressure p_E (a) and of the EF electrical potential ϕ_E (b), during stages 3 and 4.

The time evolution of the uniform axial stress (Fig.11(a)) shows, during the change of the bath composition (stage 1), a slight increase due to the increase of the water mass content and of the EF water pressure. Once the compression starts at stage 3, with the chemical environment kept constant, the stress suffers a significant increase in absolute value.

In Fig.11(b), it may be observed that the tissue thickness does not change during the first two stages and it decreases, according to the imposed deformation, during the third stage.

Alterations in the period of time during which the bath concentration is changed (stage 1) introduce modifications in the response of the tissue. By making faster the decrease of the ionic content of the bath (t_1 = 100 s), the stimulus felt by the tissue is more abrupt, which is reflected in the presence of a more distinct overshoot in the stress underwent by the tissue during stage 1 (see Fig.12(a)). On the contrary, if the alteration in the concentration of ions in the bath is made slower (t_1 = 5000 s), the tissue has more time to adapt to the imposed changes, and the overshoot is almost completely absent (see Fig.12(b)).

The hydraulic conductivity (K_h) is a characteristic property of porous tissues which describes the ease of a fluid to flow through the pores (percolation), thus being an indicator of the permeability of the porous medium. This property depends on the medium by itself (*i.e.* pore size, pore distribution and connectivity) but also on the properties of the fluid (*e.g.* density and viscosity) [7]. The higher its value, the higher the permeability is. In order to quantify the influence of the hydraulic conductivity in the behavior of the tissue, its value is changed from the base value 9.8×10^{-12} m/s (see Table 2) to higher (9.8×10^{-11} m/s) and lower (9.8×10^{-13} m/s) values.

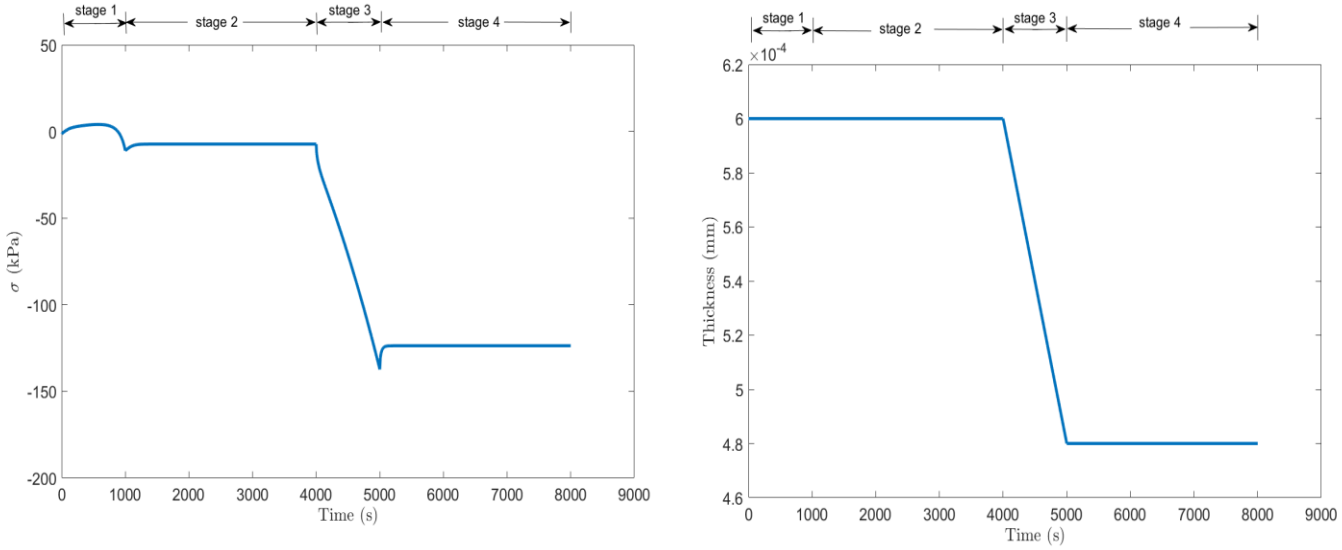

(a) (b)

Fig.11 - Time evolution of the axial stress in the tissue (a) and of the tissue thickness (b), during the four-stage simulation. After each of the stages involving external chemical (stage 1) and mechanical (stage 3) changes, the stress reaches equilibrium during stages 2 and 4.

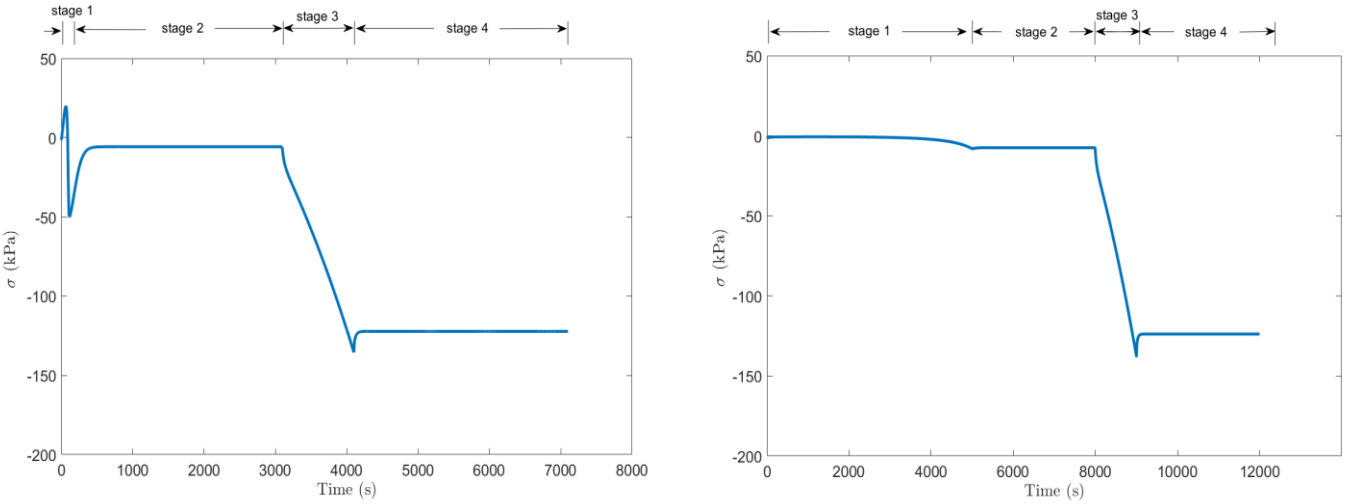

(a) (b)

Fig.12 - Time evolution of the axial stress underwent by the tissue, considering, for stage 1, a duration of 100 s (a) and 5000 s (b), during the four-stage simulation. After each of the stages involving external chemical (stage 1) and mechanical (stage 3) changes, the stress reaches equilibrium during stages 2 and 4.

As K_h is assigned with successive lower values, water does not flow through the tissue so easily, which means that a higher compressive stress is required to impose the same contractive deformation. This behavior can be verified analyzing the evolution of the stress over time presented in Fig.13(a). On the contrary, when the permeability increases (Fig.13(b)) equilibrium at stage 4 is attained very quickly with almost no overshoot. During the change of the bath composition, differences among the distinct permeability values are not as evident as during the imposition of the deformation. Nevertheless, at the end of the first stage a lower compressive stress is obtained for the lower K_h value, which may be explained due to the fact that water does not flow towards inside the tissue as easily leading to a lower EF water pressure and consequently to a lower compressive stress. Regardless the hydraulic conductivity, at the end of the second and fourth equilibrium stages the final stresses are the same. It should be mentioned that the rapid changes observed in Fig.12(a) and Fig.13(b) have been cross-checked by reducing the time step.

One additional note that should be considered is that the hydraulic conductivity and, consequently, the permeability, depends on the strain applied to the tissue, meaning that under higher deformation states the size of the pores is reduced and the fluid flow becomes more difficult (reduced permeability). In this way, although considered constant in this work,

the hydraulic permeability could have been defined in a way that would depend on the available pore volume for the movement of the fluid inside the tissue. Such dependence was taken into account in [1], based on the Kozeny-Carman equation.

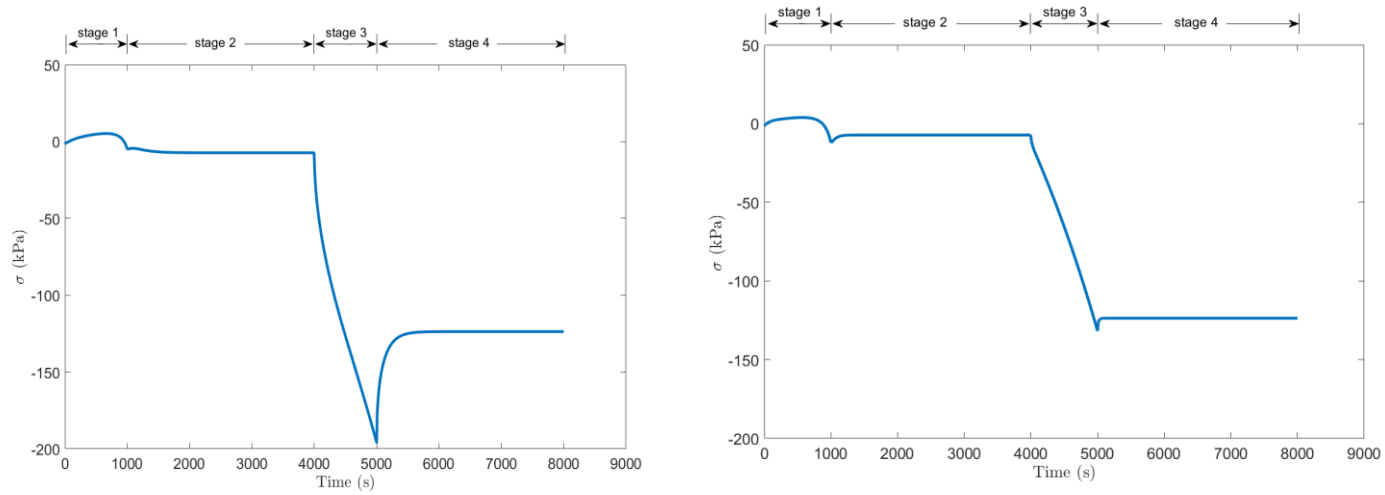

Fig.13 - Time evolution of the axial stress underwent by the tissue, considering a hydraulic conductivity, K_h, equal to 9.8×10^{-13} m/s (a) and equal to 9.8×10^{-11} m/s (b), during the four-stage simulation. After each of the stages involving external chemical (stage 1) and mechanical (stage 3) changes, the stress reaches equilibrium during stages 2 and 4.

The reach of the new equilibrium state after each of the chemical or mechanical changes is not accomplished instantaneously as it is highlighted in each and every one of the figures mentioned above. Instead, the tissue response undergoes a transient period. Such transient time is related with several material properties such as the percolation time related to Darcy's law and the diffusion time related to Fick's law. In the case of absence of electro-chemo-mechanical couplings, the characteristic times of the ionic diffusion and water seepage are given by $\tau_k^{Fick} = 1/(4\pi^2)\, L^2/D_{kE}^*$ and $\tau^{Darcy} = 1/(4\pi^2)\, L^2/(E_e\, k_{EE})$, respectively, with $D_{kE}^* = \tau\, D_{kE}$, τ the tortuosity factor, L the distance traveled by ions and water, E_e the confined compression modulus and k_{EE} the "short-circuit" permeability.

Analyzing the figures related to the evolution of stress during the stages where the equilibrium is reached (2 and 4), it is possible to retrieve that the equilibrium is attained faster in stage 4 than in stage 2. In Fig.11, the times required to reach the plateau, in stages 2 and 4, are 474 s and 203 s, respectively. This trend is in agreement with the individual times of diffusion and percolation, which, in the present case, are: $\tau_{Na}^{Fick} = 4.285$ s and $\tau^{Darcy} = 3.5658$ s. Since, in the second stage, the system evolution mainly depends on diffusion as a response to the bath chemical alteration, while in the fourth stage the evolution mainly depends on the water flow as a response to the applied deformation, the faster achievement of equilibrium during stage 4 is plausible. However, the characteristic times here presented do not account for the coupled interactions from which the tissue response depends. Of course, the time necessary to reach the equilibrium states depends on the period of time during which the modifications are introduced. The slower the changes in the bath composition or in the imposed deformation are introduced, the faster the equilibrium is reached. In these simulations the same period of time is selected for stages 1 and 3, where the chemical and mechanical actions are imposed. It is observed that a period of time equal to 50 minutes is larger than necessary for the equilibrium to be achieved and, therefore, in the following simulations a period of time equal to 1000 s is considered in stages 2 and 4.

The computational time taken to conduct the four stages of this simulation, with 50 finite elements and a time step of 0.1 s within a total simulation time of 8000s, is around 4 hours using a PC with the following characteristics: Intel Core i7-8750H 2.20 GHz processor and 8 GB of RAM.

3.3. Eisenberg and Grodzinsky simulation

The finite element program is also used to obtain several stress-strain equilibrium points, for different bath concentrations and different contractive deformations, in order to compare with the experimental results by Eisenberg and Grodzinsky [3]. Several simulations similar to the one presented in section 3.2 are then performed imposing, in stage 1, different bath concentrations in the range showed in [3] and imposing, in stage 3, different contractive deformations.

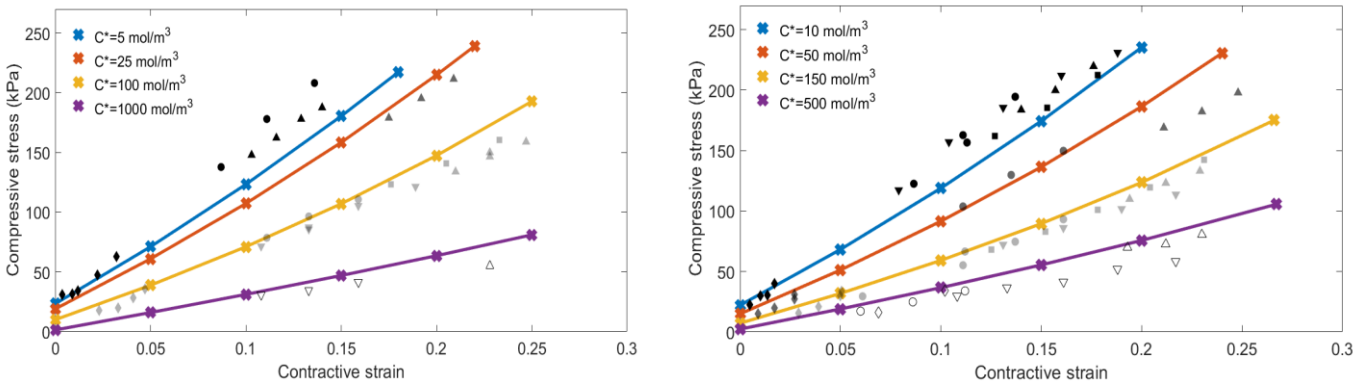

Fig.14 - Stress-strain curves obtained in the finite element simulation using the material parameters specified in section 2. Marked with a × are the steady state points obtained for a given bath concentration and a given contractive deformation. The experimental points by Eisenberg and Grodzinsky [3] are represented with black symbols.

In Fig.14, the stress-strain equilibrium points are represented with a cross (values retrieved at the end of stage 4), along with the respective interpolation curves. The results show that the finite element simulation, using the proposed mechanical model and considering the IF phase as described before, properly simulates the real cartilage behavior captured in these experiments, which is something that Loix *et al*. [1] were not able to simulate.

3.4. Heterogeneous bath simulation

The introduction of the *fictitious bath* concept in the formulation of the constitutive model makes possible to conduct a simulation in which the tissue sample is surrounded by a heterogeneous bath (Fig.15). In such experimental framework, the bath presents a physical horizontal separation which allows each of the sample extremities to experience distinct variations of the salt concentration over time.

To conduct a simulation with a heterogeneous change of the bath chemistry, two different final concentrations are imposed, starting from the initial bath concentration of 1000 mol/m^3: in the upper side, the final concentration is set to 250 mol/m^3 and, in the lower side, it is set to 150 mol/m^3. Once the chemical change is performed at a constant rate during a time equal to 1000 s, with the next 1000 s stage to reach the equilibrium state, a 20% negative deformation is imposed during 1000 s, followed by another 1000 s equilibrium stage (see Fig.15).

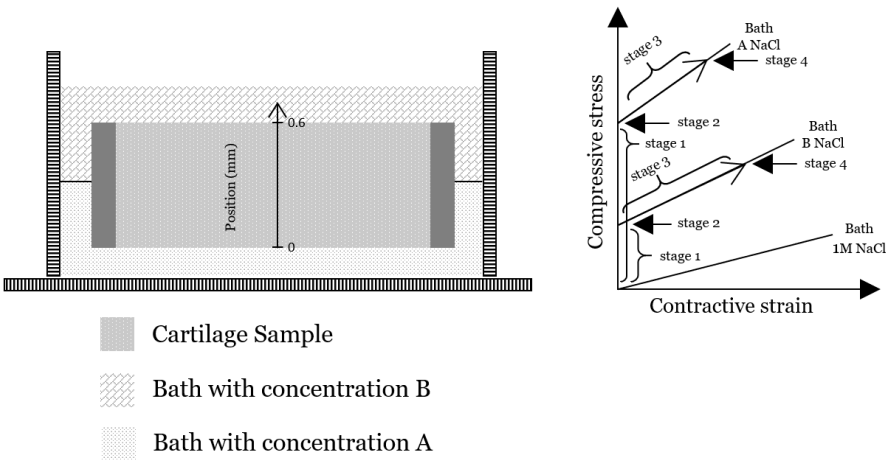

Fig.15 - Schematic of a cylindrical tissue sample, with 0.6 mm thickness, immersed in a piecewise heterogeneous bath, with a horizontal physical division, separating the area of concentration A (at the bottom) from the area of concentration B (at the top).

When imposing a change in the chemical content of the bath that is different in the two extremities of the tissue sample, the behavior in the extremity nodes in reaction to the external modifications is predictable, since it is in these

nodes that the changes are imposed. However, the way the response to the stimulus progresses towards inside the tissue sample is not that straight forward.

Looking at Fig.16, profiles similar to those obtained in section 3.2 are shown, being the distribution of the ionic mass contents, at the end of stage 2, now not uniform along the tissue thickness since the heterogeneity of the bath composition contributes to the loss of symmetry in the tissue behavior, which is also perceptible in all the figures that follow. The side of the tissue sample with the higher EF ionic mass contents corresponds to the side in contact with the bath with higher final ionic concentration.

The water mass content and the local deformation are also no longer uniform, neither symmetric, after the new equilibrium state has been reached. In Fig.17(a), after the equilibrium is restored under no variation of thickness, an increase in the water mass content is verified in general along the tissue thickness, since in both sides of the bath there is a significant decrease in the salt concentration. Nevertheless, the water mass content is higher on the lower side of the sample, where a lower final bath concentration is imposed, since it is in this extremity that a higher outflow of ions occurs. Due to this non-uniform behavior of the tissue, although maintaining an overall zero deformation, the local deformation ε presents a non-zero value in the upper extremity of the sample (see Fig17(b)).

The proteoglycan effective molar fraction y_{PG} presents the same trend as the deformation, that results from the uneven distribution of water inside the tissue (see Fig.18). The range of y_{PG} values is maintained in comparison to previous simulations.

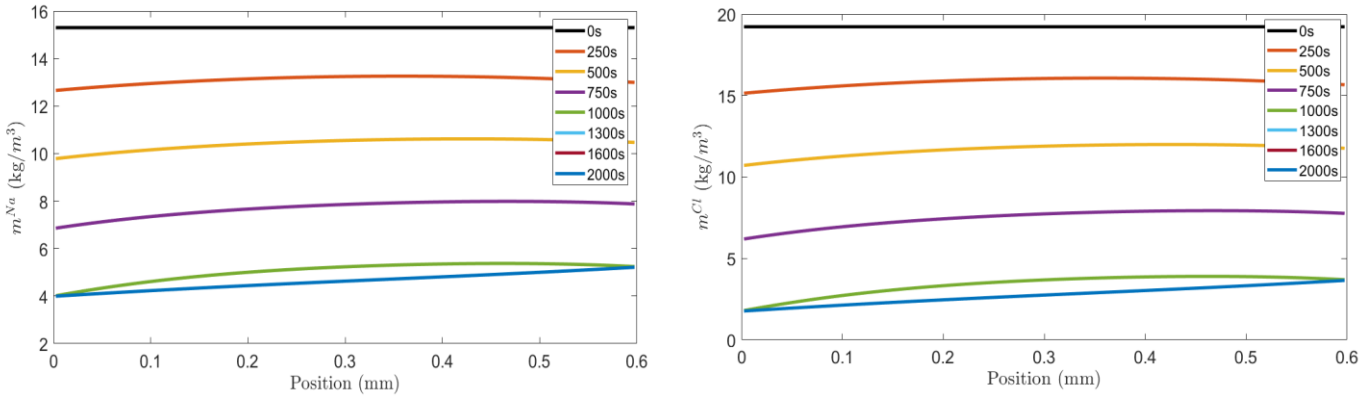

(a) (b)

Fig.16 - Time evolution of the spatial distribution, along the tissue thickness, of the sodium (a) and chloride (b) ionic mass contents, m^{NaE} and m^{ClE}, during stages 1 and 2, for a heterogeneous change in the salt concentration of the bath. The last three curves are practically superimposed which means that steady state is practically reached at t = 1300 s. The same type of behavior can be observed next in Fig.17 to Fig.19.

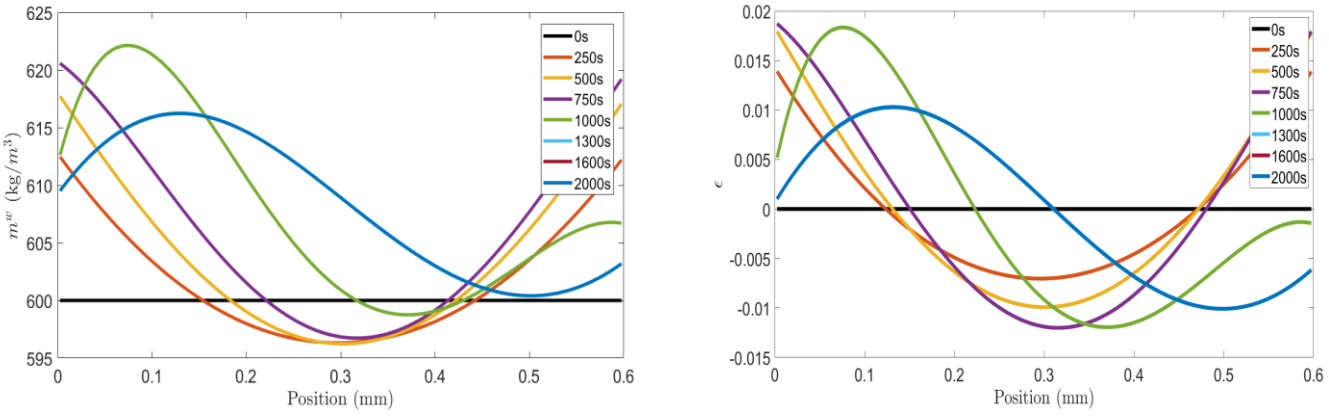

(a) (b)

Fig.17 - Time evolution of the spatial distribution, along the tissue thickness, of the water mass content m^{wE} (a) and of the local tissue deformation ε (b), during stages 1 and 2, for a heterogeneous change in the salt concentration of the bath.

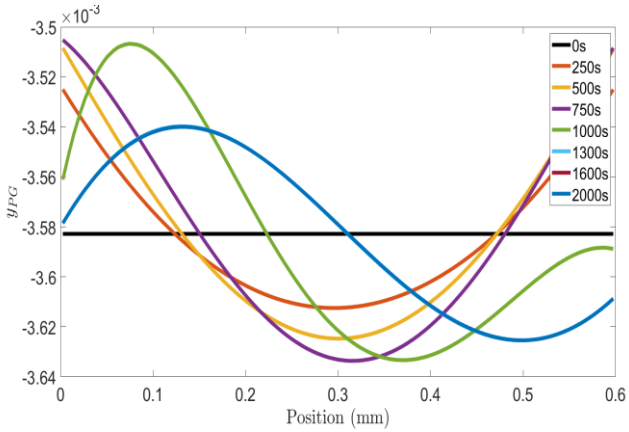

Fig.18 - Time evolution of the spatial distribution, along the tissue thickness, of the proteoglycan effective molar fraction y_{PG}, during stages 1 and 2, for a heterogeneous change in the salt concentration of the bath.

In Fig.19, the EF water pressure and EF electrical potential profiles, during the first two stages, are presented. The rational behind the obtained curves follows the same line as described in the case of a homogeneous bath.

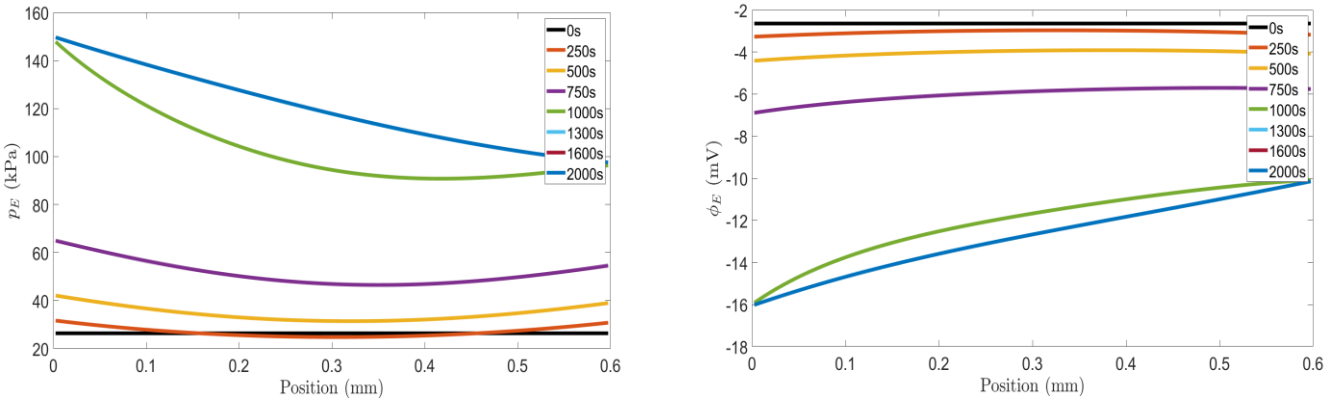

(a) (b)

Fig.19 - Time evolution of the spatial distribution, along the tissue thickness, of the EF water pressure p_E (a) and of the EF electrical potential ϕ_E (b), during stages 1 and 2, for a heterogeneous change in the salt concentration of the bath.

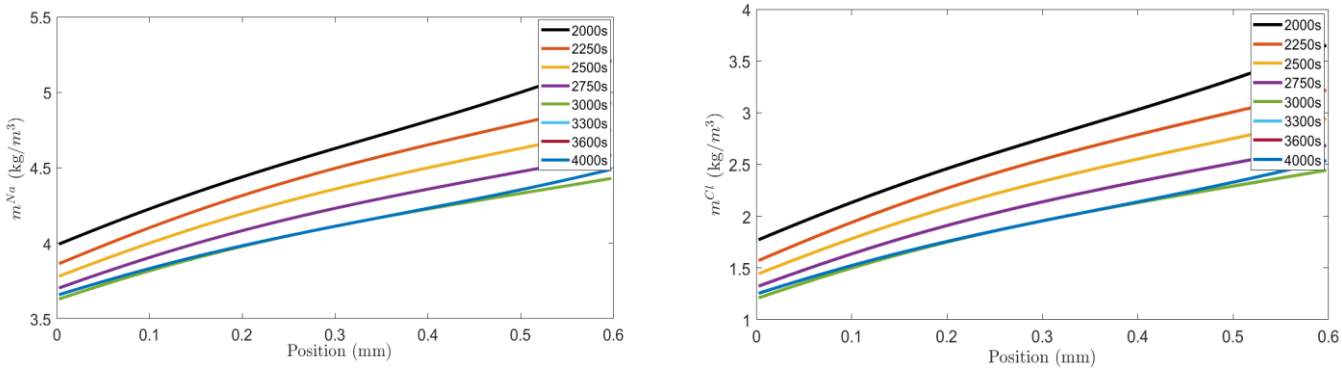

(a) (b)

Fig.20 - Time evolution of the spatial distribution, along the tissue thickness, of the sodium (a) and chloride (b) ionic mass contents, m^{NaE} and m^{ClE}, during stages 3 and 4, for a heterogeneous change in the salt concentration of the bath. The last three curves are practically superimposed which means that steady state is practically reached at t = 3300 s. The same type of behavior can be observed next in Fig.21 to Fig.23.

When the contractive deformation is imposed, the evolution of the different variables until equilibrium is reached occurs much like in the case of the homogeneous bath (this is due to the fact that mechano-chemical coupling is not so strong as the chemo-mechanical coupling), the only difference being that in the current simulation the starting state of

stage 3 is not uniform, and thus the results obtained after the imposed deformation (Fig.20 to Fig.23) are not uniform as well.

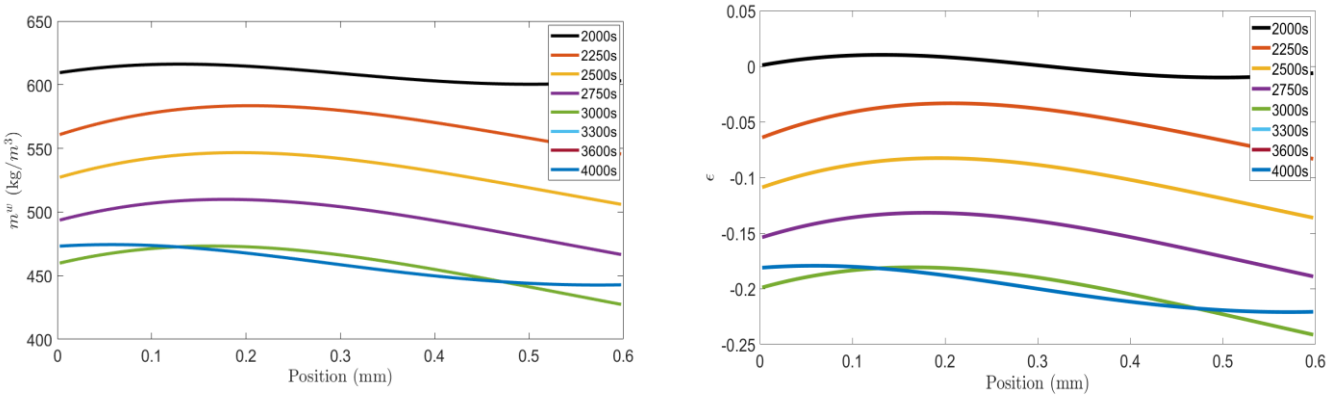

(a) (b)

Fig.21 - Time evolution of the spatial distribution, along the tissue thickness, of the water mass content m^{wE} (a) and of the local tissue deformation ε (b), during stages 3 and 4, for a heterogeneous change in the salt concentration of the bath.

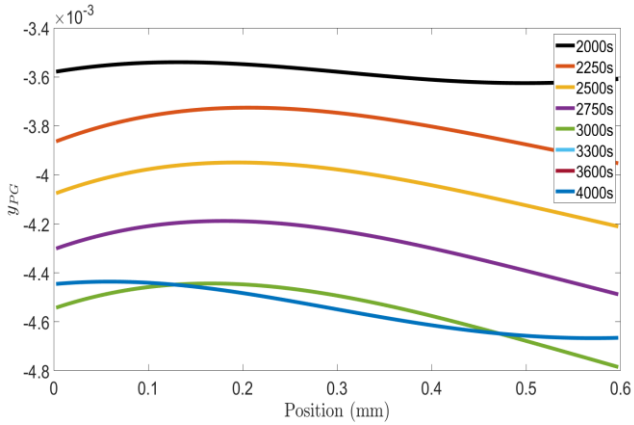

Fig.22 - Time evolution of the spatial distribution, along the tissue thickness, of the proteoglycan effective molar fraction y_{PG}, during stages 3 and 4, for a heterogeneous change in the salt concentration of the bath.

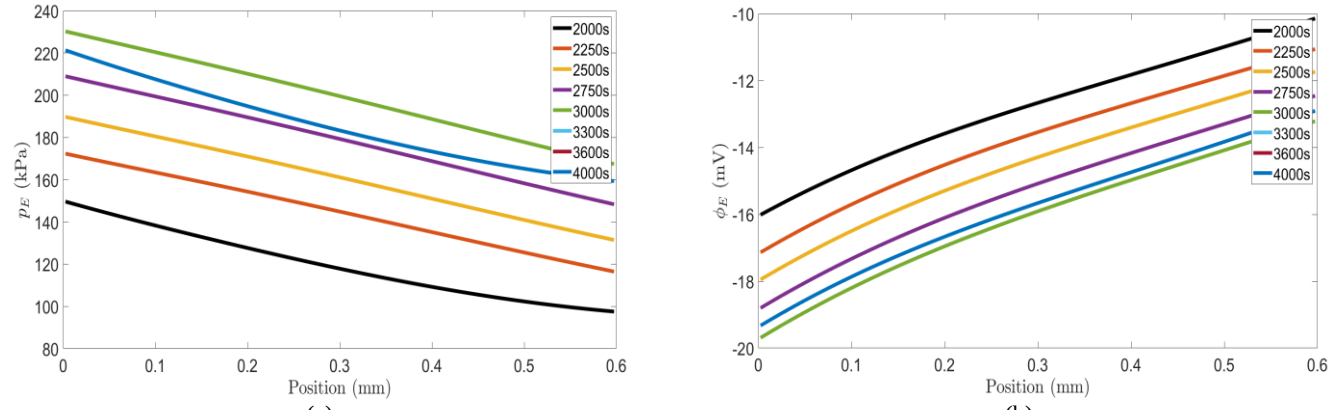

(a) (b)

Fig.23 - Time evolution of the spatial distribution, along the tissue thickness, of the EF water pressure p_E (a) and of the EF electrical potential ϕ_E (b), during stages 3 and 4, for a heterogeneous change in the salt concentration of the bath.

The time evolution of the stress is shown in Fig.24, where it may be observed that, at the end of stage 4, the compressive stress is a little lower than the one registered in the case of the homogeneous bath (section 3.2). This result

is expected, since one of the baths has the same final concentration as the homogeneous bath (150 mol/m^3), while the second bath has a higher final concentration (250 mol/m^3). In contrast to the case of the homogeneous bath, there are now some points in the tissue in which the sodium mass content is higher, thus implying a higher shielding of the repulsive forces which is translated in a lower tissue compressive stiffness. In this way, the compressive stress required to impose a negative deformation of 20% is lower as well.

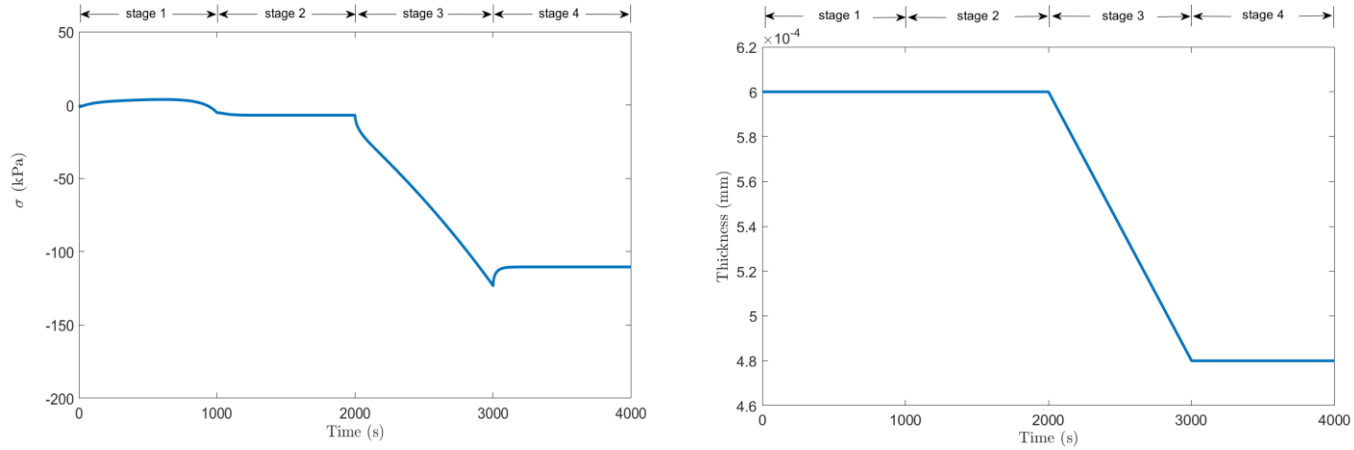

(a) (b)

Fig.24 - Time evolution of the axial stress in the tissue (a) and of the tissue thickness (b), during the four-stage simulation, for a heterogeneous change in the salt concentration of the bath during the first two stages of the simulation. After each of the stages involving external chemical (stage 1) and mechanical (stage 3) changes, the stress reaches equilibrium during stages 2 and 4.

4. Conclusions

In this work, a finite element program, whose formulation is based on the model described in the companion paper, is developed in a MATLAB environment and used to numerically simulate the response of an articular cartilage sample to a combination of chemical and mechanical actions. The sample of articular cartilage is found immersed in a bath whose chemical composition may be altered, while the tissue-bath interface is considered to steadily remain at electro-chemical equilibrium. However, the equilibrium inside the tissue is not reached instantaneously. In fact, the time required to establish steady state depends on the problem geometry and on several material properties, such as the percolation and diffusion times related to Darcy's and Fick's laws, respectively. Therefore, spatial and temporal profiles are obtained, for several mechanical, chemical and electrical variables defined in the interior of the tissue, due to either isolated or combined actions of chemical (changing of the chemical composition of the external bath) and mechanical (confined compression) loadings. The framework may also simulate tests where the electrical field of the bath is altered but this type of simulations is not reported here.

Using the finite element method, with the new constitutive equation proposed in [2], the experimental stress-strain curves obtained in [3] are successfully modelled. In particular, the observed shielding effect is very well reproduced by the model, which is something that other existing articular cartilage chemo-mechanical models (*e.g.* [4]) and existing finite element software packages based on those models (like FEBio [5]) are not able to replicate, since they assume a constant stiffness for the tissue. The good approximation of the real tissue behavior allows, additionally, to conclude that the simplification regarding the contribution of the IF phase in this model still permits to obtain acceptable outcomes, being this an advantage of the current formulation with respect to the one developed by Loix *et al.* [1] where several material parameters and functions were defined without experimental validation.

The concept of *fictitious* or *equilibrium bath* also allows to obtain spatial and temporal profiles of several variables when the sample is immersed in a heterogeneous bath which gives a closer insight to the tissue mechanical behavior under a more diverse environment. This is something that other existing chemo-mechanical models are not able to provide.

The control of the tissue response to mechanical, chemical and electrical actions is crucial in the improvement of prevention and treatment of its degenerative disease as well as in the development of novel engineered tissues, mimicking the biological and mechanical properties of the tissue, that could be used in regenerative medicine.

Appendix A. Mesh and time convergence analysis

For the study of the influence of mesh size on the convergence of the method, simulations are conducted with 6 meshes comprising different number of finite elements with a successively higher refinement: 6, 12, 25, 50, 100 and 200 elements, all of them using the same integration time Δt equal to 1 s. For each mesh, several variables (both primary and secondary) are extracted at 3 fixed points (point 1 at the extremity of the sample and points 2 and 3 at 100 μm and 300 μm from the extremity, respectively, see Fig.2) in order to study the evolution of their values as a function of the mesh refinement. The evaluation of the variables is performed at the end of the second stage, once the equilibrium is restored, after the change of the bath composition during stage 1 to a chosen final concentration equal to 150 mol/m^3.

From Fig.A.1, a convergent trend is perceptible for the considered variables. Even if some curves seem not to tend to an asymptotic value, the numerical values are very close, thus reflecting a good rate of convergence. In fact, it may be observed that the considered mesh refinement has almost no influence on the results, since the maximum observed variation with respect to the values of the finer mesh (with 200 finite elements) is only 0.003%. In this way, the number of elements that is considered to allow a satisfactory convergence of the results, whilst not compromising the computational effort, is equal to 50.

For the study of the influence of the time step on the convergence of the method, simulations are conducted with a mesh of 50 finite elements. Three different time steps Δt = (Time stage)/(Number of steps) are tested: 1 s, 0.1 s and 0.01 s. For each time step, spatial profiles of several variables are obtained along the tissue thickness. Analyzing the results presented in Fig.A.2, obtained again at the end of stage 2, a convergent trend is perceptible for the considered variables. The fact that some of the curves, computed with the smallest time step, seem not to be completely flat may be related to the fact that the mesh used in these simulations was not very refined. Since the values of the variables obtained for the two lower time steps (0.1 s and 0.01 s) are, again, very close, a value of Δt = 0.1 s is considered to reduce the time step influence on the results, without increasing excessively the computational cost.

References

[1] Loix F, Simões FMF, Loret B. Articular cartilage with intra and extrafibrillar waters - Simulations of mechanical and chemical loadings by the finite element method. Computer Methods in Applied Mechanics and Engineering. 2008;197(51-52):4840–4857.

[2] Loret B, Simões FMF. Effects of the pH on the mechanical behavior of articular cartilage and corneal stroma. International Journal of Solids and Structures. 2010;47(17):2201–2214.

[3] Eisenberg SR, Grodzinsky AJ. Swelling of articular cartilage and other connective tissues: Electromechanochemical forces. Journal of Orthopaedic Research. 1985;3(2):148–159.

[4] Gu WY, Lai WM, Mow VC. A mixture theory for charged-hydrated soft tissues containing multi-electrolytes: passive transport and swelling behaviors. Journal of Biomechanical Engineering. 1998;120:169–180.

[5] FEBio. Available from: https://febio.org/

[6] Maroudas A. Biophysical chemistry of cartilaginous tissues with special reference to solute and fluid transport. Biorheology. 1975;12(3-4):233–248.

[7] Ren X, Zhao Y, Deng Q, Kang J, Li D, Wang D. A relation of hydraulic conductivity - void ratio for soils based on Kozeny-Carman equation. Engineering Geology. 2016;213:89–97.

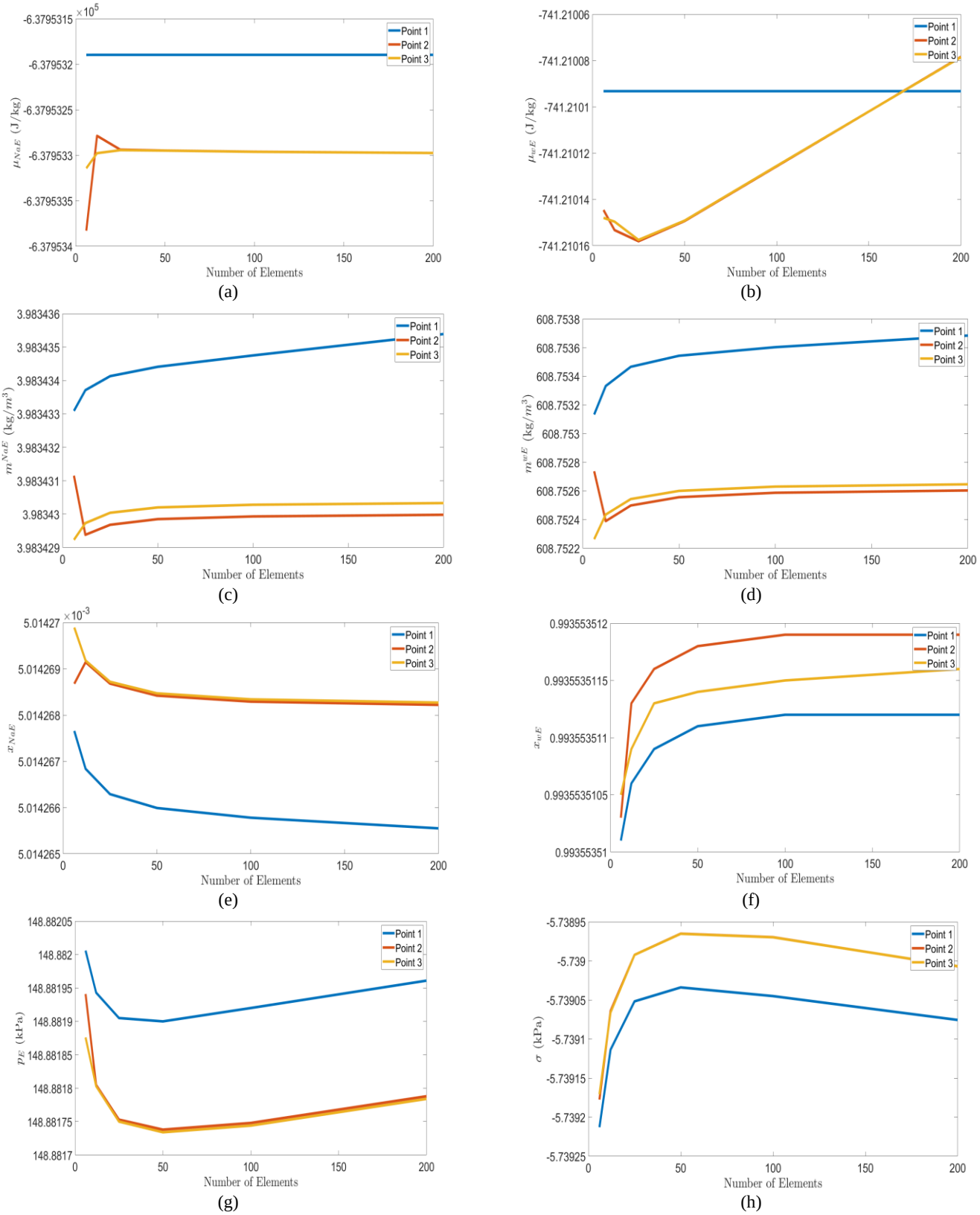

Fig.A.1 - Spatial convergence analysis for several variables (electrochemical potentials of extrafibrillar sodium μ_{NaE}^{ec} (a) and water μ_{wE}^{ec} (b), mass contents of extrafibrillar sodium m^{NaE} (c) and water m^{wE}(d), molar fractions of extrafibrillar sodium x_{NaE} (e) and water x_{wE} (f), extrafibrillar water pressure p_E (g) and axial stress σ(h),with values taken at the steady state at end of stage 2 after a change of the bath concentration), at three different spatial positions. Numerical values being so close in each figure reflects the good rate of convergence.

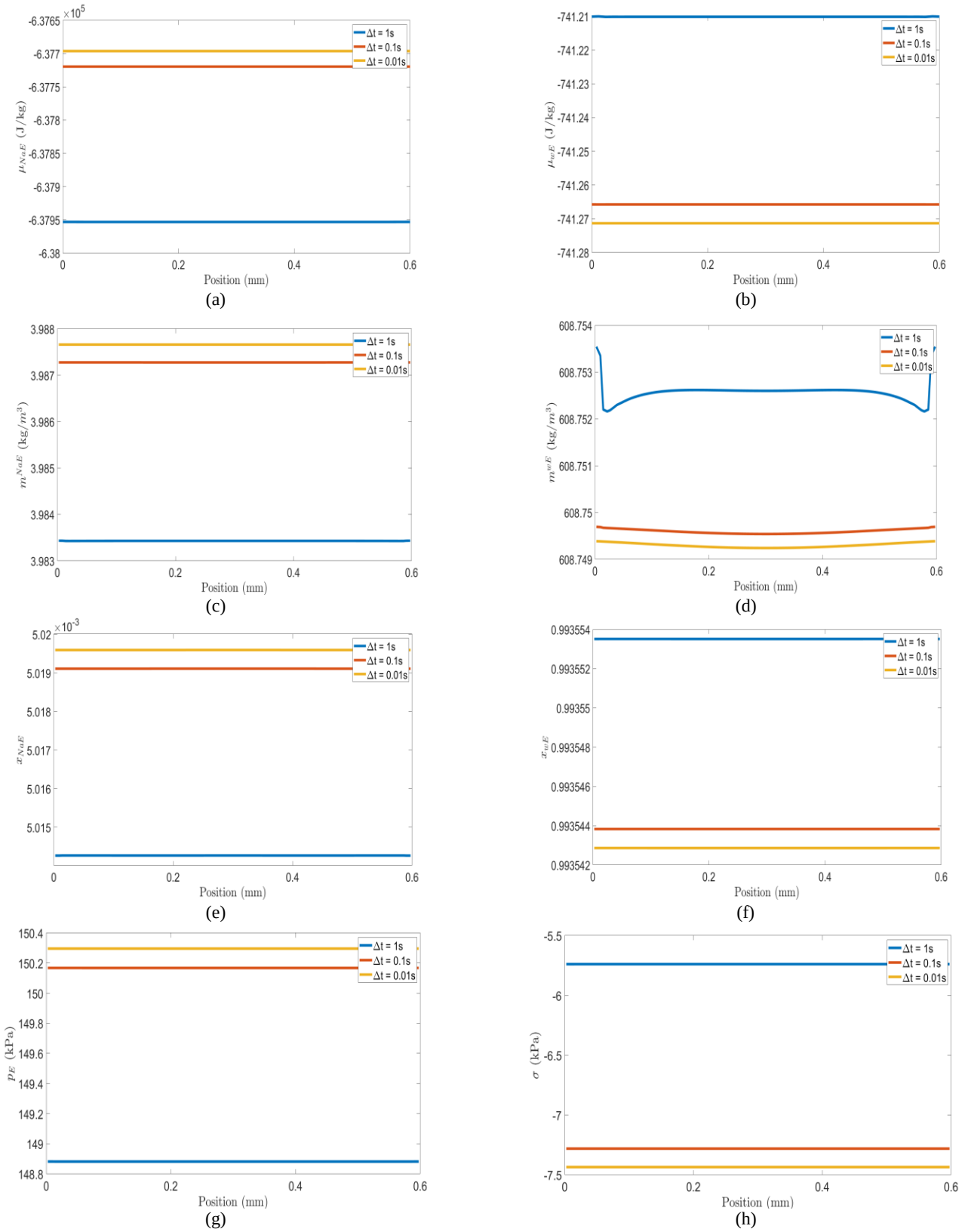

Fig.A.2 - Time convergence analysis for several variables (electrochemical potentials of extrafibrillar sodium μ_{NaE}^{ec} (a) and water μ_{wE}^{ec} (b), mass contents of extrafibrillar sodium m^{NaE} (c) and water m^{wE}(d), molar fractions of extrafibrillar sodium x_{NaE} (e) and water x_{wE} (f), extrafibrillar water pressure p_E (g) and axial stress σ(h), with values taken at the steady state at end of stage 2 after a change of the bath concentration), considering three different time steps: 1s, 0.1s and 0.01s. Numerical values being so close in each figure reflects the good rate of convergence.

Journal of Computation and Artificial Intelligence in Mechanics and Biomechanics ISSN 2184-8971
Volume 2, Issue 1, Page 35-43, 2022

Structural analysis of the new Bioactive Kinetic Screw in titanium alloy vs. commercially pure titanium

Carlos Aurelio Andreucci [1], Elza M. M. Fonseca [2], Renato N. Jorge [3]

[1] *PhD Engenharia Biomédica, FEUP | Faculdade de Engenharia do Porto; candreucci@hotmail.com;Porto; Portugal*
[2] *LAETA, INEGI, Mechanical Engineering Department, School of Engineering, Polytechnic Institute of Porto; elz@isep.ipp.pt; Porto;Portugal*
[3] *LAETA, INEGI, Mechanical Engineering Department, Faculty of Engineering, University of Porto; ; rnatal@fe.up.pt; Porto; Portugal*

Abstract
This study presents the structural and static analysis of the new Bioactive Kinetic Screw (BKS) using the finite element method (FEM). The FEM was conducted to predict three-dimensional (3D) simulations according to a cutting torque applied at a constant feed rate. The results were compared using two different materials in the BKS simulation: commercially pure titanium (cp-Ti) and titanium alloy (typically Ti6Al4V). BKS modelling was done in Solidworks ® and the FEM analysis was performed in the ANSYS Workbench 2020 R2 ® software. According to the results, it was observed that the low imposed cutting torque and BKS in cp-Ti material are recommended to obtain a less effective stress in the screw. In addition, the low imposed cutting torque and BKS in Ti6Al4V material are recommended to obtain less equivalent strain and total deformation level in the screw.

***DOI**: 10.5281/zenodo.7406075*

Article Info

Keywords
Bioactive Kinetic Screw
Drilling parameters
Finite Element Method
Simulation

Article History
Received: 30/01/2022
Revised: 02/05/2022
Accepted: 03/09/2022

1. Introduction

Drilling is the most used process to produce holes, and it is essential for different industries and clinical medical centers [1]. To minimize time and costs of the experimental tests of the cutting process, before use, computer models have become more numerous, providing accurate and safe conditions [2]. Many researchers have developed analytical, numerical, and experimental tests to predict and control different drilling parameters [1-7].

Numerical methods based on the finite element analysis (FEA) are widely used presenting many advantages compared to other methodologies, due the reduction of the cost, to avoid wasting time during analysis, as well as faster designer of any component [8]. This method allows finding the approximation solution of partial differential equations of analysis due to the boundary conditions imposed on the problem.

FEA is extensively used in many fields, originally developed for numerical solutions of complex problems in solid mechanics [9]. FEA has been recognized as a crucial solution to a variety of structural, modal, fatigue, thermal, fluid, or electromagnetic design problems. Nowadays, different range of purposes are applied in all these domains, namely in implantology [10].

FEA can simulate the interaction between the implant and the surrounding bone. Some different studies allow the identification of load transfer at the bone-implant interface, which depends on the type of load, material properties, geometry (diameter, shape, length), among other characteristics [10].

Different studies have been focused on optimizing the implant geometry to provide the favorable stress level for different static or dynamic conditions of applied load, due the interaction between the implant and the surrounding bone [10].

For dental implants a range of different material have been recommended [10-13]. Typical materials used are: Pure Ti (cp-Ti), Ti6Al4V, Type 3 gold alloy, Ag-Pd alloy, Co-Cr alloy and Porcelain, [10, 12-13]. In the most reported studies, the materials are assumed to be homogeneous, linear and have elastic materials characterized by Young's Modulus and Poisson's Ratio [10, 12-13].

In the present study, commercially pure titanium (cp-Ti) and titanium alloy (typically Ti6Al4V) were chosen for the analysis of the new BKS. Titanium dental implants can offer many advantages. They have excellent characteristics, namely excellent corrosion resistance, passivation capacity and biocompatibility [11-14]. According to investigations by

Corresponding author:
Carlos Andreucci
candreucci@hotmail.com

Shah et al. [11] concluded that, under experimental conditions, cp-Ti and Ti6Al4V provide similar osseointegration and biomechanical anchorage. Furthermore, the authors concluded that machined surfaces exhibit similar morphology, topography, phase composition and chemistry [11]. The choice of implant materials can greatly affect the stress concentrations at the implant-bone interface that is still under discussion [10].

Different authors have been studied the effect of the drilling force and torque as important parameters to avoid overloading the bone tissue [14]. Another important parameter is related with the bone temperature caused by the drilling. According to the study by Alam et al. [14] the decrease in bone temperature was attributed to the reduced time required for the drill to penetrate the bone, as a function of the drill rotation speed. In all experiments, the authors used a range between 600 to 3000 rpm for the drilling speed with constant feed rate [14]. According to a protocol, established by the research from Mihali et al. [15], for reducing the drilling sequence during implant preparation, based on temperature and insertion torque, the mean torque that the authors have been applied to all bone densities was a range between 44.12 and 45.04 Ncm, with a rotational speed of 800 rpm.

In this work, to analysis and measure the drill resistance capacity as a function of the applied torque, a 3D finite element model of the new BKS (at 4mm in diameter and 10 mm in length) was tested using two materials: titanium alloy Ti6Al4V (Grade 5) and commercially pure titanium cp-Ti (Grade 4). This new BKS presents itself a new delivery system for the use of natural growth factors, since the characteristic is to introduce protein molecules, cells, blood, and particulate bone through the hole of the BKS by a system of drill flutes; it also becomes a new means of delivering growth factor in surgery for expansion, lifting and bone fixation [16]. The main objective of this work was to identify the values of the cutting torque that must be applied in the BKS, depending on the rotational speed between 2250 to 4000 rpm, so that the ultimate strength of the material is not exceeded. The torque value is of great importance, since high values in the drilling can cause the drill breakage during the surgical incision [12, 17].

2. Material and Methods

In this research work, a 3D numerical and structural linear model was developed using ANSYS 2020 R2 ® - Workbench 2020 R2, with the new BKS biomechanism in Ti6Al4V (Grade 5) and commercially pure titanium cp-Ti (Grade 4). The mechanical properties of the materials used in the study are shown in Table 1.

Ti6Al4V Grade 5 alloy is the most commercially available of all titanium alloys. Widely applied to medical and biomedical implants, it offers an excellent combination of strength and toughness, corrosion resistance, good weld, and manufacturing characteristics.

Cp-Ti Grade 4 is an unalloyed titanium, with excellent corrosion resistance, good weld, high strength, and used in different types of industries.

Table 1 – Mechanical properties [11, 18].

	Ti6Al4V (Grade 5)	cp-Ti (Grade 4)
Young's Modulus, GPa	114	105
Poisson's Ratio	0.36	0.32
Ultimate Tensile Strength, MPa	896	553
Tensile Yield Strength, MPa	827	483

The numerical model aims to simulate the drilling process of the BKS biomechanism and evaluate the distribution of mechanical stresses and strains in the screw material. The 3D model was built using Solidworks ® and ANSYS 2020 R2 ® - Workbench 2020 R2 software, as shown in Fig.1.

Boundary conditions, which represent typical drilling phenomena, are established on the lower surface of the BKS as fixed, and on the upper surface with the application of torque, Fig.1(a). Based on the geometrical model, volumetric finite element meshes were generated using SOLID187. SOLID187 element is a higher order, defined by 10 nodes having three degrees of freedom at each node (translations in the nodal x, y, and z directions), Fig.1(b). This tetrahedron element has a quadratic displacement behaviour with four-point integration and is suitable for modelling irregular meshes, such as those produced from various CAD/CAM systems [19]. The simulations are based on Lagrangian finite element model performed to determine the effective stress and strain.

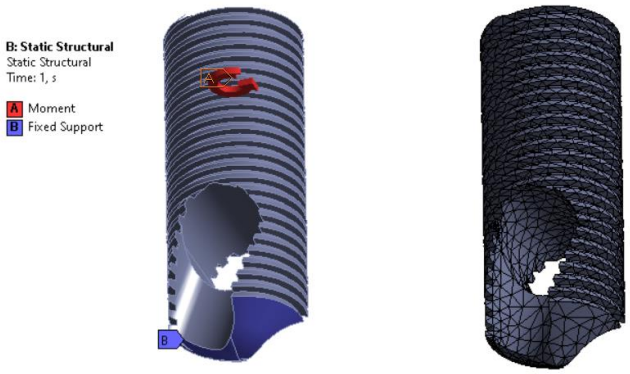

(a) (b)

Fig.1 – BKS model, static structural analysis (ANSYS 2020 R2 ® - Workbench 202 R2). (a) Boundary conditions. (b) Mesh.

In the present study, an electric motor EM-12L with a maximum power of 59 W was selected, and angular speeds between 100 and 40000 rpm [20].

The new BKS tool, intended for use in ongoing research, will work with different angular speeds depending on the material of which it is made, and with a constant feed rate of 0.5 mm/sec vertically downwards. In this study, only the mechanical load due to the cutting torque M_t was considered in the model and the thermal effect produced by the BKS was not considered in this simulation.

The relation between the torque (M_t in Nm), the maximum electrical power during drilling (P in W) and the speed of rotation (n in rpm) is determined according by Eq. (1) [19].

$$M_t = 9.55 \frac{P}{n} \tag{1}$$

3. Results and Discussion

In the present study, six numerical simulations were performed, varying the cutting torque according to the imposed and appropriated rotational speed for each BKS tool material, Table 2.

Numerical results of stress, strain and deformation level were obtained during the structural analysis on the BKS for different imposed cutting torques, according to the rotational speed from 2250 to 4000 rpm. The chosen drilling parameters were due to the obtained values for the ultimate tensile strength in the BKS, identified for an imposed rotational speed higher than 2250 rpm, as presented in Table 2. The obtained values of the cutting torque decrease with the increase of the rotational speed.

Table 2 – Drilling parameters.

Tool BKS	Power derived from cutting torque, Ref: Electric Motor EM-12L [20], P=59 W	
	Cutting torque, M_t Ncm	Rotational speed, n rpm
Ti6Al4V (Grade 5)	25.04	2250
	22.54	2500
	18.78	3000
cp-Ti (Grade 4)	17.34	3250
	16.10	3500
	14.09	4000

Before the simulations, different mesh convergence tests were performed, where the computational error was minimized by changing the number of elements, as shown in Fig.2.

(a) (b) (c) (d)

Fig.2 – Different mesh convergence. Number of elements in (a) 18175 (b) 18857 (c) 23215 (d) 76105.

Convergence tests were performed by changing the number of elements to obtain the maximum stress values verified at the tip of the BKS model and compared with the ultimate tensile strength of the material. As shown in Fig.3, in four solutions, the stress values converge where the smallest percent error obtained was 4.3% using 23215 finite elements. To obtain a finite element accuracy criterion of mesh discretization, an error smaller than 7% must be considered [8]. Accordingly, the mesh adopted to use in our simulations consists of a total of 23215 tetrahedron elements, Fig.2(c).

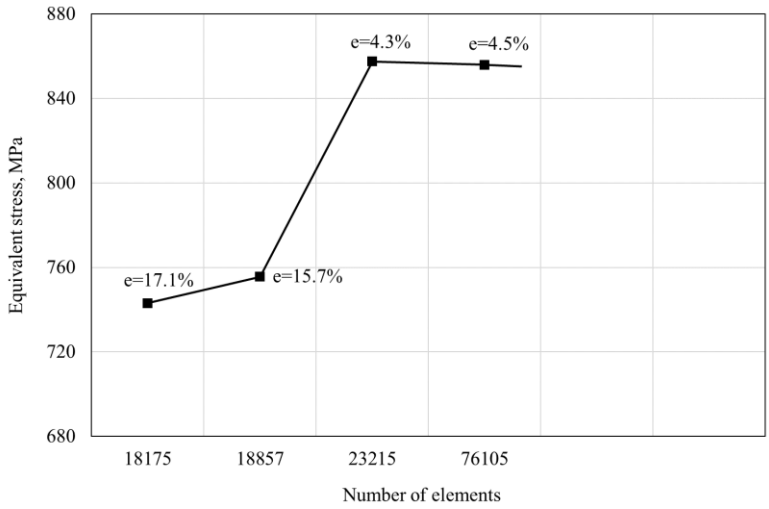

Fig.3 – Mesh convergence and error (e).

The obtained results from the total deformation, equivalent elastic strain, and equivalent stress for BKS allow us to conclude on the drilling parameters chosen for each BKS material. The results are shown for each different applied cutting torque on BKS and presented in different figures. Figs.4 to 9 represent the results for each material of the BKS, as a function of the applied cutting torque.

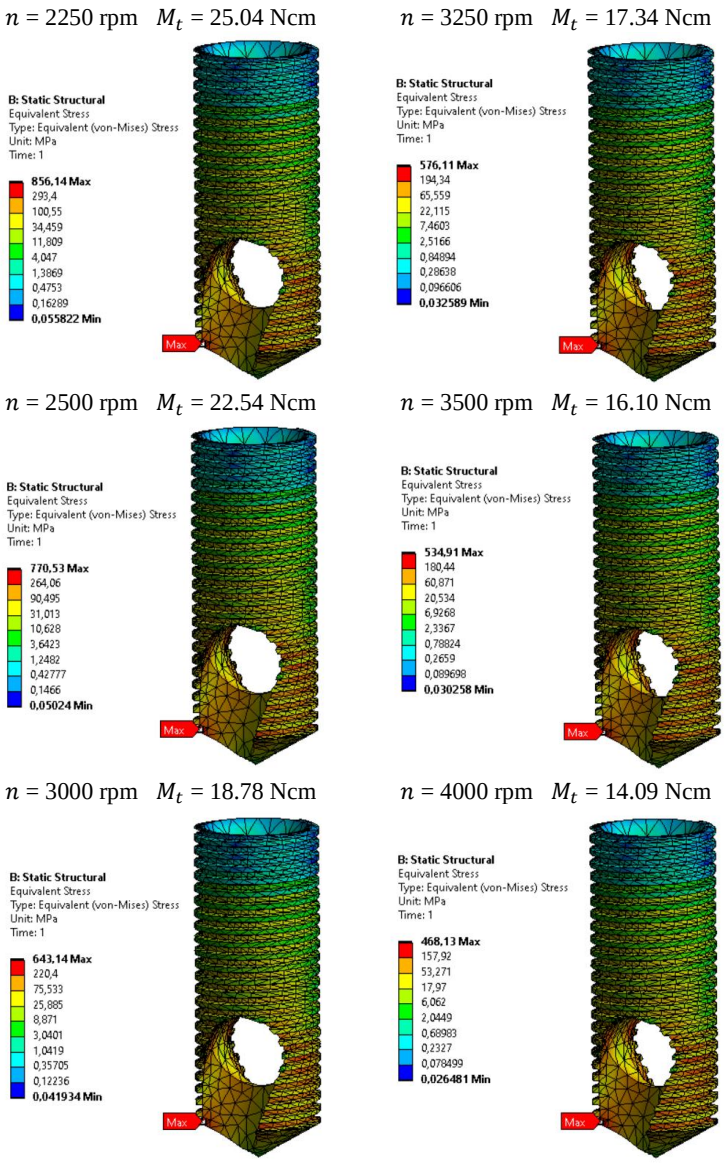

Fig.4 – Equivalent stress in BKS with two materials. (a) Ti6Al4V (Grade 5). (b) Cp-Ti (Grade 4).

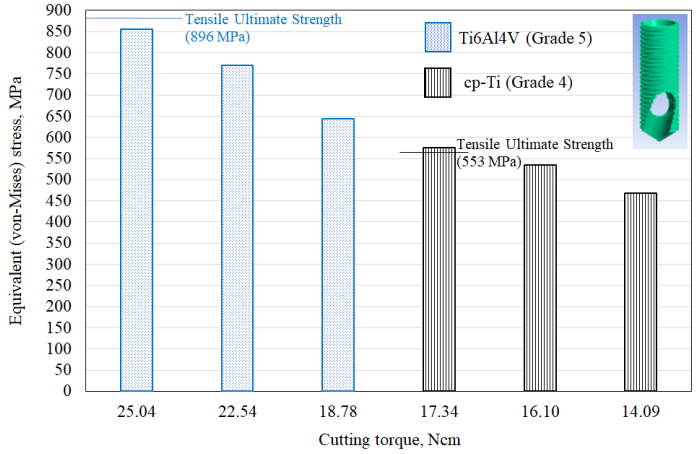

Fig.5 – Maximum value of equivalent stress in BKS model for all drilling parameters.

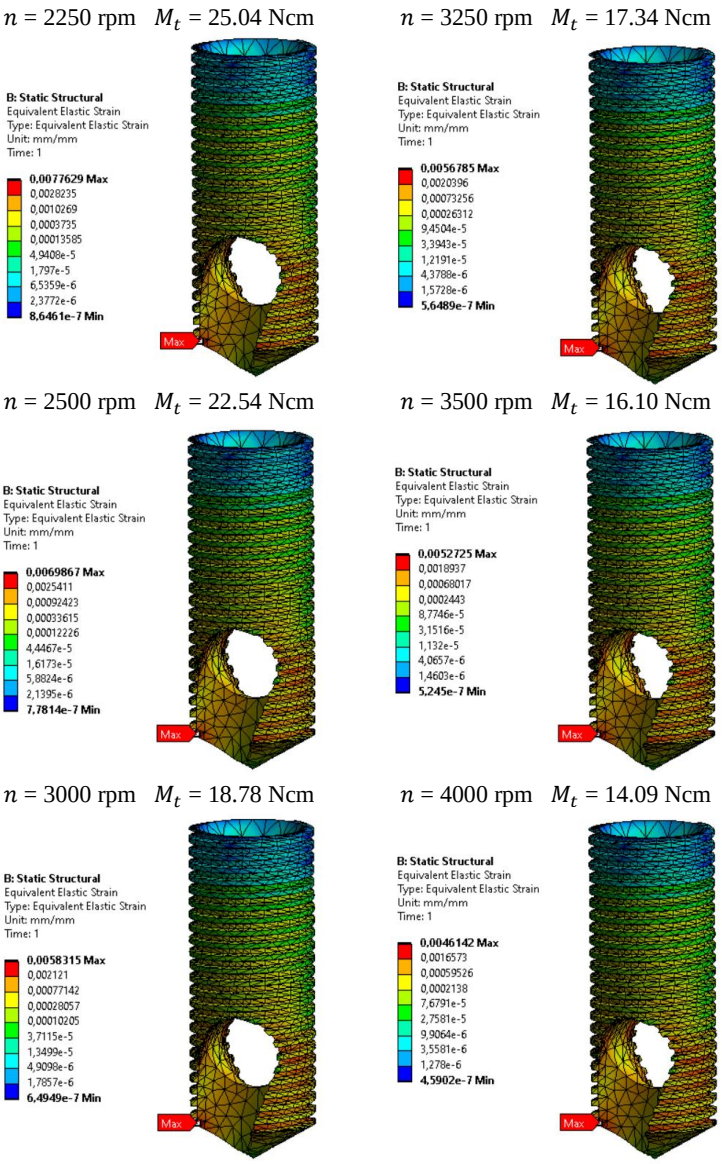

Fig.6 – Equivalent elastic strain in BKS with two materials. (a) Ti6Al4V (Grade 5). (b) Cp-Ti (Grade 4).

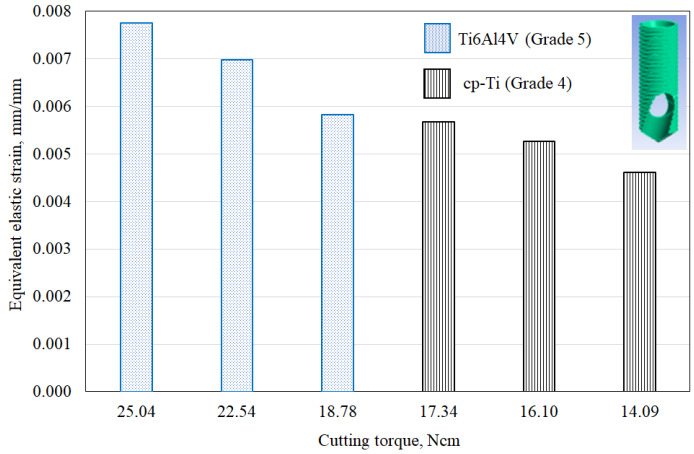

Fig.7 – Maximum value of equivalent elastic strain in BKS model for all drilling parameters.

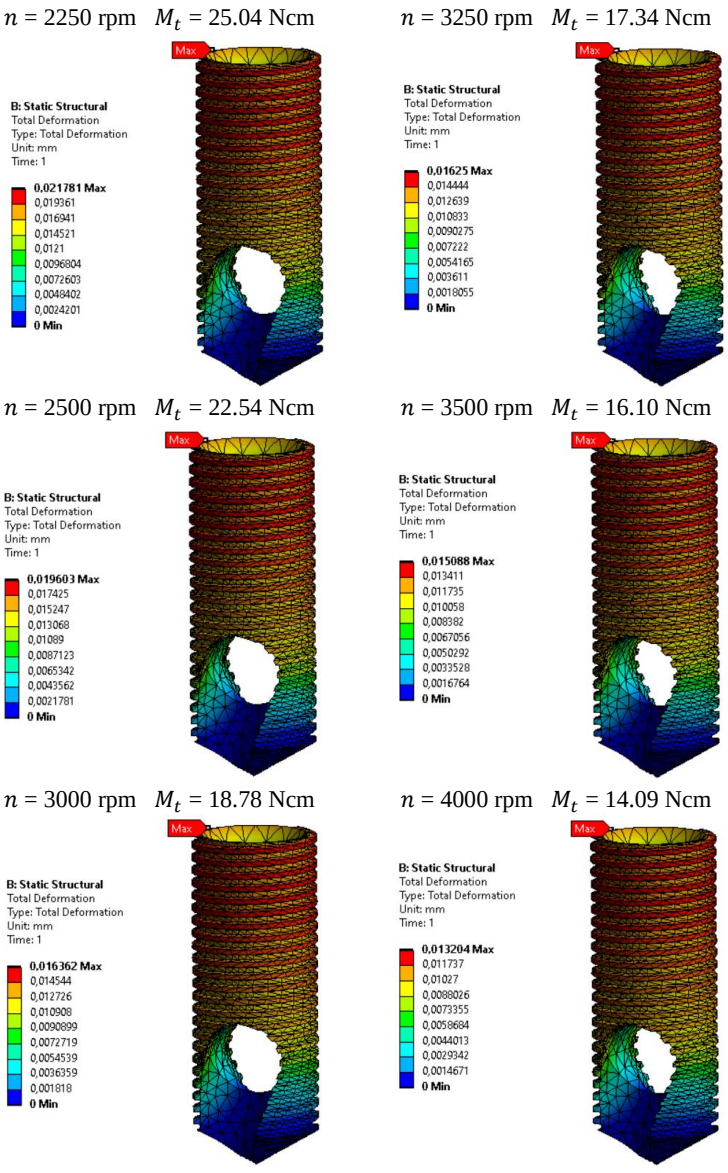

Fig.8 – Total deformation in BKS with two materials. (a) Ti6Al4V (Grade 5). (b) Cp-Ti (Grade 4).

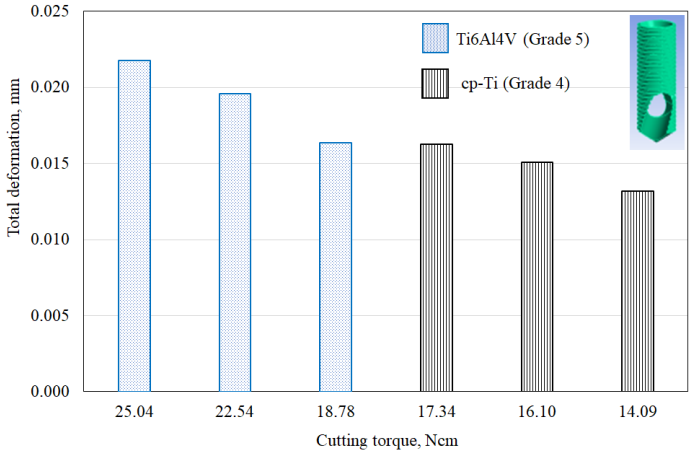

Fig.9 – Maximum value of total deformation in BKS model for all drilling parameters.

Numerical results show that stress, strain, and deformation levels tend to increase with lower BKS rotation or higher imposed cutting torque. At the tip of the screw, the BKS presents higher stress and strain. The deformation is closer to the imposed cutting torque. The equivalent elastic strain determines the level of equivalent stress in the BKS that can be transmitted to the drilling process in bone material.

The calculated strains and stresses vary along the entire length of the BKS, and this can be justified by the inertia of its cross-section, due to the existing space in the BKS mechanism. The inertia cross-section at the bottom decreases and the stress increases.

The maximum stress, strain and deformation values are verified when a cutting torque equal to 25.04 Ncm is applied, corresponding to the minimum rotational speed of 2250 rpm. Comparing the materials, the high level of stress, strain and deformation is produced when the BKS is Ti6Al4V material.

The BKS mechanism achieves greater deformation, stress and elastic strain for high cutting torques at low speed. The BKS in cp-Ti material presents the lower values of stress and strain, since that the material strength is lower than Ti6Al4V. The screw with less stress will allow for a longer tool life, as mentioned in the literature [21].

4. Conclusions

In the present study, numerical simulations were performed implementing a 3D FEM model. A total of 6 simulations were performed to study the effect of cutting torque and screw material on the drilling process. The BKS is in Ti6Al4V or cp-Ti material of 4 mm diameter. The drilling process uses different rotational speeds. The chosen drilling parameters were due to the obtained values for the ultimate tensile strength in the BKS for each material. This study can be used to avoid the difficulties that normally occur during the drilling process.

The described simulation demonstrates that the screw causing strains, stresses, and deformations during the imposed cutting torque, which can affect the bone. Based on the simulation results, the low cutting torque imposed on the BKS on cp-Ti material is recommended to obtain lower stress levels on the screw. The screw with lowest stress will have a longer tool life.

The BKS mechanism achieves higher stresses for high cutting torques at low speed and in Ti6Al4V material.

The new BKS presented for dental drilling presents a space in the mechanism that can be occupied by particulate bone, resulting in the accumulation of material removed inside the implant screw.

As future research, BKS can be analysed to improve its life cycle, more tests can be performed to estimate the maintenance time of BKS replacement, more tests can be performed to combine BKS in bone material and verify the interaction and accumulation of material inside the screw.

References

[1] Shivani DrLPS, Alok Y. Modelling & Analysis of Drill Bit with different Materials. International Research Journal of Engineering and Technology. 2019; 06(08):194-199.

[2] Necati U, Adem Ç, Ekrem O, Kubilay A. Finite element simulations of cutting force, torque, and temperature in drilling of Inconel 718. Procedia CIRP 82. 2019, 47-52. DOI:10.1016/j.procir.2019.03.277

[3] Strenkowski JS; Hsieh CC; Shih AJ. An analytical finite element technique for predicting thrust force and torque in drilling. International Journal of Machine Tools & Manufacture. 2004; 44:1413–1421. DOI:10.1016/j.ijmachtools.2004.01.005

[4] Fernandes MG; Fonseca EM; Natal RM. Three-dimensional dynamic finite element and experimental models for drilling processes. Proc IMechE Part L: Journal of Materials: Design and Applications. 2015; 232(1), 35-43. DOI:10.1177/1464420715609363

[5] Fernandes MG; Fonseca EM; Natal RM. R. Thermo-mechanical stresses distribution on bone drilling: numerical and experimental procedures. Proceedings of the Institution of Mechanical Engineers, Part L: Journal of Materials: Design and Applications. 2019; 233(4):637-646. DOI:10.1177/1464420716689337

[6] Fernandes MG; Fonseca EM; Natal RM, Dias MIR. Thermal analysis in drilling of ex vivo bovine bones. Journal of Mechanics in Medicine and Biology. 2017; 17(5):16 pages. DOI:10.1142/S0219519417500828

[7] Fernandes MG; Fonseca EM; Natal RM.; Manzanares MC. Ex vivo experimental and numerical study of stresses distribution in human cadaveric tibiae. International Journal of Medical Engineering and Informatics. 2021; 13(2):164-173. DOI:10.1504/IJMEI.2021.113396

[8] Hemesh P; Jeyakarthikeyan PV. Mesh convergence study and estimation of discretization error of hub in clutch disc with integration of ANSYS. IOP Conf. Series: Materials Science and Engineering 402. 2018. DOI:10.1088/1757-899X/402/1/012065

[9] Zhuming Bi. Chapter 8 Applications—Solid Mechanics Problems. Finite Element Analysis Applications. Elsevier. 2018. DOI:10.1016/B978-0-12-809952-0.00008-X

[10] Jianping G; Weiqi Y; Wei X. Application of the Finite Element Method in Implant Dentistry. Springer. 2008.

[11] Shah FA; Trobos M; Thomsen P; Palmquist A. Commercially pure titanium (cp-Ti) versus titanium alloy (Ti6Al4V) materials as bone anchored implants – Is one truly better that the other?. Materials Science and Engineering C. 2016; 62:960-966. DOI:10.1016/j.msec.2016.01.032
[12] Craig RG. Restorative Dental Materials. 2012, Edited by Ronald L. Sakaguchi, John M. Powers. Ed 13. Philadelphia.
[13] Lewinstein I, Banks-Sills L, Eliasi R. Finite element analysis of a new system (IL) for supporting an implant-retained cantilever prosthesis. The Journal of Prosthetic Dentistry. 1995, 10:355-366. DOI:10.1016/S0022-3913(96)90301-7.
[14] K. Alam R; Muhammad A; Shamsuzzoha A; AlYahmadia; Ahmed N. Quantitative Analysis of Force and Torque in Bone Drilling. The Journal of Engineering Research. 2017; 14(1):39-48. DOI:10.24200/tjer.vol14iss1pp39-48
[15] Mihali et al. Effects of a Short Drilling Implant Protocol on Osteotomy Site Temperature and Drill Torque. Implant Dentistry. 2017; 1-6. DOI:10.1097/ID.0000000000000707
[16] Sivolella S; De Biagi M; Brunello G; Ricci S; Tadic D; Marinc C; Lops D; Ferroni L; Gardin C; Bressan E; Barbara ZB. Delivery Systems and Role of Growth Factors for Alveolar Bone Regeneration in Dentistry. In: Regenerative Medicine and Tissue Engineering, chapter 28. INTECH. 2013; 713-742. DOI:10.5772/55580
[17] Jantunen E. A summary of methods applied to tool condition monitoring in drilling. International Journal of Machine Tools and Manufacture. 2002; 42(9): 997-1010. DOI:10.1016/S0890-6955(02)00040-8
[18] RMI Titanium Company. Titanium Alloy Guide. 2000; An RTI International Metals, Inc. Company
[19] ANSYS, Inc. (2020) ANSYS Mechanical APD 2020 R2, Release 2.
[20] Acceded 27 December 20212. Available from: https://www.wh.com/en_global/dental-products/restoration-prosthetics/electric-motor/em-12l/
[21] Swapnil C; Chaitanya VK; Bharat C; Nitin S. Design & Analysis of Stress on Drill Bit. Turkish Journal of Computer and Mathematics Education. 2021, 12(13):2243-2248.

Journal of Computation and Artificial Intelligence in Mechanics and Biomechanics ISSN 2184-8971
Volume 2, Issue 1, Page 44-54, 2022

Structural analysis of healthy and degenerated intervertebral discs using meshless methods

Rita Almeida [1], Jorge Belinha [2]

[1] *Rita Almeida, School of Engineering, Polytechnic of Porto (ISEP), Portugal, 1170461@isep.ipp.pt*
[2] *Jorge Belinha, Department of Mechanical Engineering, School of Engineering, Polytechnic of Porto (ISEP), Portugal, job@isep.ipp.pt*

Abstract
Intervertebral disc (IVD) degeneration is a progressive condition that modifies the geometric morphology, biomechanical behavior, and material properties of an IVD, affecting its ability to transmit and distribute loads. The aim of this work is to analyze the effects of applying different loads in different orientations both in healthy and degenerated IVDs. To perform the numerical analysis, a three-dimensional (3D) discretized model was constructed and analyzed with the radial point interpolation method (RPIM) and the finite element method (FEM). In order to simulate the IVD degeneration, the mechanical properties, height and applying loads were altered, allowing to represent six different study cases. With an elasto-static analysis, assuming small strains, the von Mises equivalent stress and principal stresses (σ_1 and σ_3) variable fields were obtained with both RPIM and FEM. Also, for a region of interest, the equivalent strain is also addressed. The results show that distinct IVD conditions lead to distinct stress/strain distributions. Additionally, the comparison between the RPIM and FEM solutions indicate that the RPIM provides variable fields with lower magnitude. Nevertheless, both technique provide similar variable field distributions.

***DOI**: 10.5281/zenodo.7406104*

Article Info

Keywords
Finite element method
Meshless methods
Biomechanics
Intervertebral disc

Article History
Received: *22/03/2022*
Revised: *12/07/2022*
Accepted: *23/09/2022*

1 Introduction

Over 80% of the adult population experiences low back pain (LBP) at some point in their lives, resulting in a vast amount of money in annual costs, to alleviate and treat this pain [1],[2]. Epidemiologic and biomechanical studies have shown that mechanical loads imposed on the human spine and, consequently, on the intervertebral disc (IVD), during daily life, play a significant role in this type of pain [2].

The IVDs are fibrocartilaginous, biconvex lens-shaped structures, which are interposed between the vertebral bodies of two adjacent vertebrae and are responsible for approximately 25% of the size of the spine [3]. The IVD is constituted by a soft, deformable, nucleus pulposus (NP) that is surrounded by the fibrous concentric layers of the anulus fibrosus (AF) [4],[5]. The NP and AF are comprised primarily of water, proteoglycans, and collagen fibers, in different rations between the two tissues [6]. They function as an additional load-absorption support that sustains high deformations, distributes the load, allows movement of the functional unit, and prevents friction between adjacent bodies [7],[4]. Throughout human life, a phenomenon called disc degeneration occurs, which is marked by changes in the disc morphology and biochemistry [8]. For example, when compared to a healthy disc, a degenerated one can have a 20% to 60% reduction of its height, depending on the degree of degeneration [9]. Upon disc degeneration, there is a reduction in the water content in the NP, which leads to changes in its mechanical properties. For this reason, it is possible to make a comparison between a hydrated disc, when it is healthy, and dehydrated, when it is degenerated [10],[11].

IVD pressure is an important parameter to characterize spinal overload in disc degeneration [12]–[14]. To analyze the effects of this degeneration in the IVD, several studies have already been caried out. In the 1960s and 1970s, the pioneering scientific work performed by Nachemson et al. [15] showed a relationship between body positions or exercises (unsupported sitting, lifting weights, etc.) and lumbar IVD pressure. In this study, Nachemson and colleagues showed that sitting increases the pressure in the IVD by approximately 40% when compared with standing position [15]. A few years ago, finite element method (FEM) analysis emerged as a promising solution to study IVD pressure and its relationship to healthy and degenerated IVDs. Cai et al. [9], proved, using a finite element study, that an increase in the IVD degeneration leads to higher von Mises stress and higher shear stress [9]. This fact was also proved by Rohlmann et al. [16], that also used finite element method. More FEM studies focusing on the IVD have been carried out over the years [10].

Corresponding Author:
Jorge Belinha
job@isep.ipp.pt

A few years later, the computational mechanics' scientific community started to focus their attention on other advanced discretization techniques, such as the meshless methods. In this work, a meshless method is used to perform the structural analysis of the IVD and obtain the corresponding variable fields – the radial point interpolation method (RPIM). The RPIM emerged as a promising technique due to its sensitivity to the element's distortion [17]. The RPIM has been successfully applied to 1D and 2D solid mechanics, plate and shell structures, problems of smart materials, geometrically non-linear problems, material non-linear problems in civil engineering [18], and biomechanics related topics, such as the simulation of human chromosomes [19] or even a 2D stress analysis of zirconia dental implants [20].

In the present work, an analysis of the pressure in the IVD will be performed through the use of both RPIM and FEM, in order to study the effect of the pressure exerted by the vertebrae when applied in certain positions and when the mechanical properties of the disc are varied.

2. Meshless Methods and Model Discretization

2.1. RPIM formulation

Due to continuous advances in numerical techniques and computational technology, FEM is able to simulate several distinct scenarios in a realistic way [8]. Despite the good results obtained using FEM, there are some mesh-related problems that can be minimized if a meshless approach is considered [21]. In opposition to FEM, in the meshless methods the nodes can be arbitrary distributed, since the field functions are approximated within an influence-domain rather than an element. Throughout the years, several interpolation meshless methods were developed, and one of the most relevant is the RPIM [22]. By meshless methods, models can be built using only nodes, without the need of a pre-established mesh. This makes meshless methods very effective in modeling large deformations, mesh-transient problems and fracture problems, especially for highly heterogeneous materials [21].

The RPIM constructs its shape functions using the radial point interpolator technique [22]. Thus, the variable field $h(\boldsymbol{x}_I)$ of an integration point $\boldsymbol{x}_I$ can be interpolated with the following expression:

$$h(\boldsymbol{x}_I) = \sum_{i=1}^{n} r_i(\boldsymbol{x}_I) \cdot a_i + \sum_{j=1}^{m} p_j(\boldsymbol{x}_I) \cdot b_j = \boldsymbol{r}(\boldsymbol{x}_I)^T \cdot \boldsymbol{a} + \boldsymbol{p}(\boldsymbol{x}_I)^T \cdot \boldsymbol{b} \tag{1}$$

In which, n represents the number of nodes inside the influence-domain of $\boldsymbol{x}_I$, m is the number of monomial of the polynomial basis functions $\boldsymbol{p}(\boldsymbol{x}_I)$, respectively. The radial basis functions (RBF) is represented by $\boldsymbol{r}(\boldsymbol{x}_I)$ and $\boldsymbol{a}$ and $\boldsymbol{b}$ are the non-constant coefficients of $\boldsymbol{r}(\boldsymbol{x}_I)$ and $\boldsymbol{p}(\boldsymbol{x}_I)$, respectevly: $\boldsymbol{a} = \{a_1 \quad \cdots \quad a_n\}^T$ and $\boldsymbol{b} = \{b_1 \quad \cdots \quad b_m\}^T$. The RBF used in this work is the Multi-Quadrics RBF (MQ-RBF), which can be represented as,

$$r_i(\boldsymbol{x}_I) = r(d_{iI}) = (d_{iI}^2 + c^2)^p \tag{2}$$

Being, d_{iI} the Euclidean norm between node $\boldsymbol{x}_i$ and the integration point $\boldsymbol{x}_I$:

$$d_{iI} = \sqrt{(x_i - x_I)^2 + (y_i - y_I)^2 + (z_i - z_I)^2} \tag{3}$$

and c and p the MQ-RBF shape parameters, already optimized for elasto-static problems in previous works: $p = 0.9999$ and $c = 0.0001$ [22]. In this work, a constant polynomial basis functions is used. Thus, $\boldsymbol{P}(\boldsymbol{x}_I) = \{1\}$ and $m = 1$.

To construct the RPI function of integration point $\boldsymbol{x}_I$, it is necessary to apply Eq. (1) to each k node inside the influence-domain of $\boldsymbol{x}_I$.

$$h(\boldsymbol{x}_k) = \sum_{i=1}^{n} r_i(\boldsymbol{x}_k) \cdot a_i + \sum_{j=1}^{m} p_j(\boldsymbol{x}_k) \cdot b_j = h_k, \quad k = 1,2,\ldots,n \tag{4}$$

Notice that h_k is the nodal variable value. To ensure a unique solution, the following equation must be included in the interpolating system of equations [22]:

$$\sum_{i=1}^{n} p_j(\boldsymbol{x}_i) \cdot a_i = 0, \quad j = 1,2,\ldots,m \tag{5}$$

Allowing to write the following system of equations,

$$\begin{bmatrix} \boldsymbol{R} & \boldsymbol{P} \\ \boldsymbol{P^T} & 0 \end{bmatrix} \begin{Bmatrix} \boldsymbol{a} \\ b \end{Bmatrix} = \begin{Bmatrix} \boldsymbol{h} \\ 0 \end{Bmatrix} \Leftrightarrow \boldsymbol{G} \begin{Bmatrix} \boldsymbol{a} \\ b \end{Bmatrix} = \begin{Bmatrix} \boldsymbol{h} \\ 0 \end{Bmatrix} \tag{6}$$

Being $\boldsymbol{G}$ the moment matrix. Matrices $\boldsymbol{R}$ and $\boldsymbol{P}$ and vector $\boldsymbol{h}$ are defined as,

$$\boldsymbol{R}_{[n\times n]} = \begin{bmatrix} R(r_{11}) & R(r_{12}) & \ldots & R(r_{1n}) \\ R(r_{21}) & R(r_{22}) & \ldots & R(r_{2n}) \\ \vdots & \vdots & \ddots & \vdots \\ R(r_{n1}) & R(r_{n2}) & \ldots & R(r_{nn}) \end{bmatrix}; \ \boldsymbol{P}_{[n\times 1]} = \begin{bmatrix} 1 \\ 1 \\ \vdots \\ 1 \end{bmatrix}; \ \boldsymbol{h}_{[n\times 1]} = \begin{bmatrix} h_1 \\ h_2 \\ \vdots \\ h_n \end{bmatrix} \tag{7}$$

Solving Eq. (6) it is possible to obtain the non-constant coefficients:

$$\begin{Bmatrix} \boldsymbol{a} \\ b \end{Bmatrix} = \boldsymbol{G}^{-1} \begin{Bmatrix} \boldsymbol{h} \\ 0 \end{Bmatrix} \tag{8}$$

To assure that $\boldsymbol{G}$ is invertible, it is necessary that m ≤ n. Since in this work, the number of nodes inside the influence domain is always much higher than the number of polynomial terms of the polynomial basis $\boldsymbol{p}$, ($m = 1$), this condition is always largely satisfied. Substituting $\boldsymbol{a}$ and b, into Eq. (1), the shape functions vector $\phi(\boldsymbol{x}_I)$ of the integration point $\boldsymbol{x}_I$ is obtained:

$$h(\boldsymbol{x}_I) = \{\boldsymbol{r}(\boldsymbol{x}_I)^T; \boldsymbol{p}(\boldsymbol{x}_I)^T\}\boldsymbol{G}^{-1} \begin{Bmatrix} \boldsymbol{h} \\ 0 \end{Bmatrix} = \{\boldsymbol{\phi}(\boldsymbol{x}_I)^T; \ \boldsymbol{\psi}(\boldsymbol{x}_I)^T\} \begin{Bmatrix} \boldsymbol{h} \\ 0 \end{Bmatrix} \tag{9}$$

being $\boldsymbol{\phi}(\boldsymbol{x}_I) = \{\boldsymbol{\phi}_1(\boldsymbol{x}_I), \boldsymbol{\phi}_2(\boldsymbol{x}_I), \ldots, \boldsymbol{\phi}_n(\boldsymbol{x}_I)\}$ and the residual, $\boldsymbol{\psi}(\boldsymbol{x}_I)$, defined by $\boldsymbol{\psi}(x_I) = \{\psi_I(x_I)\}$. The RPI shape functions possess the delta Kronecker property, which allows to exactly impose the essential and natural boundary conditions using penalty techniques, and possess compact support, leading to banded system of equations. Details on the construction of RPI shape functions and corresponding numerical properties can be found in the literature [22].

2.2. Elasto-static system of equations

After discretizing the problem domain and determining the shape functions, the equilibrium equations based on the principle of virtual displacements can be developed,

$$\int_\Omega \delta\boldsymbol{\varepsilon}^T \boldsymbol{\sigma} \, d\Omega - \int_\Omega \delta\boldsymbol{u}^T \boldsymbol{b} \, d\Omega - \int_\Omega \delta\boldsymbol{u}^T \bar{\boldsymbol{t}} \, d\Gamma_t = 0 \tag{10}$$

where Ω represents the domain of the problem and Γ_t the traction boundary. The strain vector is defined with $\boldsymbol{\varepsilon}$ and the stress vector with $\boldsymbol{\sigma}$. The displacement fields is represented with, $\boldsymbol{u}$, the body force vector as $\boldsymbol{b}$ and $\bar{\boldsymbol{t}}$ is the traction vector representing the external force applied on the natural boundary. Using the generalized Hooke's law, the relation between $\boldsymbol{\varepsilon}$ and $\boldsymbol{\sigma}$ can be established,

$$\boldsymbol{\varepsilon}(\boldsymbol{x}_I) = \boldsymbol{L}\boldsymbol{u}(\boldsymbol{x}_I) \Leftrightarrow \begin{Bmatrix} \varepsilon_{xx}(\boldsymbol{x}_I) \\ \varepsilon_{yy}(\boldsymbol{x}_I) \\ \varepsilon_{zz}(\boldsymbol{x}_I) \\ \gamma_{xy}(\boldsymbol{x}_I) \\ \gamma_{yz}(\boldsymbol{x}_I) \\ \gamma_{zx}(\boldsymbol{x}_I) \end{Bmatrix} = \begin{bmatrix} \frac{d}{dx} & 0 & 0 \\ 0 & \frac{d}{dy} & 0 \\ 0 & 0 & \frac{d}{dz} \\ \frac{d}{dy} & \frac{d}{dx} & 0 \\ 0 & \frac{d}{dz} & \frac{d}{dy} \\ \frac{d}{dz} & 0 & \frac{d}{dx} \end{bmatrix} \begin{Bmatrix} u(\boldsymbol{x}_I) \\ v(\boldsymbol{x}_I) \\ w(\boldsymbol{x}_I) \end{Bmatrix} \tag{11}$$

and then,

$$\boldsymbol{\sigma}(\boldsymbol{x}_I) = \boldsymbol{c} \cdot \boldsymbol{\varepsilon} \Leftrightarrow \begin{Bmatrix} \varepsilon_{xx}(\boldsymbol{x}_I) \\ \varepsilon_{yy}(\boldsymbol{x}_I) \\ \varepsilon_{zz}(\boldsymbol{x}_I) \\ \gamma_{xy}(\boldsymbol{x}_I) \\ \gamma_{yz}(\boldsymbol{x}_I) \\ \gamma_{zx}(\boldsymbol{x}_I) \end{Bmatrix} = \begin{bmatrix} \frac{1}{E} & -\frac{\upsilon}{E} & -\frac{\upsilon}{E} & 0 & 0 & 0 \\ -\frac{\upsilon}{E} & \frac{1}{E} & -\frac{\upsilon}{E} & 0 & 0 & 0 \\ -\frac{\upsilon}{E} & -\frac{\upsilon}{E} & \frac{1}{E} & 0 & 0 & 0 \\ 0 & 0 & 0 & \frac{1}{G} & 0 & 0 \\ 0 & 0 & 0 & 0 & \frac{1}{G} & 0 \\ 0 & 0 & 0 & 0 & 0 & \frac{1}{G} \end{bmatrix}^{-1} \cdot \begin{Bmatrix} \varepsilon_{xx}(\boldsymbol{x}_I) \\ \varepsilon_{yy}(\boldsymbol{x}_I) \\ \varepsilon_{zz}(\boldsymbol{x}_I) \\ \gamma_{xy}(\boldsymbol{x}_I) \\ \gamma_{yz}(\boldsymbol{x}_I) \\ \gamma_{zx}(\boldsymbol{x}_I) \end{Bmatrix} \tag{12}$$

being E the Young's modulus, υ the Poisson's coefficient and G the shear modulus, $G = E/(2\upsilon + 2)$. Thus, the first term of Eq.(8) is as follows:

$$\int_\Omega \delta\boldsymbol{\varepsilon}^T \boldsymbol{\sigma}\, d\Omega = \int_\Omega (\delta\boldsymbol{L}\boldsymbol{u})^T \boldsymbol{c}(\boldsymbol{L}\boldsymbol{u})\, d\Omega \tag{13}$$

The RPIM permits to interpolate nodal data to integration points $(\boldsymbol{x}_I)$ using the shape functions of $(\boldsymbol{x}_I)$, allowing to define the virtual displacement $\delta\boldsymbol{u}(\boldsymbol{x}_I)$ with the interpolation function, $\boldsymbol{\phi}(\boldsymbol{x}_i)$,

$$\delta\boldsymbol{u}(\boldsymbol{x}_I) = \delta\boldsymbol{u}_I = \begin{bmatrix} \phi_1(\boldsymbol{x}_I) & 0 & 0 & \cdots & \phi_n(\boldsymbol{x}_I) & 0 & 0 \\ 0 & \phi_1(\boldsymbol{x}_I) & 0 & \cdots & 0 & \phi_n(\boldsymbol{x}_I) & 0 \\ 0 & 0 & \phi_1(\boldsymbol{x}_I) & \cdots & 0 & 0 & \phi_n(\boldsymbol{x}_I) \end{bmatrix} \begin{Bmatrix} \delta u_1 \\ \delta v_1 \\ \delta w_1 \\ \vdots \\ \delta u_n \\ \delta v_n \\ \delta w_n \end{Bmatrix} = \boldsymbol{H}_I \delta\boldsymbol{u} \tag{14}$$

Notice that in a 3D analysis, each node $\boldsymbol{x}_i$ possesses three degrees of freedom: $\boldsymbol{u}_i = \{u_i, v_i, w_i\}^T$. Assuming $\boldsymbol{L} \cdot \boldsymbol{H}_I = \boldsymbol{B}_I$, Eq.(11) becomes,

$$\int_\Omega (\delta\boldsymbol{L}\boldsymbol{u})^T \boldsymbol{c}(\boldsymbol{L}\boldsymbol{u})\, d\Omega = \int_\Omega (\boldsymbol{L}\boldsymbol{H}_I\delta\boldsymbol{u})^T \boldsymbol{c}(\boldsymbol{L}\boldsymbol{H}_I\boldsymbol{u})\, d\Omega = \int_\Omega \delta(\boldsymbol{B}_I\boldsymbol{u})^T \boldsymbol{c}(\boldsymbol{B}_I\boldsymbol{u})\, d\Omega = \delta\boldsymbol{u}^T \int_\Omega \boldsymbol{B}_I^T \boldsymbol{c}\boldsymbol{B}_I\boldsymbol{u}\, d\Omega \tag{15}$$

where $\boldsymbol{B}_I$ is the deformability matrix of the interest point $\boldsymbol{x}_I$ and can be written as,

$$\boldsymbol{B}_I = \begin{bmatrix} \frac{d\phi_1(\boldsymbol{x}_I)}{dx} & 0 & 0 & \cdots & \frac{d\phi_n(\boldsymbol{x}_I)}{dx} & 0 & 0 \\ 0 & \frac{d\phi_1(\boldsymbol{x}_I)}{dy} & 0 & \cdots & 0 & \frac{d\phi_n(\boldsymbol{x}_I)}{dy} & 0 \\ 0 & 0 & \frac{d\phi_1(\boldsymbol{x}_I)}{dz} & \cdots & 0 & 0 & \frac{d\phi_n(\boldsymbol{x}_I)}{dz} \\ \frac{d\phi_1(\boldsymbol{x}_I)}{dy} & \frac{d\phi_1(\boldsymbol{x}_I)}{dx} & 0 & \cdots & \frac{d\phi_n(\boldsymbol{x}_I)}{dy} & \frac{d\phi_n(\boldsymbol{x}_I)}{dx} & 0 \\ 0 & \frac{d\phi_1(\boldsymbol{x}_I)}{dz} & \frac{d\phi_1(\boldsymbol{x}_I)}{dy} & \cdots & 0 & \frac{d\phi_n(\boldsymbol{x}_I)}{dz} & \frac{d\phi_n(\boldsymbol{x}_I)}{dy} \\ \frac{d\phi_1(\boldsymbol{x}_I)}{dz} & 0 & \frac{d\phi_1(\boldsymbol{x}_I)}{dx} & \cdots & \frac{d\phi_n(\boldsymbol{x}_I)}{dz} & 0 & \frac{d\phi_n(\boldsymbol{x}_I)}{dx} \end{bmatrix} \tag{16}$$

It is possible to discretize the integral of Eq. (13) by dividing the volume domain, Ω, into several subdomains, Ω_I, which corresponds to the physical volume occupied by each integration point, $\boldsymbol{x}_I$. The volume of such a subdomain is represented by the integration weight, $\widehat{\omega}_I$, of the corresponding integration point, $\boldsymbol{x}_I$. Thus, the discretized version of Eq. (13) can written as,

$$\delta \boldsymbol{u}^T \int_{\Omega} \boldsymbol{B}_I^{\boldsymbol{T}} \boldsymbol{c} \boldsymbol{B}_I \boldsymbol{u}\, d\Omega = \delta \boldsymbol{u}^T \sum_{I=1}^{N_Q} \left[\widehat{\omega}_I \boldsymbol{B}_I^{\boldsymbol{T}} \boldsymbol{c} \boldsymbol{B}_I\right] \boldsymbol{u} = \delta \boldsymbol{u}^T \sum_{I=1}^{N_Q} [\boldsymbol{K}_I] \boldsymbol{u} = \delta \boldsymbol{u}^T \boldsymbol{K} \boldsymbol{u} \tag{17}$$

where N_Q represents the total number of integration points. The local stiffness matrix $\boldsymbol{K}_I$ is then assembled into the global stiffness matrix, $\boldsymbol{K}$. Regarding the second and third terms of Eq. (10), the body volume forces are neglected, so only the third term is developed,

$$\int_{\Gamma_t} \delta \boldsymbol{u}^T \bar{\boldsymbol{t}}\, d\Gamma_t = \delta \boldsymbol{u}^T \int_{\Gamma_t} \boldsymbol{H}^T \bar{\boldsymbol{t}}\, d\Gamma_t = \delta \boldsymbol{u}^T \sum_{I=1}^{N_Q^*} \left[\widehat{\omega}_I \boldsymbol{H}_I^{\boldsymbol{T}} \bar{\boldsymbol{t}}\right] = \delta \boldsymbol{u}^T \sum_{I=1}^{N_Q^*} [\boldsymbol{f}_I] = \delta \boldsymbol{u}^T \boldsymbol{f} \tag{18}$$

where N_Q^* represents the number of integration points along the natural boundary. Thus, substituting Eq. (17) and (18) into Eq. (10), it is possible to establish the final discrete system of equations,

$$\delta \boldsymbol{u}^T \boldsymbol{K} \boldsymbol{u} - \delta \boldsymbol{u}^T \boldsymbol{f} = 0 \implies \boldsymbol{K} \boldsymbol{u} = \boldsymbol{f} \tag{19}$$

and then obtain the displacement field, $\boldsymbol{u} = \boldsymbol{K}^{-1} \boldsymbol{f}$.

2.3. Model construction

To obtain the IVD computational model, an anonymized CT image was used to perform the manual segmentation in the 3D Slicer® software, and obtain a IVD representation, in the STL format, as shown in Fig.1(a). This STL file is then opened in Meshmixer® software where possible mesh problems, such as holes and ill-conditioned triangles, are eliminated; the surface mesh of the STL is smoothed and significantly reduced (by decreasing the vertices and number of surface triangles), obtaining the representation presented in Fig.1(b), with 819 vertices and 1634 triangles. It should be noted that, at this stage, only a triangular surface mesh was obtained, and it is necessary to discretize the problem domain using solid elements, such as tetrahedral elements, so that a 3D analysis is allowed. For this, the FEMAP® student version software is used, and an IVD representation was obtained, as shown in Fig.1(c), with 1501 nodes and 6306 elements. This file was saved in INP format, so that it can be imported into the academic meshless software FEMAS® (cmech.webs.com), where the pressure analysis will be performed, more specifically at the points marked in red in Fig.1(d).

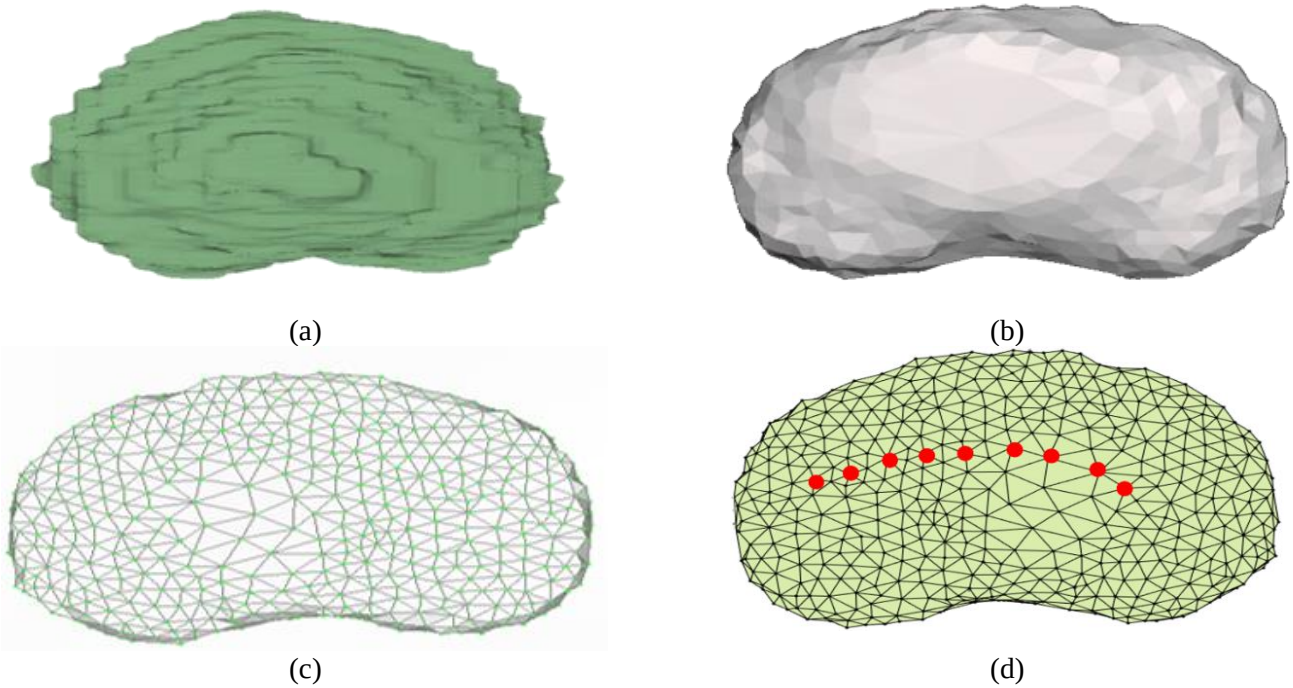

Fig.1 - IVD model (a) after manual segmentation in Slicer® software; (b) after smoothing and correcting errors in Meshmixer® software; (c) after application of tetrahedral mesh in FEMAP® software; (d) Region of interest for the analysis.

The materials and their properties were defined in the FEMAS® software. The model consists of two types of materials, corresponding to the NP and the AF. As previously mentioned, when a IVD degenerates, its composition changes, leading to a change in the mechanical properties [10],[11]. Table 1 shows the different mechanical properties for a healthy IVD, identified as hydrated (Case A), and for a degenerated IVD (Case B), identified as dehydrated. Based on the literature, both Young's modulus (E) and Poisson's coefficient (υ) were defined [11], [23], [24]. Throughout this analysis, it was assumed that the IVD model presents isotropic, homogeneous characteristics and linear elastic behavior.

Table 1 - Mechanical properties of the IVD materials.

	Hydrated (Case A)		Dehydrated (Case B)	
	E (MPa)	υ	E (MPa)	υ
NP	1.00	0.49	1.66	0.40
AF	2.56	0.40	12.29	0.35

In order to estimate the value of E for the simulations, it was necessary to understand that the NP accounts for 40%-50% of the volume of the adult IVD [5]. Considering that NP represents 50% of the volume, it is subsequently possible to assume that AF represents the other 50%. Thus, using the volume fraction concept, it is possible to estimate the homogenized Young's moduli of both healthy and degenerated IVDs cases.

$$E = \frac{E_{NP} \cdot V_{NP} + E_{AF} \cdot V_{AF}}{V_{NP} + V_{AF}} \tag{20}$$

Being E_i the Young's modulus of material i, and V_i the corresponding volume fraction. Regarding υ, it is possible to say that the value that was used results from the average of the NP and AF values, in both healthy and degenerated IVDs.

2.4. Model construction

After establishing the mechanical properties, it is necessary to define the essential and natural boundary conditions (Fig.(2)). The first ones are the restrictions applied to the inferior part of the IVD so that it does not move freely. In this particular case, no displacement was allowed in any direction, as shown in Fig.2(a).

The natural boundary conditions concern the forces that are applied to the superior part of the IVD, for the different cases studied. The first load case, Fig.2(b), concerns a normal pressure applied along Oz axis on the top of the IVD. The second load case, Fig.2(c), corresponds to a force applied with a 45º angle with respect to the IVD plane, simulating a tilted movement to the side. The third load case, Fig.2(d), simulates a pure shear solicitation, by applying a force contained in the IVD plane. It should be mentioned that, in all cases, it was assumed a straight sitting position, actively straightening the back.

Regarding the load magnitudes, previous works address such matter, such as the work of Wilke et al. [25]. Thus, for the body position mentioned before, the pressure applied to an area of 1800 mm2, is approximately 0.55 MPa. Thus, knowing the area of the natural boundary of load case 1 ($A = 500mm^2$), it is possible to estimate the total force applied to the IVD: $F = p \cdot A = 0.55 \cdot 500 = 275N$. All load cases possess the same force magnitude, only the force direction is modified.

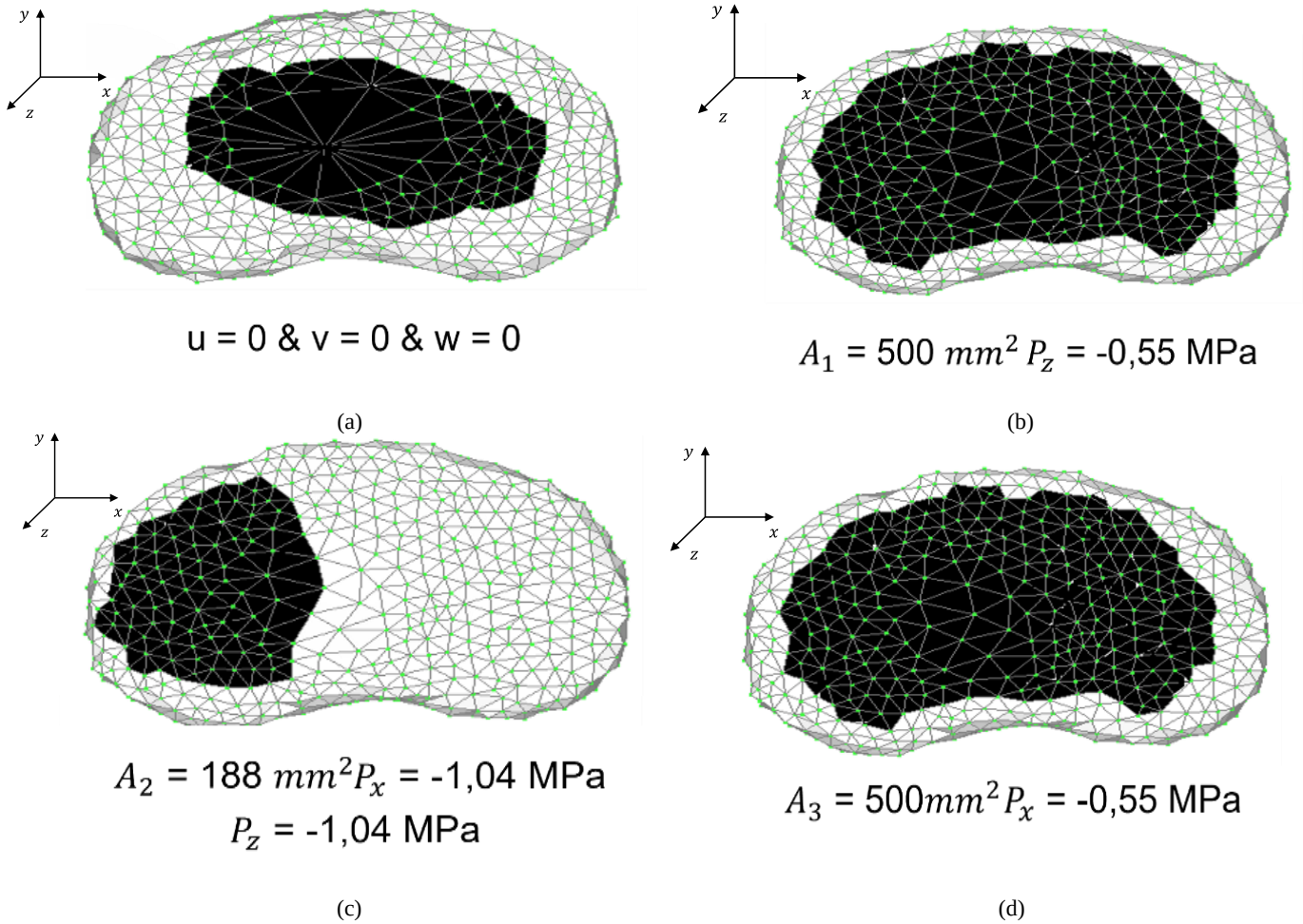

Fig.2 – (a) constrained boundary; (b) load case 1; (c) load case 2; (d) load case 3.

3. Results

After the RPIM and FEM analysis, displacements, stress and strain fields are obtained. In this section, the results obtained are presented. In Fig.3 and Fig.4 are presented the colored maps of the effective distribution of von Mises stresses, for a healthy IVD and degenerated IVD, respectively, when different loads are applied, as described before.

The von Mises equivalent stress (σ_{ef}) and equivalent strain (ε_{eq}), both acquired along the interest region depicted in Fig.1(d), are shown in Fig.5, respectively.

Table 2 shows the different values of σ_1 and σ_3, representing the maximum tensile and compressive stress in the model, correspondingly. Besides that, it is also possible to observe information regarding the average value of each

principal stress (σ_1 and σ_3). Principal stresses are presented due to its importance in biotissues. For instances in the IVD, the fibers oriented respecting the principal stress directions.

Table 2 – Principal stress $\sigma 1$, $\sigma 3$ $[MPa]$ and correspondent average values, $\bar{\sigma}_1$ *and* $\bar{\sigma}_3$ [MPa] for the six different study cases.

	A1	A2	A3	B1	B2	B3
σ_1	0.4303	2.7703	4.8263	1.478	4.7996	5.278
σ_3	-3.8462	-8.096	-4.8449	-5.4609	-12.7272	-3.9345
$\bar{\sigma}_1$	0.0555	0.3628	0.3615	0.1661	0.5378	-0.4068
$\bar{\sigma}_3$	-0.367	-0.346	-0.421	-0.458	-0.4068	-0.4638

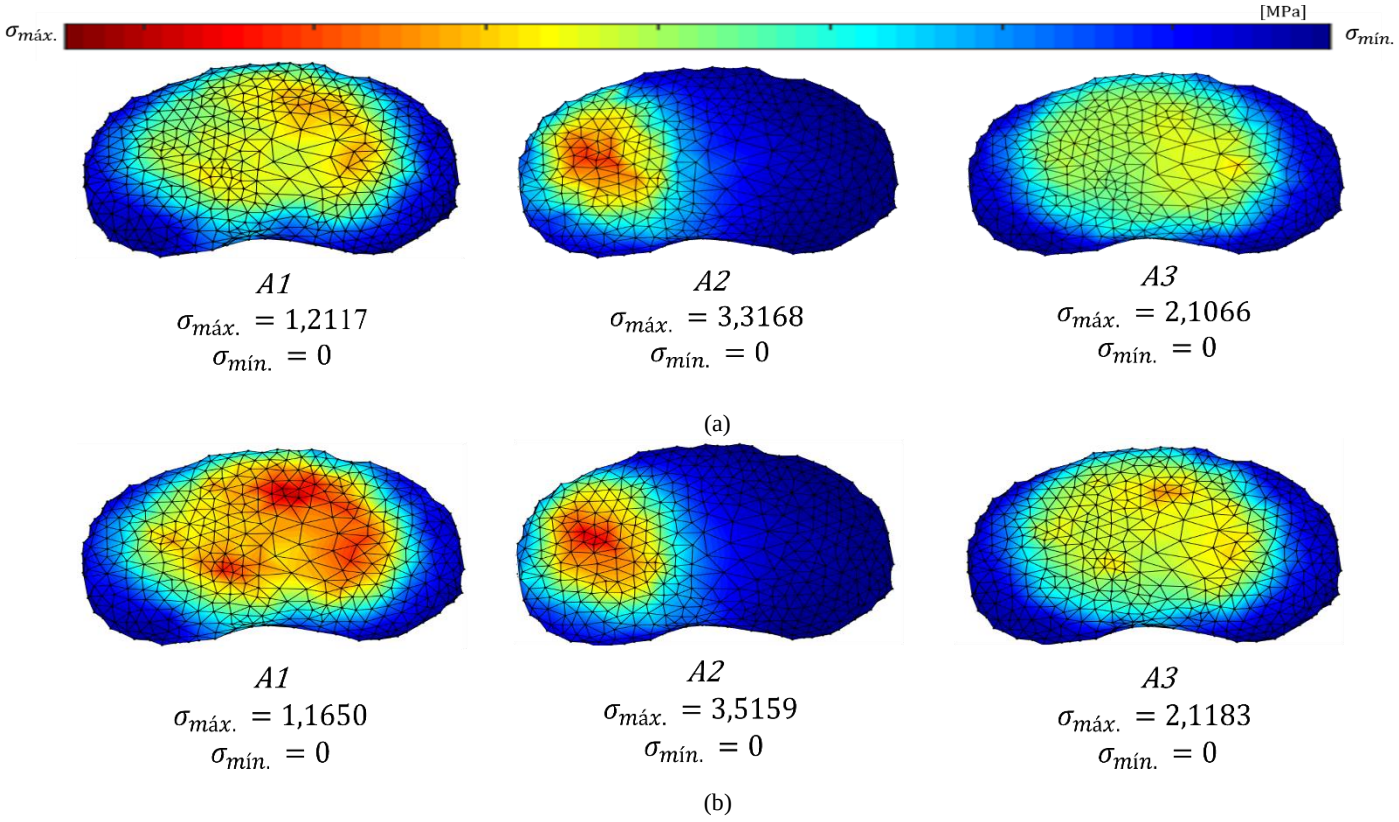

Fig.3 – Colored maps of the effective distribution of von Mises stresses (MPa) for healthy IVD (A) in 3 different load cases(1, 2 and 3) for (a) FEM analysis; (b) RPIM analysis.

4. Discussion

The main goal of this work was to develop an IVD model, using several softwares, to perform an elasto-static meshless analysis. Additionally, two IVD conditions were assumed, aiming to understand the impact of the material properties on the stress and strain variable fields. In order to validate the meshless analysis, the models were also analyzed using the well-known, and extensively validated, FEM.

Taking into consideration the results presented in Fig.(3), it is possible to assume that the higher von Mises stress are obtained for a degenerated IVD when a person is tilted to the side (case B2), for FEM and RPIM analyzes, with 5.987 MPa and 3.914 MPa, respectively. By contrast, smaller values for the von Misses stress were obtained for a healthy IVD when the pressure is exerted on the entire superior part of the IVD, for both FEM and RPIM analyzes, with 1.212 MPa and 1.165 MPa, respectively. It is possible to conclude that a degenerated IVD presents higher stress values than a healthy IVD, as it was showed in the study performed by Cai et al. [9], Park et al. [26] and Rohlmann et al. [16].

Through the analysis of Fig.(4), it is possible to conclude that when the stresses in cases A and B are compared, both from the FEM and from the RPIM analysis, they are equivalent, but the same does not happen with strains.

Analyzing Fig.(5), it is possible to observe that the maximum tensile stress is obtained for a degenerated IVD when a shear force is applied (B3). Also, the minimum compressive stress is obtained for a degenerated IVD, but this time when a tilted movement to the side occurs (B2). Besides that, it is also possible to visualize that the maximum average value for $\sigma 1$ was 0.538 MPa (B2) and the minimum value for $\sigma 3$ was -0.464 MPa (B3).

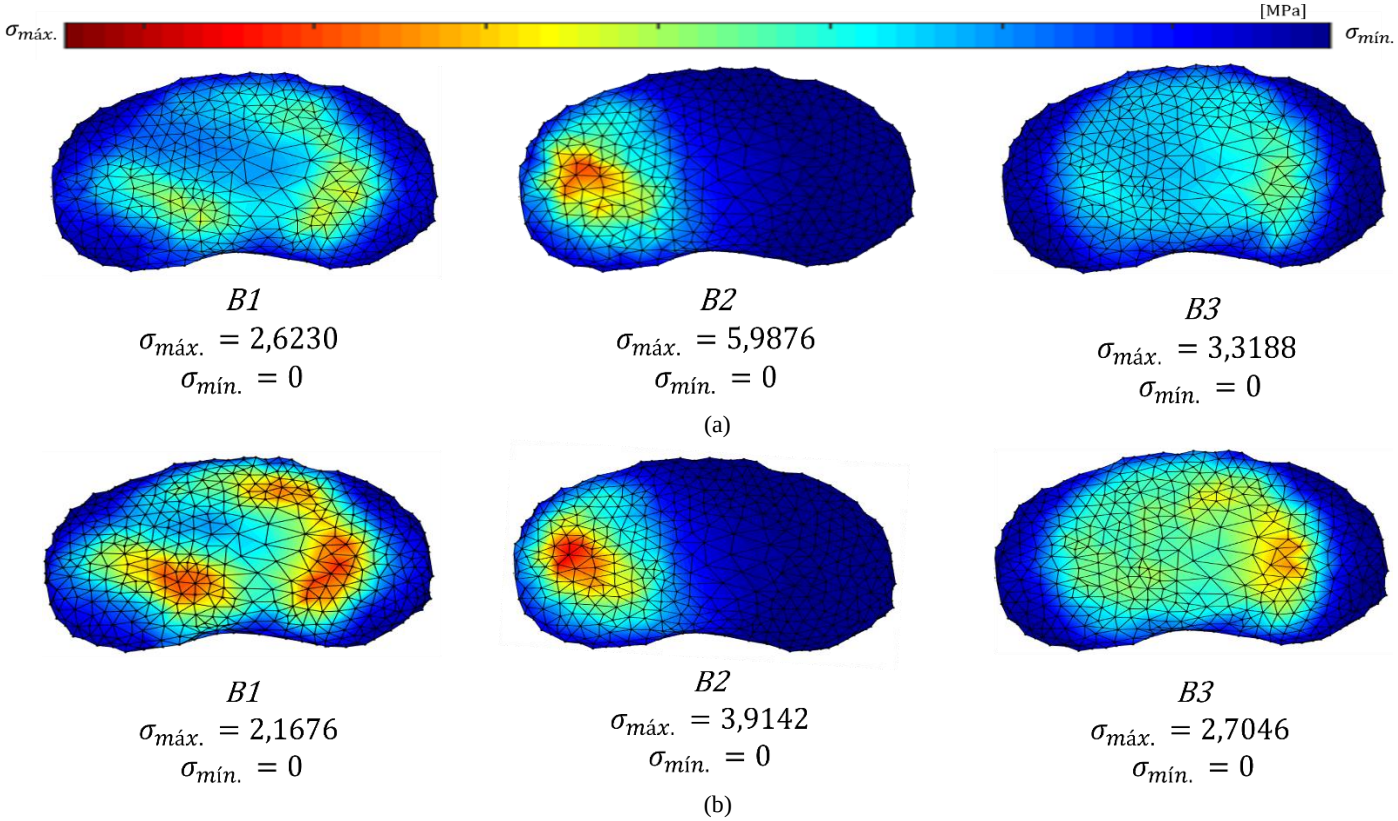

Fig.4 – Colored maps of the effective distribution of von Mises stresses (MPa) for a degenerated IVD (A) in 3 different load cases(1, 2 and 3) for (a) FEM analysis; (b) RPIM analysis.

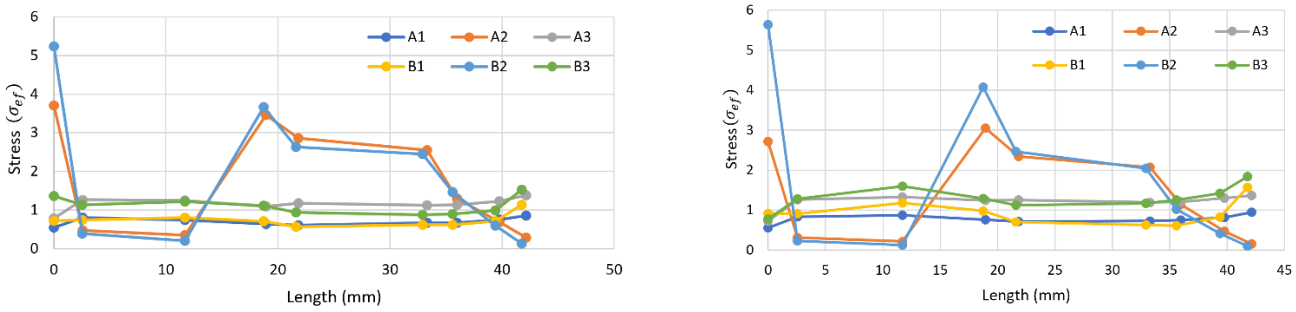

Fig.5 - Graphical representations of the von Mises's effective stress (MPa) for the length of the regionof interest using (a) FEM analysis; (b) RPIM analysis.

5. Conclusion

The main objectives of the present work were: to compare the performance of a meshless method (RPIM) and the FEM; and to study the application of different pressures in both healthy and degenerated IVDs. To achieve this goal, a 3D model of an IVD was constructed and analyzed using an elasto-static formulation. When analyzing the different stress fields obtained, it was possible to corroborate the literature, in the sense that a degenerated IVD (higher Young's

modulus) presents higher von Mises stresses than a healthy IVD (smaller Young's modulus). It was also possible to conclude that when comparing the values obtained by FEM with RPIM, they do not vary significantly. Besides that, for a region of interest, stress and strain will not present similar behavior, because mechanical properties are not the same.

With this study, it was possible to observe the advantages of using discretization techniques and simulation in the medical field, as well as the robustness and maturity of meshless methods in the biomechanical simulation of biological structures. However, it is important to refer that, involving meshless methods, no similar studies were found in literature, which hinders a more detailed comparison and validations of the RPIM performance.

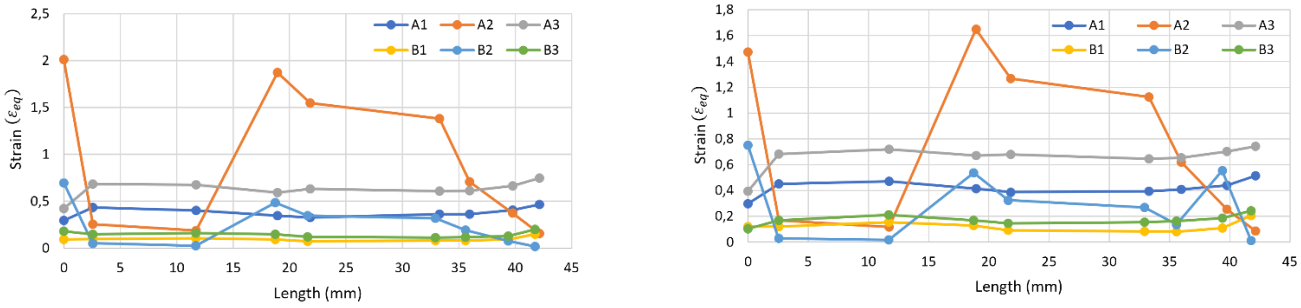

(a) (b)

Fig.6 - Graphical representations of the equivalent strain (MPa) for the length ofthe region of interest using (a) FEM analysis; (b) RPIM analysis.

References

[1] B. R. Whatley and X. Wen, "Intervertebral disc (IVD): Structure, degeneration, repair and regeneration," *Mater. Sci. Eng. C*, vol. 32, no. 2, pp. 61–77, 2012.

[2] M. Bashkuev, S. Reitmaier, and H. Schmidt, "Relationship between intervertebral disc and facet joint degeneration: A probabilistic finite element model study," *J. Biomech.*, vol. 102, p. 109518, 2020.

[3] C. S. C. F. França, "Modelo Matemático da Coluna Vertebral," 2010.

[4] D. G. de Oliveira, "Análise mecânica da coluna lombar com ênfase nos esforços nos ligamentos," p. 141, 2013.

[5] N. Newell, J. P. Little, A. Christou, M. A. Adams, C. J. Adam, and S. D. Masouros, "Biomechanics of the human intervertebral disc: A review of testing techniques and results," *J. Mech. Behav. Biomed. Mater.*, vol. 69, pp. 420–434, 2017.

[6] B. Yang and G. D. O'Connell, "Intervertebral disc swelling maintains strain homeostasis throughout the annulus fibrosus: A finite element analysis of healthy and degenerated discs," *Acta Biomater.*, vol. 100, pp. 61–74, 2019.

[7] C. O. S. Carneiro, "Caracterização do comportamento mecânico de uma vértebra lombar; com e sem cimentação," Faculdade de Engenharia da Universidade do Porto, 2014.

[8] Q. H. Zhang and E. C. Teo, "Finite element application in implant research for treatment of lumbar degenerative disc disease," *Med. Eng. Phys.*, vol. 30, no. 10, pp. 1246–1256, 2008.

[9] X. yi Cai *et al.*, "Biomechanical Effect of L4–L5 Intervertebral Disc Degeneration on the Lower Lumbar Spine: A Finite Element Study," *Orthop. Surg.*, vol. 12, no. 3, pp. 917–930, 2020.

[10] W. M. Park, K. Kim, and Y. H. Kim, "Effects of degenerated intervertebral discs on intersegmental rotations, intradiscal pressures, and facet joint forces of the whole lumbar spine," *Comput. Biol. Med.*, vol. 43, no. 9, pp. 1234–1240, 2013.

[11] F. F. Lemos, "Influência da desidratação no comportamento mecênico do disco intervertebral lombar," 2011.

[12] T. Guehring, F. Unglaub, H. Lorenz, G. Omlor, H. J. Wilke, and M. W. Kroeber, "Intradiscal pressure measurements in normal discs, compressed discs and compressed discs treated with axial posterior disc distraction: An experimental study on the rabbit lumbar spine model," *Eur. Spine J.*, vol. 15, no. 5, pp. 597–604, 2006.

[13] K. Sato, S. Kikuchi, and T. Yonezawa, "In vivo intradiscal pressure measurement in healthy individuals and in patients with ongoing back problems," *Spine (Phila. Pa. 1976).*, vol. 24, no. 23, pp. 2468–2474, 1999.

[14] H. Schmidt, A. Kettler, F. Heuer, U. Simon, L. Claes, and H. J. Wilke, "Intradiscal pressure, shear strain, and fiber strain in the intervertebral disc under combined loading," *Spine (Phila. Pa. 1976).*, vol. 32, no. 7, pp. 748–755, 2007.

[15] A. Nachemson, "Load on lumbar disks in various positions," *Clinical Orthopaedics and Related Research*, vol. 45. pp. 107–122, 1966.

[16] A. Rohlmann, T. Zander, H. Schmidt, H. J. Wilke, and G. Bergmann, "Analysis of the influence of disc degeneration on the mechanical behaviour of a lumbar motion segment using the finite element method," *J. Biomech.*, vol. 39, no. 13, pp. 2484–2490, 2006.

[17] R. El Kadmiri, Y. Belaasilia, A. Timesli, and M. S. Kadiri, "A coupled Meshless-FEM method based on strong form of Radial Point Interpolation Method (RPIM)," in *Journal of Physics: Conference Series*, 2021, vol. 1743, no. 1.
[18] G. R. Liu, G. Y. Zhang, Y. T. Gu, and Y. Y. Wang, "A meshfree radial point interpolation method (RPIM) for three-dimensional solids," *Comput. Mech.*, vol. 36, no. 6, pp. 421–430, 2005.
[19] A. C. S. Veiga, J. Belinha, and R. . N. Jorge, *BIOMECHANICAL SIMULATION OF HUMAN CHROMOSOMES*. 2019.
[20] L. Gonçalves Piqueiro and P. Jorge Américo Oliveira Pinto Belinha Professor Renato Manuel Natal Jorge, "A 2D Stress Analysis of Zirconia Dental Implants: A Comparison Study," 2016.
[21] J. D. Lee, Y. Chen, X. Zeng, A. Eskandarian, and M. Oskard, "Modeling and simulation of osteoporosis and fracture of trabecular bone by meshless method," *Int. J. Eng. Sci.*, vol. 45, no. 2–8, pp. 329–338, Feb. 2007.
[22] J. Belinha, *Meshless Methods in Biomechanics - Bone Tissue Remodelling Analysis*. 2014.
[23] S. Cristina and M. Plácido, "Avaliação Biomecânica das Vértebras Cervicais C6-C7 e Disco Intervertebral," 2015.
[24] M. N. Bureau, J. Legoux, J. Denault, and R. U. S. A. Data, "(12) Patent Application Publication (10) Pub. No.: US 2009/0177282 A1," vol. 1, no. 19, 2009.
[25] H. J. Wilke, P. Neef, M. Caimi, T. Hoogland, and L. E. Claes, "New In-vivo measurements of pressures in disc in daily," *Spine*, vol. 8. pp. 755–762, 1999.
[26] W. M. Park, Y. H. Kim, and S. Lee, "Effect of intervertebral disc degeneration on biomechanical behaviors of a lumbar motion segment under physiological loading conditions," *J. Mech. Sci. Technol.*, vol. 27, no. 2, pp. 483–489, 2013.